Universität Hamburg
DER FORSCHUNG | DER LEHRE | DER BILDUNG

FAKULTÄT
FÜR MATHEMATIK, INFORMATIK
UND NATURWISSENSCHAFTEN

Novel THz-streak Experiment for Time Resolved Measurement of Ultrafast Inner- and Interatomic Coulombic Decays

Dissertation
zur Erlangung des Doktorgrades
an der Fakultät für Mathematik, Informatik und Naturwissenschaften
Fachbereich Physik
der Universität Hamburg

vorgelegt von
Sophie Walther

Hamburg
2020

Gutachter/innen der Dissertation:	Prof. Dr. Ulrike Frühling PD Dr. Michael Martins
Zusammensetzung der Prüfungskommission:	Prof. Dr. Ulrike Frühling PD Dr. Michael Martins Prof Dr. Ludwig Mathey Prof Dr. Daria Gorelova PD Dr. Tim Laarman
Datum der Disputation:	14.10.2020
Vorsitzende/r des Prüfungskommission:	Prof Dr. Ludwig Mathey
Vorsitzende/r des Fach-Promotionsausschusses Physik:	Prof. Dr. Günter Hans Walter Sigl
Leiter des Fachbereichs Physik:	Prof. Dr. Wolfgang Hansen
Dekan der Fakultät für Mathematik, Informatik und Naturwissenschaften:	Prof. Dr. Heinrich Graener

Abstract

In the present work, time-resolved measurement techniques with resolutions in the femtosecond range were used to understand electronic excitations better and thus the formation and breaking of chemical bonds. Electrical excitations occur on a time scale in the attosecond to femtosecond range, and therefore ultra-short pulses in the extreme ultraviolet (XUV) range are needed to excite these processes. Furthermore, pulses in the terahertz range are used for the time resolution, as the pulse duration and slope of the electric field match the required temporal resolution. Within the scope of this work, a THz streak camera was set up to investigate decay times of an excited system in the femtosecond range. The functionality of the setup was investigated by measuring Xenon Auger electrons. The lifetime known from measurements of the spectral width of the Auger peaks was used as a reference. In the experiment, the XUV pulses used to ionize the atom or molecule are superimposed with THz pulses. The time offset between the XUV and THz pulses is varied and the change in kinetic energy of the photoelectrons and Auger electrons is measured. Since the Auger electrons are emitted at a different phase of the THz field, there is a time offset between the two curves. This time offset provides information about the lifetime of the process.

In addition, a setup was designed to measure the Interatomic Coulomb Decay (ICD) in neon dimers in the next step. ICD is a process that occurs in many weakly bound systems. In this process, the excitation energy is passed on to a neighboring atom or molecule, so it is strongly dependent on the internuclear distance between the two atoms or molecules. In contrast to the purely atomic Auger decays, the lifetime of these ICD processes can not be determined from spectral measurements of the line width. Therefore, it is of particular interest to investigate these ICD processes with time-resolved measurement methods, such as a THz streak camera. With the help of the measurements performed with the Auger electrons, the temporal resolution of the experimental setup was determined in order to be able to derive predictions about the feasibility of the ICD measurements. For ICD processes with a significantly longer lifetime than in typical Auger decays, the analysis shows that the experimental requirements are fulfilled. Thus, time-resolved measurements of ICD processes are possible.

Kurzfassung

In der vorliegenden Arbeit wurden zeitaufgelöste Messtechniken mit Auflösungen im Femtosekundenbereich eingesetzt um ein besseres Verständnis über elektronische Anregungen und damit über die Entstehung und das Aufbrechen chemischer Bindungen zu bekommen. Elektrische Anregungen laufen auf einer Zeitskala im Atto- bis Femtosekunden Bereich ab und daher werden für die Anregung dieser Prozesse ultrakurze Pulse im extrem ultravioletten (XUV) Bereich benötigt. Zudem werden für die zeitliche Auflösung Pulse im Terahertzbereich verwendet, da diese die benötigte Pulslänge besitzen um im Femtosekunden Bereich zu messen. Im Rahmen dieser Arbeit wurde eine THz-Streakkamera aufgebaut, mit der Zerfallszeiten eines angeregten Systems im Femtosekundenbereich untersucht werden können. Die Funktionalität des Aufbaus wurde durch Messung von Xenon-Auger-Elektronen untersucht. Dazu wurde die aus Messungen der spektralen Breite der Auger-Peaks bekannte Lebensdauer als Referenz verwendet. Im Experiment werden die zur Ionisierung des Atoms oder Moleküls verwendeten XUV-Pulse mit THz-Pulsen überlagert. Dabei wird der Zeitversatz zwischen den XUV- und THz-Pulsen variiert, und die Änderung der kinetischen Energie der Photo- und Auger-Elektronen gemessen. Da die Augerelektronen zu einer anderen Phase des THz-Feldes emittiert werden, kommt es zu einem zeitlichen Versatz zwischen den beiden Kurven. Dieser Zeitversatz gibt Auskunft über die Lebenszeit des Prozesses.

Zudem wurde ein Aufbau designt, mit dem im nächsten Schritt der Interatomare Coulombzerfall (ICD) in Neon-Dimeren gemessen werden soll. ICD ist ein Prozess, der in vielen schwach gebundenen Systemen auftritt und da bei diesem Prozess die Anregungsenergie an ein Nachbaratom oder Molekül weitergegeben wird, ist er stark vom internuklearen Abstand zwischen den beiden Atomen oder Molekülen abhängig. Im Gegensatz zu den rein atomaren Augerzerfällen kann die Lebensdauer dieser ICD-Prozesse also nicht aus spektralen Messungen der Linienbreite bestimmt werden. Daher ist es von besonderem Interesse, diese ICD-Prozesse mit zeitaufgelösten Messmethoden, wie z.B. einer THz-Streakkamera, zu untersuchen. Mit Hilfe der mit den Augerelektronen durchgeführten Messungen wurde die zeitliche Auflösung des experimentellen Aufbaus bestimmt, um daraus Voraussagen über die Machbarkeit der ICD Messungen ableiten zu können. Die Analyse zeigt, dass für ICD Prozesse mit einer deutlich größeren Lebensdauer als in normalen Augerzerfällen, die Anforderungen an das Experiment erfüllt sind und somit zeitaufgelöste Messungen von ICD Prozessen möglich sind.

Contents

1. Introduction

Understanding the temporal evolution of electronic excitations in atomic or molecular systems contributes greatly to a deeper understanding of chemical reactions, such as the formation or breaking of chemical bonds. With femtosecond time-resolved techniques, it is possible to observe these excitations directly. The timescale of electronic excitations is in the attosecond to femtosecond range and usually faster than the nuclear dynamics.

However, when light nuclei are involved, like hydrates [1], dissociation processes can be fast and evolve on the same timescale as electronic decay mechanisms. Also, decay processes involving two atoms or molecules like interatomic Coulombic decay (ICD) depend strongly on the internuclear distance of the involved atoms. If the lifetime of the decaying state is on the same time scale as nuclear motion, electronic decays can no longer be studied separately. With the development of the laser in 1960 [2], several new methods to investigate dynamics in atoms and molecules were opened up. Furthermore, the continued development of ultrashort pulse laser techniques like chirped-pulse amplification [3] and Kerr-lens mode-locking [4], made it possible to perform time-resolved spectroscopy on the natural time scale of atoms and molecules.

To observe electronic de-excitation mechanisms, ultrashort pulses with photon energies in the extreme ultraviolet (XUV) are needed to remove electrons from inner shells. The first results for the high-order harmonic generation (HHG) in 1987 [5] made it possible to explore new energy schemes in probing atoms and molecules. In HHG, an intense femtosecond laser is focused onto an atomic or molecular gas target, and XUV radiation at high multiples of the drive laser frequency can be produced. The XUV pulses generated by the driving laser are also in the femtosecond range. These short pulses give access to the natural time scale of atoms and molecules, which is in the several hundred attosecond to femtosecond range, and therefore access to the making and breaking of chemical bonds. To observe these processes in the time domain, measurements with femtosecond time resolution are required. One possibility is to use a light-field driven streak camera, where the time information imprinted in the temporal profile of the electron wavepacket is measured. The rapidly varying electric field of a light pulse changes the kinetic energy of the electrons from the ionization and decay process giving insight into the temporal evolution of the system. The slope of the changing electric field needs to be in the same time range as the process under study. For attosecond processes, a NIR laser can be used, since a laser at with 800 nm wavelength has an optical period of 2.7 fs and the slope of the electric field is in the attosecond range, so events in the attosecond range can be resolved [6]. The processes studied in this thesis, like inner shell relaxation by Auger decay

or ICD, are in the femtosecond range and therefore require longer wavelength electric fields in the THz range. The THz pulses required for this purpose can either be generated with an accelerator, e.g., using an undulator or a laser-based setup. In this thesis, nearly single-cycle THz pulses can be produced by optical rectification in a crystal using ultra-short laser pulses.

The streaking technique is used to investigate ultrafast processes within atoms or molecules, such as the measurement of lifetimes from non-radiative decays. By measuring known decays, for example, pure atomic Auger decays, the experimental setup can be tested, and the time resolution of the setup can be determined. In this thesis, the evaluation of the time shift between the delay-dependent streaking spectra of photo and Auger electrons in xenon is used to characterize the measurement setup. Furthermore, measurements with molecular Auger electrons in iodomethane were performed. From the measurements performed with xenon and iodomethane, the capabilities of the setup can be assessed.

The experimental setup was built as a test setup for a planned measurement of interatomic Coulomb Decay (ICD) in neon dimers. ICD occurs in excited systems of loosely bound matter, such as systems bound by van der Waals forces or hydrogen bonds. For systems in which the Auger decay is energetically not allowed, ICD may become the dominant decay process since ICD lifetimes are generally much faster than radiative decays. An interesting aspect of ICD is the non-exponential behavior of the decay. The decay rate depends strongly on the internuclear distance of the involved atoms. To measure the time-dependent behavior of ICD, a combination of coincidence measurements with THz streaking is proposed. The electrons and ion fragments from this decay will be measured in coincidence utilizing position- and time-dependent detectors, like they are used in a COLd Target Recoil-Ion Momentum Spectroscopy (COLTRIMS) detector. Such detectors are developed by the group of Prof. Jahnke in Frankfurt, which collaborated with our group on this project. Combining a COLTRIMS detector with THz-streaking is a new technique to perform time-resolved measurements of ICD processes.

In this thesis, the laser-based XUV source and THz source were set up, and measurements of Auger decay times were performed to characterize the setup and to determine the achievable temporal resolution. The differences between measurements of Auger decay times performed at FLASH [1] and with the laser-based methods used for the measurements are discussed. Furthermore, the design of the experiment combining COLTRIMS with THz-Streaking was developed. The thesis is structured in five parts. In the first part (Chapter 2), the theoretical concepts of high harmonic generation and THz radiation are explained. Furthermore, the principle of light-field and THz-streaking is introduced. In Chapter 3, the experimental setup of the XUV and THz source in the laboratory is described. In Chapter 4, the results of the characterization measurements of the light sources are shown, and the beam parameters in the interaction zone are characterized. In Chapter 5 the measurement results are presented and in Chapter 6 the results are summarized and put into context with future applications.

2. Theoretical Background

The natural time scale for the motion of atoms in molecules, e.g., the formation and breaking of the chemical bonds, is in the pico to femtosecond domain. In order to study theses reaction dynamics in the time domain, it is important to use radiation with pulse lengths in the order of the process under investigation. In this experiment, photons in the extreme ultraviolet (XUV) range are needed to remove electrons from inner shells. XUV radiation is electromagnetic radiation in the photon energy range from 10 eV to 124 eV (this corresponds to wavelengths of 124 nm to 10 nm). Electrons in inner shells are more tightly bound than typical valence electrons, where only energies of less than 25 eV are needed to extract the electron. For our streaking experiments, radiation in the terahertz (THz) range is needed. With these wavelengths, the desired time shifts in the femtosecond range can be measured. The wavelength range for this radiation is around 0.1 mm to 1 mm, so THz radiation lies in the range between infrared and microwave radiation. With ultrafast light sources in the extreme ultraviolet, the process of interest is initiated, which is then examined with a THz-driven streak camera. This camera covers the time domain in the order of several femtoseconds. So the streaking field needs a slope, with a time duration in the same order. Therefore it is necessary to use electromagnetic light fields, which are in the THz range.

In Section 2.1 of this chapter, the photoionization of atoms and molecules, as well as the Auger process and the interatomic Coulombic decay (ICD) following the excitation of an atom or molecule are described. In Section 2.2 and Section 2.3 the laser-based generation of radiation in the extreme ultraviolet (XUV) and the terahertz region is described. In the last part of this chapter, Section 2.4, the principle of the light-field-driven streak camera is explained.

2.1. Photoionization and Decay Processes

When a photon hits an electron in an atom or a molecule, it can be absorbed. A photon with an energy $E_\gamma = \hbar\omega$ which is absorbed by an atom can either excite a bound electron to a higher excited state or, if the energy is larger than the ionization potential I_p of the atom or molecule, the electron can escape to the continuum. The kinetic energy of the free electron is then given by:

$$E_{kin} = \hbar\omega - I_p \, .$$

The excess energy of the photon is converted into the kinetic energy of the electron. The ionization potential, which is the energy required to ionize an atom or molecule in the

gas phase, is in the range of a few eV to about 25 eV for helium. For inner shells the binding energy of the electrons is a lot higher, reaching up to a few keV for tightly bound electrons. Light in the visible range of the spectrum normally does not have enough energy to ionize an atom with a single photon. In this range, a multiphoton process is required to ionize atoms or molecules. In contrast, it is possible to use light in the extreme ultraviolet (XUV) or X-ray range to ionize atoms or molecules easily and even release electrons from inner valence orbitals.

2.1.1. Auger Decay

If an electron from an inner shell A is released, then the remaining ion is in an excited state. The de-excitation process releases energy, which can be released radiatively via the emission of a photon or non-radiatively via the so-called Auger process (discovered by Lise Meitner in 1922 [7] and Pierre Auger in 1923 [8]) where the excess energy is transmitted onto another electron from one of the outer shells of the atom. The kinetic energy of the Auger electron is given by the energy difference (B,C) between the two shells $\Delta E = E_A - E_B^*$ of the atom and the binding energy of the emitted electron:

$$E_{\text{ABC, kin. energy Auger}} = (E_A - E_B^*) - E_C^*,$$

where A, B, C are the three energy levels involved in the Auger process. The energies $E_{B,C}^*$ are the binding energies of the outer levels in the presence of an inner hole. They are larger than the respective binding energies in a neutral atom. The energy of Auger electrons only depends on the energies of the orbitals involved and is independent of the energy of the photon which produced the initial single ionized state. The process is shown in Figure 2.1, where A corresponds to the L-shell and the electrons B and C originate from the M-shell.

The measured Auger line has a certain spectral width - it has a Lorentz profile with a natural line width determined by the exponential decay of the inner shell hole $\Gamma = \hbar/\tau$. Here τ denotes the lifetime of the hole state and Γ is the line width. Typical values for τ lie between a few attoseconds and a few tens of femtoseconds. For pure atomic Auger decays the lifetime can be measured by measuring the spectral line width.

Following the X-ray level naming convention, the Auger electrons would be named, for example, KLL, LMM, etc. Later in this work, the NOO-Auger electrons of xenon will be examined. Where N is the inner shell, and the electrons which are filling this hole are emitted from the outer O-shells.

During the photoionization process, not all of the photon energy may be transmitted onto the photoelectron, but it can also be used to excite another electron into a higher state. This process is called shake-up. In the shake-up process, the emitted photoelectron has less energy due to the energy transfer into the shake-up electron. If the photon energy is used to remove another electron from an outer shell, the process is called a shake-off. Electrons from shake-up and shake-off processes are visible in the electron spectrum as

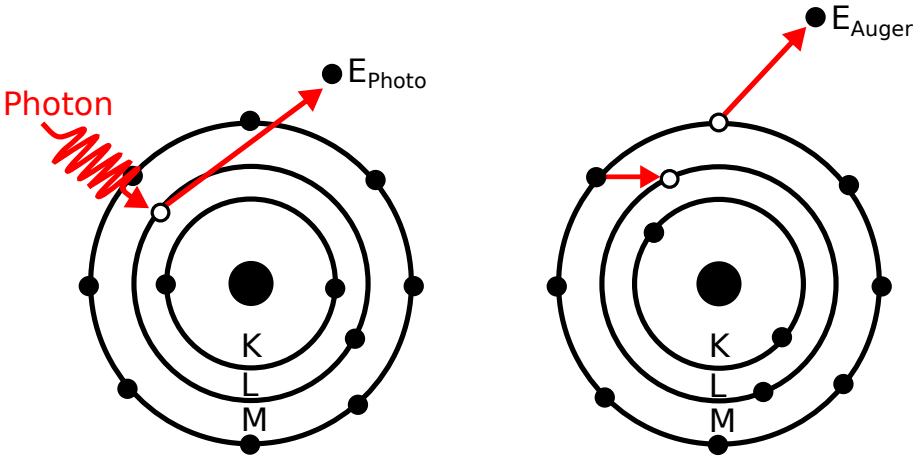

Figure 2.1.: On the left, the photoionization process is depicted, where a photon ionizes an atom. The electron is emitted from one of the inner shells of the atom (here L). In non-radiative decays, this can lead to the emission of an Auger electron (depicted on the right). An electron from the outer M-shell fills the vacancy in the L-shell, and another electron from the M-shell is emitted in the process. In this case the Auger emission is labeled as a LMM-Auger process. The inner shell *A* corresponds to the L-shell in this case and *B* and *C* are M-shells.

discrete lines with slightly lower energies than the normal photoelectron lines and are called satellites.

2.1.2. Interatomic Coulombic Decay

For some inner-valence ionized atoms or molecules, it is energetically prohibited to relax via Auger decay, since the ionization energy for an electron in an ionized atom is higher than the energy in a neutral atom. However, if the atom or molecule is surrounded by other atoms or molecules, the energy which is released via the relaxation of the ionized species can be transferred to a neighboring atom or molecule, where the binding energy of the outer electron is lower than the ionization energy of the ionized atom. This process is called interatomic Coulombic decay (ICD). It was first theoretically predicted in 1997 by Cederbaum et al. [9] and since then experimentally investigated in several studies, for example, first in 2003 by Marburger et al. [10] and in 2004 by Jahnke et al. [11]. In nature, ICD happens in weakly bound systems, like Van-der-Waals bound rare gases or hydrogen bound molecule clusters. For example, ICD has been observed in molecular water clusters and may be an important source of genotoxic low-energy electrons and radical cations.

ICD is an interatomic decay process, as depicted in Figure 2.2. It starts with the photoionization of one of the atoms in the dimer, where an inner-valence electron is removed, see Figure 2.2 a). In the case of the direct ICD process, the vacancy is filled by an outer electron from the same atom. It is also possible that the electron filling the vacancy originates from the neighbor atom. In this case the process would be called exchange ICD.

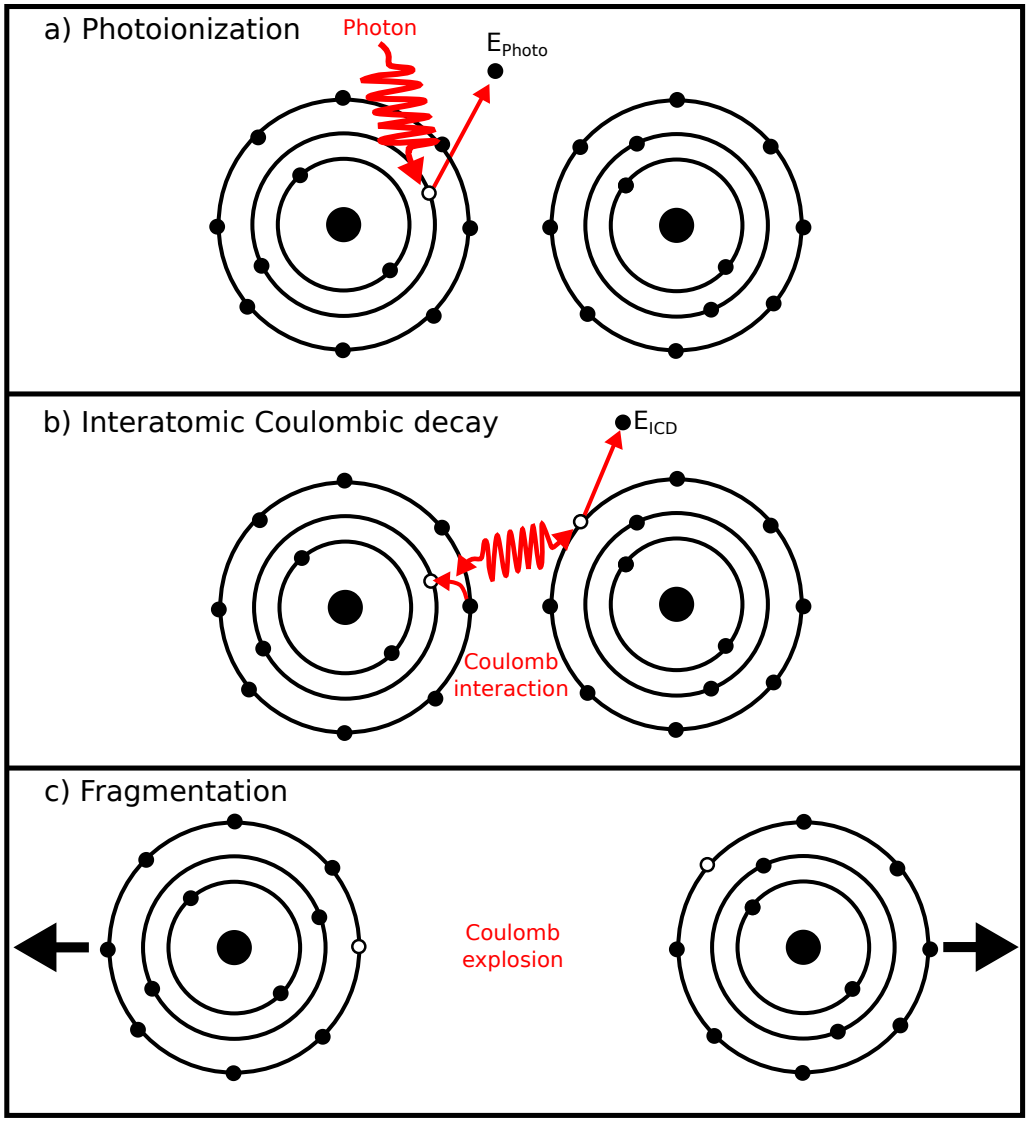

Figure 2.2.: Interatomic Coulombic decay in a dimer. a) An inner-valence electron is removed from one of the atoms in the dimer. b) An outer electron fills the valence, and the energy gained is transferred to the other atom of the dimer. c) Now there are two singly charged ions and the dimer fragments in a Coulomb explosion.

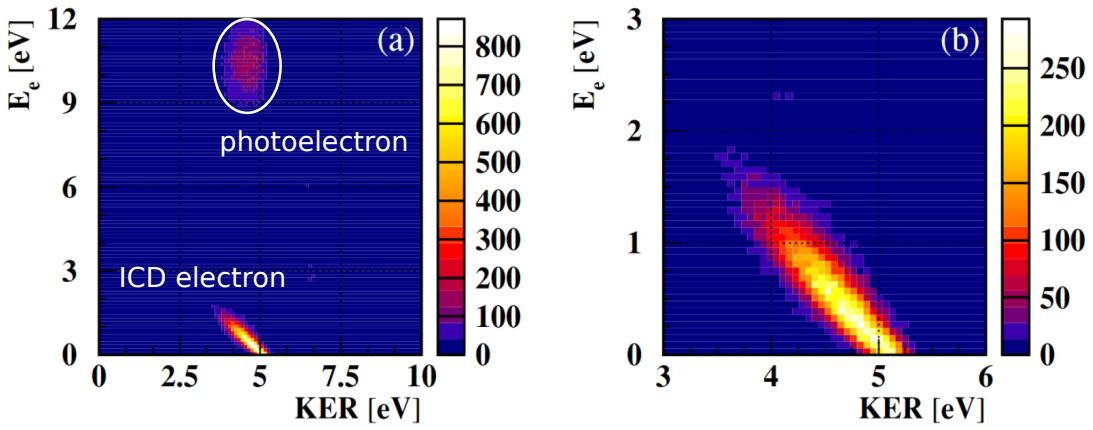

Figure 2.3.: a) The measured energy of the electrons in relation to the kinetic energy release (KER) of the ionic neon fragments. b) As the sum of the kinetic energy release and the ICD electron kinetic energy is a constant, events of ICD occur in this representation as a diagonal line (taken from [12]).

It was found that for the case of inner-valence ionization of a neon dimer, ICD occurs almost completely due to direct contribution, so in this thesis the focus is put on the direct ICD process. The de-excitation energy from filling the inner vacancy is transferred to the atomic neighbor, causing an ionization, see Figure 2.2 b). Afterward, both atoms are singly charged. Therefore the dimer fragments in a Coulomb explosion, Figure 2.2 c).

Figure 2.3 shows the measurement of the kinetic energy release (KER) of the ionic neon fragments in relation to the measured energy of one of the detected electrons. In neon the 1s, 2s, 2p shells are filled. In the experiment they observed the ionization of the 2s shell. The energy from the transition from 2p to 2s is not sufficient to remove an electron from the ionized neon atom. Therefore, the Auger decay in a single, isolated neon Atom is energetically prohibited.

ICD is energetically allowed since the amount of energy is sufficient to remove a 2p electron from a neighboring neutral neon atom. The neighboring neon atom in the dimer is then also ionized via the ICD process. As a result, the two ionized neon atoms are positively charged and fly apart due to Coulomb explosion. The energy of the photoelectrons, shown in Figure 2.3, is about 10 eV, as the measurements where performed with a photon energy 10 eV above the Ne-2s ionization threshold. For ICD processes, the sum of the KER and the ICD electron energy is a constant which results in a diagonal line when plotting the electron energy verses the KER.

Typically, ICD processes deviate from simple exponential decays. They have a strong dependence on the internuclear distance of the decay partners. The time-frame in which ICD occurs is often similar to that of the nuclear motion initiated by the excitation. This leads to a strong coupling of the electronic decay and the nuclear dynamics. It was predicted that the nuclear dynamics might be visible in a measurement [13]. If a neon dimer is excited to the intermediate $Ne^{+}(2s^{-1})$/Ne-state, this intermediate vibrational wave

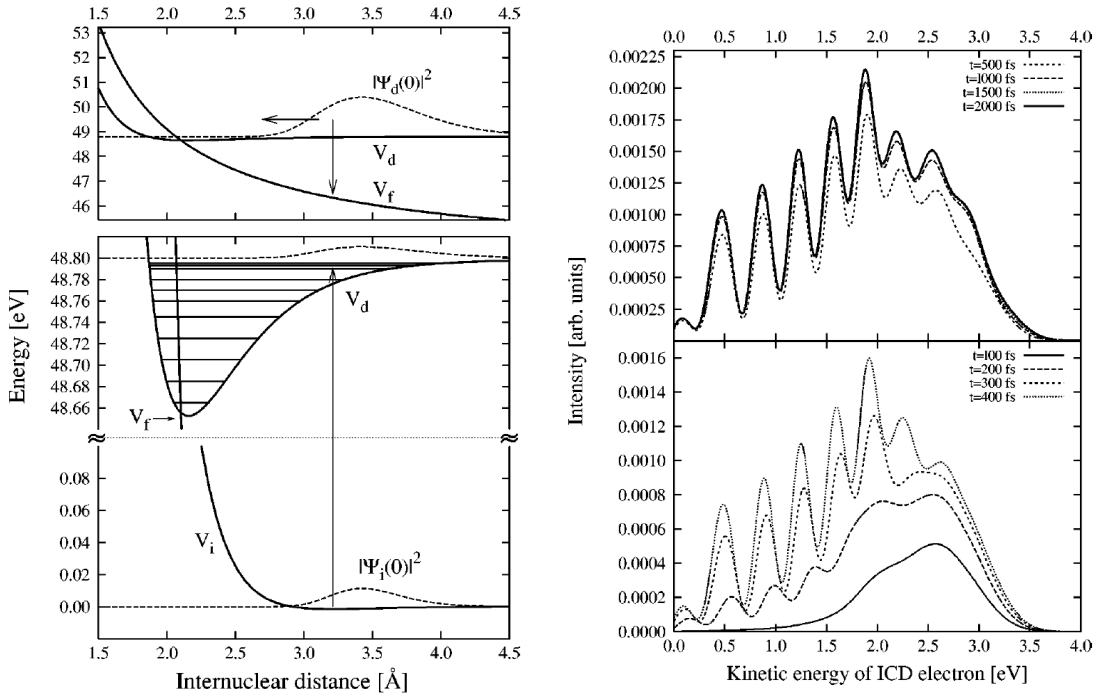

Figure 2.4.: Left: The nuclear dynamics in neon dimers. The initial wave packet $|\psi_i(0)|^2$ is centered around the equilibrium distance. It is exited to the intermediate state V_d. The intermediate wave package propagates on V_d and decays to the final state V_f, generating the final wave packet $|\psi_d(0)|^2$ (upper panel). Right: The time evolution of the ICD process can be seen from the oscillatory structure of the ICD spectrum (both taken from [13]).

packet starts to propagate on the intermediate potential energy surfaces (Figure 2.4, left). During this propagation, ICD occurs. From the calculations, it is expected that a nodal structure of the intermediate vibrational wave packet could be found in the ICD electron kinetic energy spectrum. This pattern is shown in the simulations performed in [13] (Figure 2.4, right). This shows that the temporal evolution of ICD is of great interest.

Some time-resolving techniques were already used to study ICD processes in some systems. One approach is to use a pump-probe setup. In pump-probe measurements, a short light pulse excites a system and a second time-delayed light pulse is used to probe it. One of the first measurements of ICD using the pump-probe technique was performed by Schnorr et al. [14] to determine the average decay width of ICD in neon dimers. There an average decay time of (150 ± 50) fs was found. Some difficulties of this method are that an exponential decay has to be assumed and that the measurement is very sensitive to the intensity of the ionizing setup in order to avoid multi-photon processes which could influence the results, as the measurement assumes doubly ionized states are coming only from ICD processes.

Another method for time-resolved ICD measurements is post collision interaction (PCI). In this method, a photoelectron emission is followed by the emission of a secondary electron with higher kinetic energy. When the secondary electron overtakes the slower

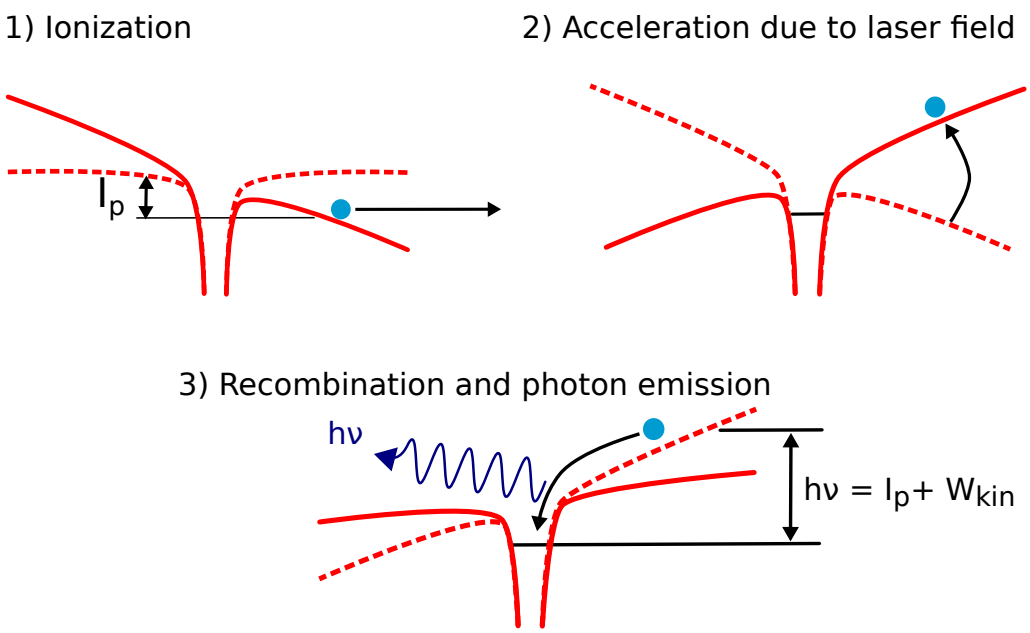

Figure 2.5.: HHG as described by the three-step model. (1) The strong laser field lowers the binding potential, and the electron can tunnel to the continuum; (2) the electron is accelerated by the laser field and (3) the electron can recollide with the parent ion, and the recombination leads to the emission of an XUV photon.

photoelectron, the photoelectron will be decelerated, as it is then exposed to the potential of the doubly charged ion and the secondary electron is accelerated. Therefore, the energy of the photoelectron depends on the time of the emission of the secondary electron. Measurements of the ICD time domain in helium dimers using the PCI method were performed by Trinter et al. [15]. This method is able to investigate non-exponential ICD processes, but is limited to certain systems, with fast photoelectrons and slow ICD electrons to observe PCI, and can not be used for all ICD processes. Therefore it is a good alternative to use THz-streaking for the time-resolved measurements, since this technique can be applied to all systems.

2.2. High Harmonic Generation

The interaction of strong laser fields (with intensities $> 10^{14}$ W/cm^2) with atoms can no longer be described only by the classical perturbative description of nonlinear optics. Instead, the response of the medium can be described semi-classically by the three-step model [16]) or quantum-mechanically by the strong field approximation (SFA) theory.

2.2.1. Three-step Model/ Single-atom Response

The mechanism of high harmonic generation (HHG) can be explained using the semi-classical so-called three-step model by Corkum [16]. In this model, a strong laser field

ionizes an atom, and the emitted (now free) electron is then accelerated by the laser field and finally recombines with the parent ion while emitting an extreme ultraviolet photon (Figure 2.5).

In the first step, the laser field lowers the binding potential of the atom and the potential energy is lower than the binding energy I_p. Then the electron can tunnel into the continuum. In this process, called tunnel ionization ([17], [18]), an electron from the atomic ground state can tunnel through the barrier formed by the Coulomb potential of the atom. In the second step the electron is accelerated by the linearly polarized laser field

$$E_L = E_0 \cos(\omega t),$$

and performs oscillatory motions. These motions can be described by classical mechanics:

$$\begin{aligned}
\ddot{z}(t) &= E_0 \cos(\omega t) \\
\dot{z}(t) &= \frac{E_0}{\omega} \left(\sin(\omega t) - \sin(\omega t_i)\right) \\
z(t) &= \frac{E_0}{\omega_0^2} \left((\cos \omega_0 t - \cos \omega_0 t_i) + ((\omega_0 t - \omega_0 t_i) \sin \omega_0 t_i)\right)
\end{aligned}$$

with initial conditions $z(t_i) = 0$ and $\dot{z}(t_i) = 0$, since the initial velocity of the electron born into the continuum is negligible and t_i is the time at which the electron was released from the atom. Here, only the motion in the z-direction has to be considered, as this is the direction of the laser polarization. By introducing the phase $\theta = \omega_0 t$ the equation can be rewritten as z(θ) and the kinetic energy in dependence of the phase can be obtained:

$$E_{kin}(\theta) = 2U_p(\sin\theta - \sin\theta_i)^2.$$

The quiver energy of the energy gain in the laser field is given by the ponderomotive energy U_p and is proportional to the intensity I of the driving laser. The ponderomotive energy is given by:

$$U_p = \frac{e^2 E_0^2}{m_e \omega_0^2} \approx I\lambda^2 \,,$$

where e, m_e are the charge and the mass of the electron, respectively and E_0 is the electric field strength. The ponderomotive energy is proportional to the square of the wavelength λ of the laser field.

Figure 2.6 shows the kinetic energy (in U_p) emitted upon recombination. The electrons can only recombine with the nucleus upon an emission during the phase $0 < \theta_i < \pi/2$. The trajectories for electrons are shown in Figure 2.6 (a) and the highest energy is obtained for an ionization phase $\theta_i \approx 17^\circ$ and the recombination phase at $\theta_r \approx 255^\circ$, as

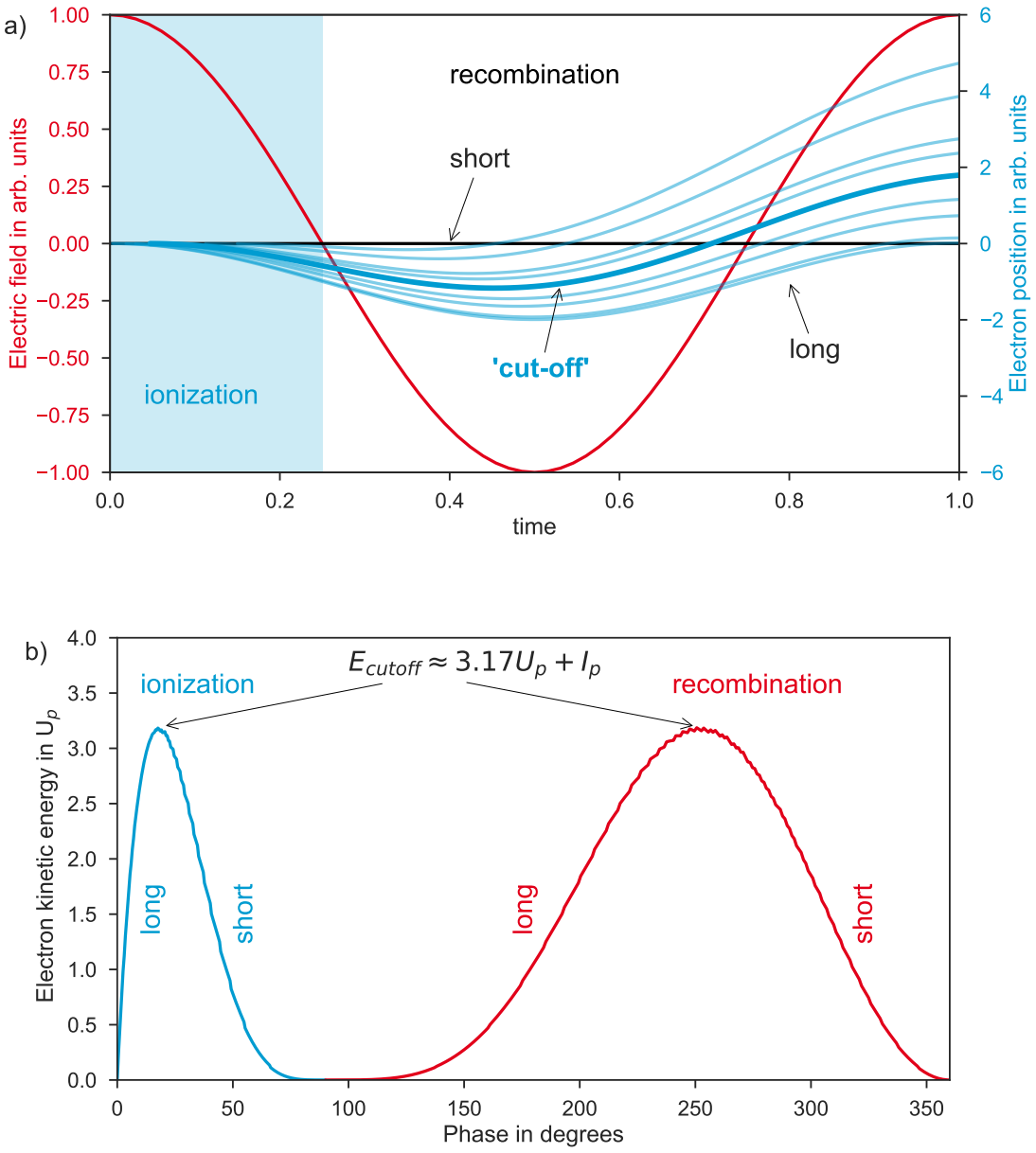

Figure 2.6.: In a) a classical calculation of the electric field and the electron trajectories are plotted. In (b) the kinetic energy, which is gained by the electron in the laser field depending on the phase of the field, is shown. For each kinetic energy, there are two possible trajectories (long and short) that join for the highest recollision energy E_{cutoff}.

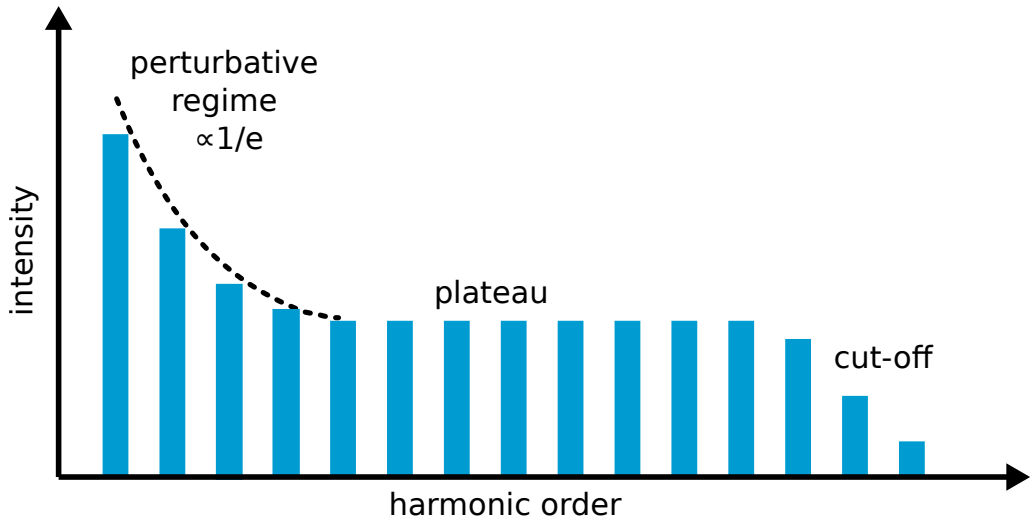

Figure 2.7.: A schematic high harmonic spectrum.

shown in Figure 2.6 (b). Here the maximum photon energy (cutoff energy) is given by:

$$E_{\text{cutoff}} = I_p + 3.17U_p \,,$$

where I_p is the ionization potential of the atom. For lower energies there are two possible trajectories (long for ionization times $\tau_l < \tau_c$, and short for ionization times $\tau_s > \tau_c$, with the ionization time τ_c for the cut-off energy). The ionization time for the cutoff energy is close to the maximum of the laser field, so the ionization probability is high. For clarity, only one cycle of ionization is shown, but the process of ionization and recombination repeats itself every half cycle. The emission of a short pulse of XUV photons occurs every half-laser cycle. The interference of the XUV pulses emitted with opposite signs every half-laser cycle leads to a spectrum of odd harmonics of the fundamental laser frequency. A schematic high harmonic spectrum is shown in Figure 2.7. For low harmonic orders, the intensity drops exponentially. For higher harmonic orders, the harmonics are in the "plateau region", where the intensity is approximately constant until the cut-off is reached.

2.2.2. Phase-matching

Harmonic generation is influenced by a number of effects that only occur when a gas volume is observed in a propagating laser field instead of just one atom. The process's efficiency depends strongly on the phase matching of the IR pulse with the XUV pulse. The XUV photons which are generated in the interaction zone should overlap coherently. So apart from the single-atom response, macroscopic effects like phase-matching and the generation geometry have also to be taken into account to generate high harmonics efficiently. The driving laser and the generated high order harmonics have to be phase-matched [19, 20]. There are three main contributions to the wave vector mismatch:

$$\Delta k_z(r,z,t) = \Delta k_{\text{dipole}} + \Delta k_{\text{gouy}} + \underbrace{\Delta k_{\text{at}} + \Delta k_{\text{elec}}}_{\text{dispersion}}, \tag{2.1}$$

where Δk_{gouy} is the geometrical wave vector mismatch, $\Delta k_{\text{dispersion}} = \Delta k_{\text{at}} + \Delta k_{\text{elec}}$ is the dispersion of the generating medium, with the contributions from the atoms and the free electrons and Δk_{dipole} is due to the intensity dependent dipole phase.

The last contribution is due the atomic phase and depends on the quantum path, so it is different for short and long trajectories, with $\Delta k_{\text{dipole}} = -\alpha \nabla I$, where α is $\alpha_{\text{short}} \approx 2 \times 10^{-14}$ cm^2/W and $\alpha_{\text{long}} \approx 22 \times 10^{-14}$ cm^2/W for short and long trajectories, respectively [20].

The dispersion term is

$$\Delta k_{\text{dispersion}} = \frac{2\pi q}{\lambda} \frac{p}{p_0} \Delta\delta \left(1 - \frac{\eta}{\eta_c}\right) ,$$

where q is the harmonic order, η_c is the critical ionization fraction, p_0 is the standard pressure (1030 mbar) and $\Delta\delta$ is the difference of the refractive indices of the fundamental and the high order harmonic. This term scales linearly with the pressure p. Values for η_c are in the order of a few percents in the near IR-region, e.g., 1% for Ne for a fundamental wavelength of 800 nm.

Phase matching can be achieved by adjusting the gas pressure until the dispersion of the generating medium compensates for the Gouy phase and the dipole phase. Another limiting factor for HHG is reabsorption of the generated high harmonic photons in the generation medium. For a phase-matched generating medium, the absorption limit is three times the absorption length $l_{\text{abs}} = 1/\sigma\rho$. Here σ is the absorption cross section and ρ is the target gas density.

2.3. THz Radiation

To generate THz radiation, a laser-based THz source was used. The experimental setup of the THz source was designed and build by Anastasios Dimitriou for the measurements performed by Martin Ranke [21] and then adjusted for the measurements in this thesis. In the following chapter, the generation and detection techniques of THz radiation will be introduced.

2.3.1. THz Generation Techniques: Optical Rectification

THz radiation has a wide variety of applications, and it can be used for probing and controlling material properties in systems such as superconductors [22] or for applications like nonlinear spectroscopy [23]. Currently, the most efficient approach to generate

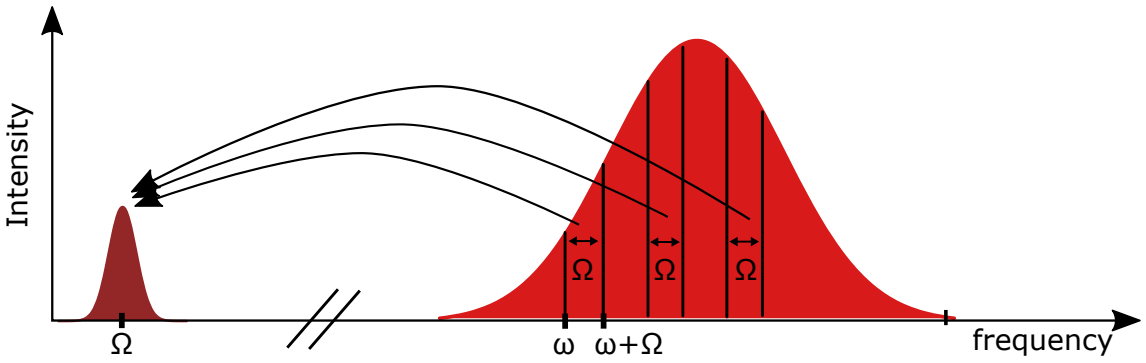

Figure 2.8.: Principle of OR. The spectral components ω and $\omega + \Omega$ generate THz radiation with a central frequency Ω, via intra-pulse difference generation.

THz radiation is by using optical rectification (OR) in nonlinear crystals. OR is a second order nonlinear process; it is based on intra-pulse difference generation between the different spectral components of the pulse, for example the two terms $E_{\mathrm{op}}(\omega + \Omega, x, z)$ and $E_{\mathrm{op}}(\omega, x, z)$ of the pulse can induce the electric polarization $P_{\mathrm{THz}}(\Omega, x, z)$, which drives the THz electric field at the angular frequency Ω, see Figure 2.8.

In general in nonlinear optics, the emission of electromagnetic waves in the THz spectral range can be expressed as a power series of the electrical field E. The optical rectification can be expressed by the polarization P due to the electric field:

$$P = \chi(E)E,$$

where $\chi(E)$ is the electric susceptibility and the nonlinear properties can be described by expanding $\chi(E)$ in powers of the field E:

$$\mathbf{P} = \epsilon_0(\chi^{(1)}\mathbf{E} + \chi^{(2)}\mathbf{EE} + \chi^{(3)}\mathbf{EEE}\dots),$$

with the free space permittivity ϵ_0, the nth-order susceptibility tensor of the material $\chi^{(n)}$. For the OR, which is a second order process we then get:

$$P_{\mathrm{THz}}(\Omega, x, z) = \epsilon_0 \chi^{(2)}_{\mathrm{eff}}(x, z) \int_0^\infty E_{\mathrm{op}}(\omega + \Omega, x, z) E^*_{\mathrm{op}}(\omega, x, z) \mathrm{d}\omega \,,$$

with the effective second order nonlinear susceptibility $\chi^{(2)}_{\mathrm{eff}}(x, z)$ at the spatial position (x, z).

Ideally, the generated THz pulse only depends on the intensity and the initial spectrum of the pump pulse, but in reality, the THz generation efficiency depends on several other factors. The medium has to have a non-centrosymmetric crystal structure and should have a high damage threshold to withstand the effects of the high intensities from the femtosecond pulses. Furthermore, material properties, like the absorption, diffraction, and phase matching conditions play a role. Here the matching of the optical group ve-

locity and the THz phase velocity is one of the most crucial factors for an efficient OR process. This condition also determines the optimal length and orientation of the crystal.

In the ideal case, for phase-matched generation the following conditions should be fulfilled:

$$v_{\mathrm{NIR}}^{gr} = v_{\mathrm{THz}}\,, \qquad n_{\mathrm{NIR}} = n_{\mathrm{THz}}.$$

And then the wave vector mismatch should ideally be zero:

$$\Delta\mathbf{k} = \mathbf{k}_{\mathrm{NIR+THz}} - \mathbf{k}_{\mathrm{NIR}} - \mathbf{k}_{\mathrm{THz}} = 0.$$

2.3.2. Materials for THz Generation

To select a material for THz generation, the effective nonlinear coefficient, the THz absorption, and the phase matching between the pump and the THz beam must be considered.

To compare the suitability of different materials for THz generation by OR, the efficiency of DFG should be taken into account. For phase-matched conditions it is given by [24]:

$$\eta_{\mathrm{THz}} = \frac{2\omega^2 d_{\mathrm{eff}}^2 L^2 I}{\epsilon_0 n_{\mathrm{NIR}}^2 n_{\mathrm{THz}} c^3} \exp\left(-\alpha_{\mathrm{THz}} L/2\right) \frac{\sinh(\alpha_{\mathrm{THz}}(L/4))}{[\alpha_{\mathrm{THz}} L/4]^2},$$

where ω is the angular difference (THz) frequency, d_{eff} is the effective nonlinear coefficient, I is the intensity of the IR laser, L is the medium length and α_{THz} the absorption coefficient for the THz radiation. The efficiency of difference frequency generation without absorption ($\alpha_{\mathrm{THz}} L \ll 1$) of the pump pulse is given by:

$$\eta_{\mathrm{THz}} = \frac{2\omega^2 d_{\mathrm{eff}}^2 L^2 I}{\epsilon_0 n_{\mathrm{NIR}}^2 n_{\mathrm{THz}} c^3}.$$

On the other hand for large absorption ($\alpha_{\mathrm{THz}} L \gg 1$) the efficiency is approximately given by:

$$\eta_{\mathrm{THz}} = \frac{8\omega^2 d_{\mathrm{eff}}^2 I}{\epsilon_0 n_{\mathrm{NIR}}^2 n_{\mathrm{THz}} c^3 \alpha_{\mathrm{THz}}^2}.$$

So for a crystal with a length larger than $L_{\mathrm{eff}} = \alpha_{\mathrm{THz}}^{-1}$, only the photons produced in the length L_{eff}, with respect to the exit surface, contribute to the signal. In Table 2.1 some properties of materials, which are suitable for OR pumped with 800 nm light are shown.

Note that the values for n_{THz} and α_{THz} are given for 1 THz. These values are highly dependent on the frequency and also on the temperature of the medium. For example the absorption coefficient of LN strongly decreases with decreasing temperature [26].

ZnTe has approximately a two times smaller nonlinear coefficient than LN. Nonetheless, ZnTe is widely used as an electro-optic crystal for OR and electro-optic sampling,

Table 2.1.: Material properties of crystals for THz generation (values taken from [25])

Material	d_{eff} [pm/V]	$n^{gr}_{800\text{nm}}$	n_{THz}	α_{THz} [cm^{-1}]	λ_0 = 800nm		E_g [eV]
					γ	Pump absorption	
ZnTe	68.5	3.13	3.17	1.3	collinear	2 PA	2.26
LN	168	2.25	4.96	17	62.7 °	3 PA	3.8

see Section 2.3.4. ZnTe can be used in a collinear velocity matching setup between the pump pulse and the THz radiation, which makes it an attractive material in some setups. For other materials, a non-collinear geometry has to be used to achieve quasi-phase-matching, as will be discussed in the following Section 2.3.3.

For Ti:sapphire lasers, with a wavelength of about 800 nm, LN is a commonly used material for the generation of THz radiation. It is a compound made of lithium, niobium and oxygen and can be doped with magnesium oxide, which helps to increase the threshold for optical damage (photorefractive damage). Stochiometric $LiNbO_3$ (sLN) has a higher nonlinear coefficient than most of the semiconductor materials like ZnTe.

Additionally, $LiNbO_3$ has a higher bandgap than other semiconductors, so photon absorption at 800 nm is only possible for three photon absorption. However, sLN crystals experience strong photorefraction if they are not doped with Mg to increase the threshold of optical damage [24].

Two main factors limiting the THz generation efficiency are the cascading effects and the free carrier absorption (FCA) of 800 nm pump radiation. Since ZnTe has a relatively small bandgap (2.26 eV), so two-photon absorption is possible ($E_{\gamma=800nm}$ = 1.56 eV). The direct bandgap (E_g) of lithium niobate is 3.8 eV at room temperature, so here FCA is only possible for three photons. The negative effect of FCA is not the loss of pump intensity but rather the strong THz absorption due to free carriers created by the FCA. So in order to further increase generation efficiency, it is beneficial to increase the wavelength and decrease the nonlinear absorption rate from three-photon absorption (3PA). The other factor, as mentioned above, are cascading effects. Typically, in nonlinear optics, the energy exchange between pump, signal and idler light waves is controlled by the Manley-Rowe relations. They require that an equal number of photons participates in the nonlinear interaction, e.g., for a three-wave mixing system with frequencies ω_I, ω_J, ω_K, where the condition $\omega_I + \omega_J + \omega_K = 0$ is fulfilled, an equal number of photons from each mode participate in the nonlinear interaction. However, the measured efficiency of THz generation can be higher than calculated from the Manley-Rowe relations. As the optical pulse propagates through the medium, it generates THz radiation at a frequency Ω, but simultaneously the pulse also suffers a frequency downshift. So while the pulse generates THz, it experiences a cascaded frequency downshift [27]. The broadening of the optical spectrum results in a disruption of the phase-matching conditions due to an enhancement of the group velocity dispersion, and after some time, the THz generation

shuts down. Therefore, cascading effects can increase the conversion efficiency above the Manley-Rowe limit [28], but can also stop the generation of THz at some point due to angular dispersion of the beam. For Ti:sapphire beams, the cascading effects along with the angular dispersion and the FCA are the limiting mechanisms for the conversion efficiency [29].

Another limitation is the damage threshold of the material. For high intensities, multi-photon ionization is possible, and a large number of free carriers (here the free electron density) is created. When the free electron density reaches the critical value, the plasma frequency is equal to the femtosecond laser frequency. At this point, the laser can be absorbed sharply, and the deposited energy is high. This can lead to macroscopic damages of the crystal [30]. The damage caused to the crystal comes mainly from free electrons getting heated by the laser and transferring their energy to the lattice. The critical free electron density for Lithium niobate with a femtosecond 800 nm laser is $n_{cr} = 1.74 \cdot 10^{21}$ cm^{-3} and the damage threshold for $LiNbO_3$ is approximately 0.35 $\mathrm{J/cm}^2$ [30].

2.3.3. Pulse Front Tilt - Phase-matching

To fulfill the phase-matching conditions, the group velocity index of the material for the IR pump beam and the refractive index THz pulse should be approximately the same. However, for $LiNbO_3$ the refractive index for THz is much larger than for an 800 nm pump pulse.

A method to achieve phase-matching conditions in the material is to use a tilted pulse front [31] of the pump beam. The generated THz propagates perpendicular to the wave-front, with a velocity v^p_{THz}. So the tilt angle γ between the propagation directions of the pump pulse and the THz pulse is the same as that of the pulse front relative to the phase front of the pump pulse. Now the phase-matching condition is:

$$v^{gr}_{NIR} \cos\gamma = v^p_{THz} \,,$$

Where v^{gr}_{NIR} is the group velocity index of the pump beam. A schematic of the setup is shown in Figure 2.9.

Normally a grating is used to tilt the optical pulse and afterward the spot is imaged at the crystal position using a lens or a telescope setup. In a setup with a single lens and a diffraction grating, the crystal should be cut at an angle γ, then the tilt-angle is connected with the imaging and grating parameters by the following condition:

$$\tan\gamma = -\frac{mN\lambda_{\mathrm{pump}}M}{n_{\mathrm{pump}}\cos\beta} \,,$$

with the diffraction order m, the groove density of the grating N, the demagnification M and the diffracted angle β of the incident beam on the grating. Tilting the pulse front also

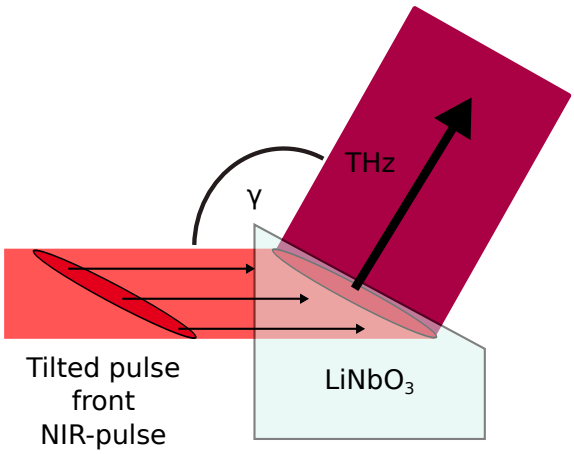

Figure 2.9.: A schematic of the TPF NIR-pulse and the generated THz pulse using a LN crystal.

leads to an angular spread whose angular dispersion $d\Theta/d\omega$ is given by:

$$\tan\gamma = -\frac{n_{NIR}}{n_{NIR}^{gr}}\frac{d\Theta}{d\omega},$$

with $n_{NIR}^{gr} = n_{NIR} + \omega(dn_{NIR}/d\omega) = c/v_{NIR}^{gr}$. For a light beam with a tilt of about $\gamma = 63°to65°$ the spread is about $\Delta\gamma \approx 2° - 5°$.

2.3.4. Electro-optical Coefficient and Pockels Effect

To determine the field intensity of the THz pulses, the pulse properties like size of focus, temporal profile and average pulse power need to be known. Often, these properties can not be measured easily. So a direct measurement of the THz field intensity is useful. This can be done through electro-optic (EO) sampling measurements. EO detection uses the second-order nonlinear EO effect. An applied electric field induces a refractive index change that is proportional to the applied field. This change in refractive index can be measured through a pump pulse passing through the crystal at the same time and measuring its change in polarization. The THz electric field intensity can be determined by varying the delay between the THz field and the pump pulse.

For EO sampling, electro-optic materials are needed. Optically active materials change their material properties when they are subjected to an electric field. In an anisotropic crystal the electric field causes a change in the refractive index. If the change in the refractive index is linear to the electric field, the effect is called Pockels effect and if it is proportional to the square of the applied field, it is called Kerr effect.

The changes in the refractive index are usually very small, but can still influence the propagation of light in the crystal. The effect can be used to measure the electric field of an external THz radiation pulse.

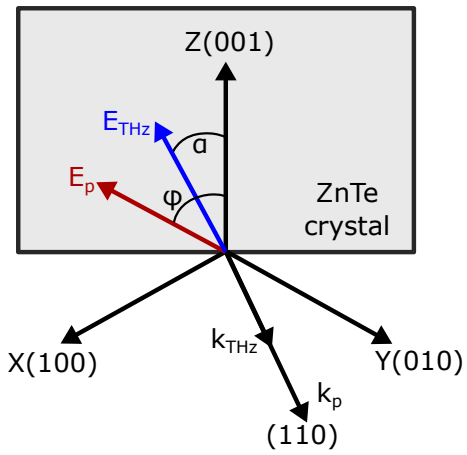

Figure 2.10.: Optical axes and wavevector for a (110)-oriented ZnTe crystal for the EO sampling scheme. α and φ are the angles of the THz and probe beam polarization direction with respect to the crystal (001) axis. The wave vectors k_{THz} and k_p give the propagation direction of the THz and probe pulse.

The electric field can be determined by measuring the intensity difference ΔI of the polarization components. The measured intensity difference depends on the angles of the THz pulse α and the probe pulse φ to the crystal axis, see Figure 2.10. The angles α and φ depend on the polarization of the pulses, so the crystal has to be adjusted at the right angle to achieve the most significant change in ΔI, to make it easier to measure the changes. The intensity change between both polarization components is given by

$$\Delta I(\alpha, \varphi) = I_p \frac{\omega n^3 E_{\mathrm{THz}} r_{41} L}{2c} (\cos\alpha \sin 2\varphi + 2 \sin\alpha \cos 2\varphi), \tag{2.2}$$

with L is the length of the crystal, r_{41} is the electro-optical coefficient (which is the only nonzero coefficient for a cubic crystal like ZnTe), c is the speed of light in vacuum, ω is the angular frequency of the probe pulse and I_p is the intensity of the probe pulse. The term in brackets becomes maximal for $\alpha = \varphi = 90°$. The final expression for the electric field is given by:

$$E_{\mathrm{THz}} = \frac{c}{\omega n^3 r_{41} L} \frac{\Delta I_{\max}}{I_p}$$

The the electro-optical coefficient of ZnTe (for a 110-orientation) is $r_{41} = 4.04$ pm/V [32] where $n = 2.854$ for a 800 nm pulse.

To measure the electric field and frequency of the THz beam and to make sure that we have a temporal overlap in the interaction zone between the THz and the XUV pulses, electro-optical sampling measurements were performed. The electric field of the THz pulse can be determined by measuring the ellipticity change of a co-propagating IR probe pulse after the crystal. The setup used here, called the collinear detection scheme, is

shown in Figure 2.11. The THz pulse and the probe pulse co-propagate through a ZnTe crystal. As shown in Table 2.1, the refractive index is similar for the 1 THz and the 800 nm pulses, so the collinear detection scheme has a good phase matching for both pulses. The refractive index change due to the THz electric field affects the ellipticity of the probe pulse, so by splitting up the beam in the s- and p-polarization components and using a balanced photodetector to measure the signal for the two orthogonal components of the probe pulse, the change caused by the electric field can be measured. Reading out the difference signal with an oscilloscope and using the delay stage to sample the electric field of the THz pulse, the pulse properties like field strength and duration of the THz pulse can be measured.

As seen from Equation (2.2), the induced change in polarization depends on the crystal orientation (given by the azimuthal angle α). In our setup the probe and the THz pulse polarization are perpendicular with $\varphi = \alpha + 90°$. To accurately measure the amplitude of the electric field, the crystal must be set at the correct angle. In Figure 2.12 the theoretical and the experimental dependence of the measured electric field depending on the crystal's azimuthal angle α is shown.

2.4. Light-field Streaking

In order to do time-resolved spectroscopy and measure processes in the natural time scale of atoms and molecules, it is necessary to be able to measure with an atto- or femtosecond resolution. To measure the duration of short pulses in the XUV range and also for measurements of the dynamics of electron processes in the femtosecond or attosecond range, a technique called light-field streaking is used [33]. It was first used for the measurement of attosecond XUV light pulses and is based on the principle of a conventional streak camera.

In a conventional streak camera, a light pulse hits a photocathode, and the resulting photoelectron wave packet is a direct replica of the temporal profile of the light intensity distribution. By applying a time-varying electric field, the electrons are transversely deflected, and the light's temporal structure is mapped onto the spatial distribution of the electrons, which can be measured by an electron-sensitive screen. However, the resolution of this streak camera is limited by the initial spread of the electron momenta and also by the space-charge effects between the electrons. Some of these limitations can be overcome by using an advanced technique of the streak camera, where the varying electric field is another light pulse (IR-field) that is collinearly overlapped with the ionizing XUV pulse in a rare gas target. In this setup, the gas target acts as a photocathode, and the photoionization of the atoms with the XUV pulse, happens during the streaking with the IR pulse, see Figure 2.13.

The energy change for the electrons depends on the phase of the IR-field during the photoionization. In this setup, the temporal profile is mapped onto the photoelectron energies. In order to use this light-field streaking technique, the XUV pulse length τ_{XUV}

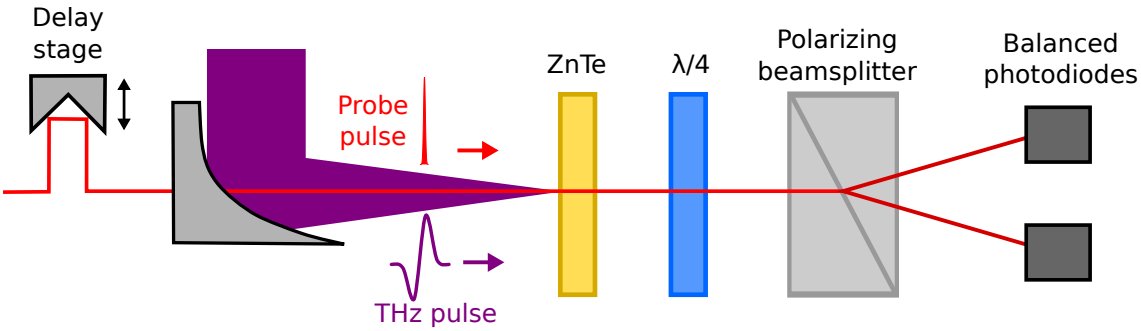

Figure 2.11.: Experimental setup for the electro-optical detection of the electric field of a THz pulse. The THz pulse and the IR probe pulse are overlapped and propagate collinearly through the electro-optic crystal (ZnTe). The change of the polarization of the IR probe pulse is measured by using a balanced detection scheme. A beam splitter splits the IR beam into the s- and p- components of polarization. The two orthogonal polarization components of the probe beam are then measured with two photodiodes, while the delay between the two pulses is changed using a delay stage.

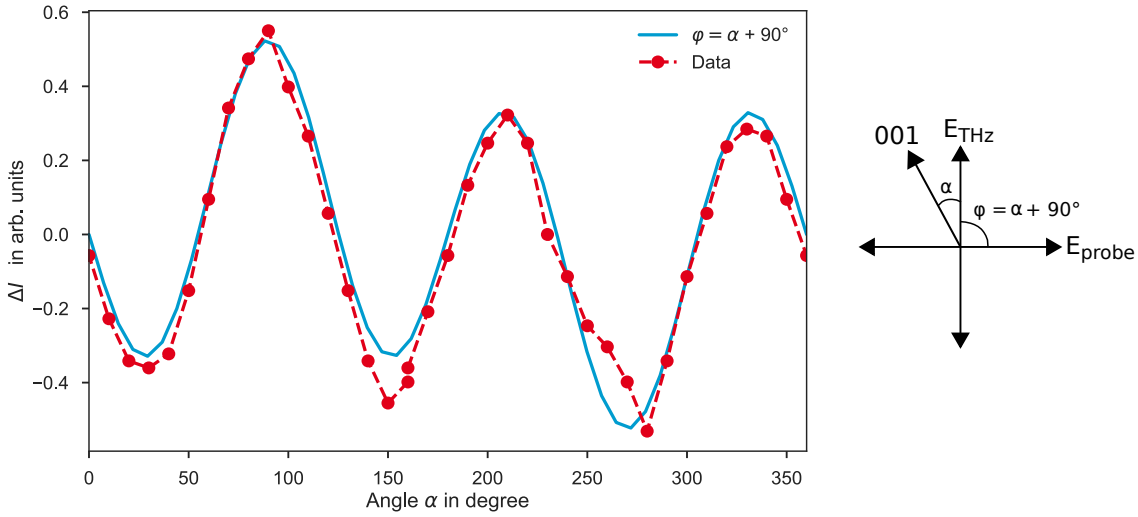

Figure 2.12.: Measured intensity change between the two polarization components of the probe beam in dependence of the crystal's azimuthal angle α. The EOS measurements should be performed for the maximal difference ΔI at angle 90° (or 290° measured by the crystal holder, which was not aligned with the crystal axis during assembling). The polarization of the THz beam and the probe beam are at a right angle, so $\varphi = \alpha + 90°$.

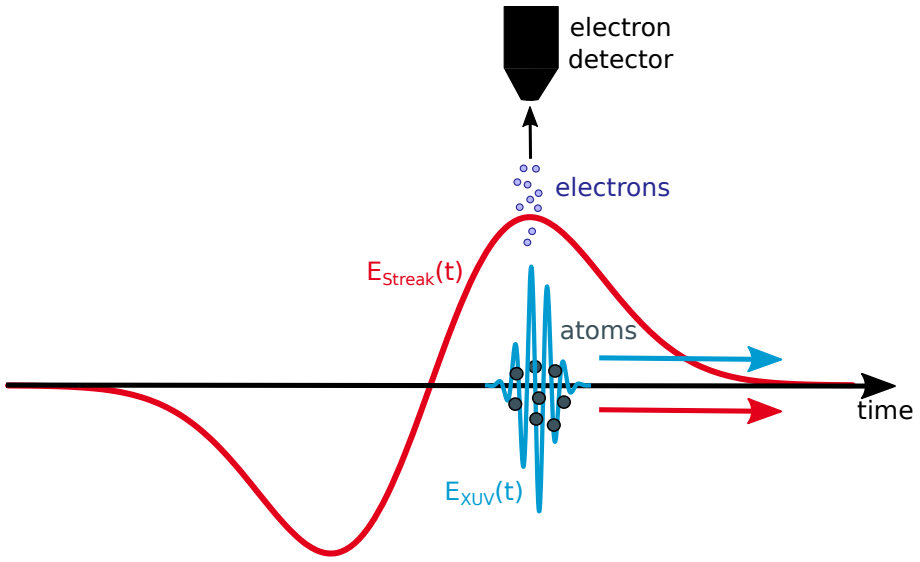

Figure 2.13.: Principle of a light-field streak camera. The electrons are generated by a XUV-pulse (E_{XUV}) while the electric field E_{Streak} changes the momentum of the electrons. The momentum change depends on the phase of the electric field E_{Streak} at the time of ionization.

should be short compared to the oscillation period T_{streak} of the streaking field $\tau_{\mathrm{XUV}} < T_{\mathrm{streak}}/4$. For attosecond XUV-pulse measurements, where this technique was first used, streaking fields in the visible to the infrared fulfill this condition. Longer XUV pulses and electron dynamics in the few tens to hundreds of femtoseconds can no longer be measured with these fields and a transition to longer wavelengths must be made. Here wavelengths in the far-infrared (with frequencies in the THz range) are used.

At first, a classical description of the process will be given to understand the process better, and then a quantum-mechanical description is given.

2.4.1. Classical Picture

For an electron which is ionized at time t_i in a linearly polarized electric field

$$E_{\mathrm{streak}}(t) = E_0(t)\cos(\omega_{\mathrm{streak}}t + \varphi)\,,$$

the momentum change due to the field is given by [34]:

$$\Delta p(t_i) = e\int_{t_i}^{\infty} E_{\mathrm{streak}}(t')\mathrm{d}t' = eA_{\mathrm{streak}}(t_i),$$

where $A_{\mathrm{streak}}(t)$ is the vector potential of the streaking field and e is the charge of the electron.

The final momentum $\boldsymbol{p}$ is given by $\boldsymbol{p} = \boldsymbol{p}_0 + \Delta\boldsymbol{p}$, where $\boldsymbol{p}_0$ is the initial momentum. The momentum change depends on the angle θ between the initial momentum and the

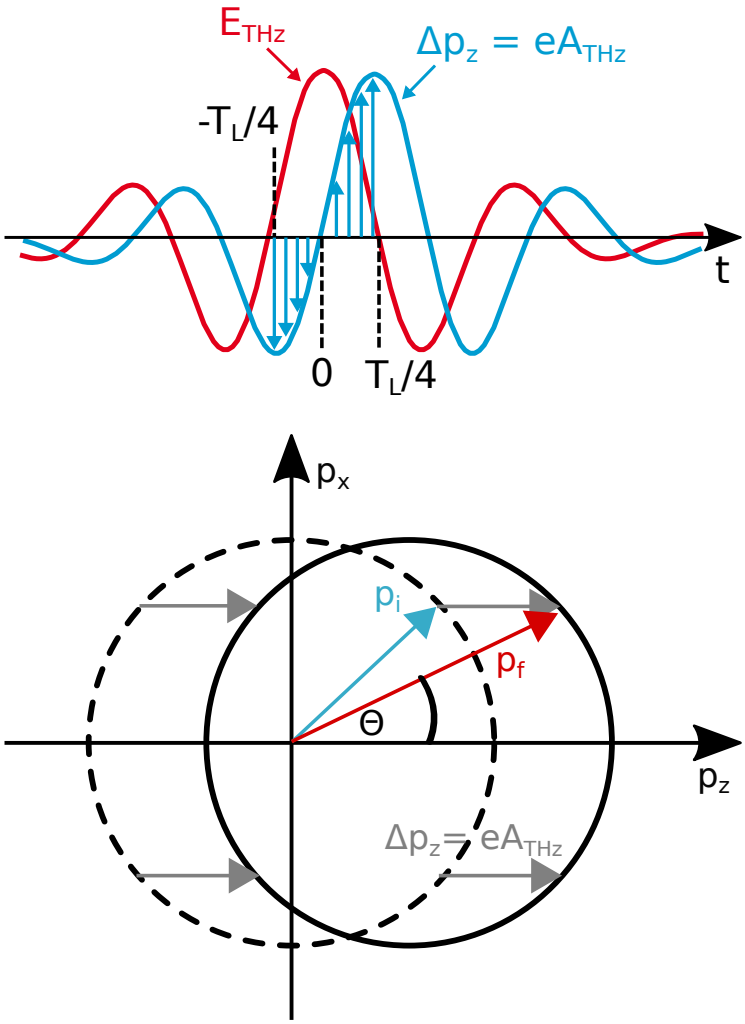

Figure 2.14.: Principle of photoelectron streaking. Top: Electrons are released into the electric field E_{THz}. Their momentum changes by Δp_z due to the vector potential A_{THz}. Bottom: Distribution of the electron momenta. The dashed circle are the initial momenta p_i, they are shifted if a laser streaking field with a vector potential $eA_{THz}(t)$ is present. The solid circle represents the final momenta p_f.

streaking field (see Figure 2.14). The final kinetic energy of the electrons after the light pulse is then:

$$\begin{aligned} W_{\text{kin}} &= \frac{|\boldsymbol{p}|^2}{2m_e} \\ &= W_0 + 2U_p \cos(2\theta) \sin^2(\varphi_i) \\ &\pm \sqrt{1 - \frac{2U_p}{W_0} \sin^2\theta \sin^2(\varphi_i)} \sqrt{8W_0 U_p} \cos\theta \sin(\varphi_i), \end{aligned} \tag{2.3}$$

where W_0 is the initial kinetic energy of the electrons, φ_i is the phase of the field at ionization time, m_e is the electron mass and $U_p = e^2 E_0^2 / 4 m_e \omega_{\text{streak}}^2$ is the ponderomotive energy.

Therefore the change in energy depends on the direction of the electron. The kinetic energies for detection geometries perpendicular ($\theta = 90°$) and parallel ($\theta = 0°$) to the laser polarization are given by:

$$\begin{aligned} W_{\text{kin},\parallel} &= W_0 + 2U_p \sin^2(\varphi_i) \pm \sqrt{8W_0 U_p} \sin(\varphi_i) \\ W_{\text{kin},\perp} &= W_0 - 2U_p \sin^2(\varphi_2). \end{aligned} \tag{2.4}$$

For perpendicular measurements, the electron spectra would be asymmetrically broadened and shifted to lower kinetic energies. In contrast, for electrons which are predominantly emitted in the direction of the laser polarization, the electron spectra will be up- or downshifted, depending on the direction of the electric field. Also, the second terms can be neglected if $U_p \ll W_0$, for the electron kinetic energies of interest. Therefore, neglecting the perpendicular energy shift, the energy change for parallel electrons is

$$\Delta W_{\text{kin}} = W_{\text{kin},\parallel} - W_0 \approx \sqrt{8U_p W_0} \sin(\varphi_i).$$

For small φ_i the ionization time is projected onto the kinetic energy of the electrons. Therefore measurements of the electron kinetic energy around the zero-crossing of the vector potential give a measurement of the time-dependence of the ionization process. However, this is only true if all photoelectrons have the same initial energy, which is not true if the XUV pulses have a non-vanishing spectral width and if the pulses have a chirp.

2.4.2. Quantum-mechanical Picture

In the previous section, electrons were treated as classical particles, but the full effects of the XUV pulse on the photoelectron spectrum can only be explained if the electrons are treated as a wave packet.

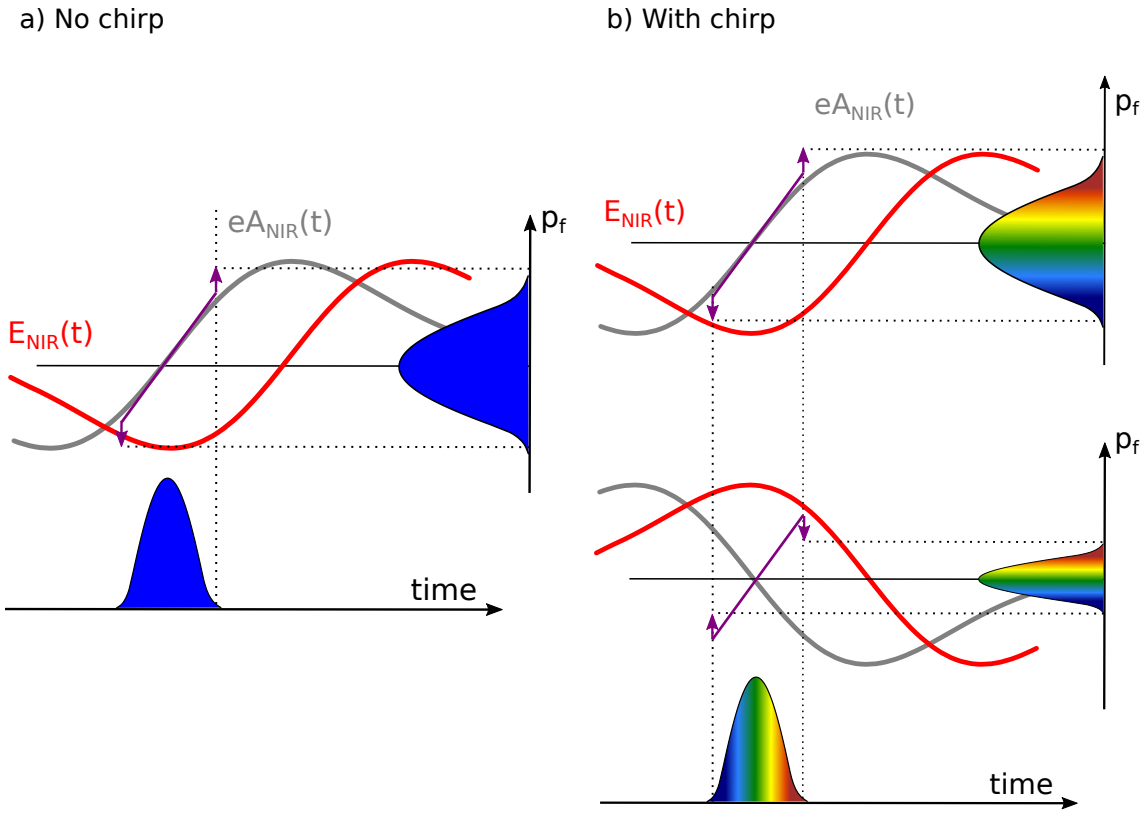

Figure 2.15.: Light-field driven streak camera for a non-chirped (a) and a linearly chirped pulse (b). The chirp is shown as color gradient of initial spectrum. (a) Around the zero crossing of the vector potential eA_{NIR} the spectrum gets broadened. (b) Top: For a the rising edge of the vector potential the spectrum is broadened, since higher energetic electrons which come first are accelerated more and electrons with lower energy are slowed down. Bottom: For a falling edge, the opposite effect appears. Electrons with high energy are slowed down and the spectrum becomes narrower.

To get a more general understanding of the process, the electrons are treated as a quantum-mechanical wave packet $|\psi(t)\rangle$ and the time-dependent Schrödinger equation (TDSE) in atomic units is

$$i\frac{\mathrm{d}}{\mathrm{d}t}|\psi(t)\rangle = \hat{H}(t)\,|\psi(t)\rangle\,.$$

In the dipole approximation, the Hamiltonian $\hat{H}$ can be written as:

$$\hat{H}(t) = \frac{1}{2}\left(\hat{p} + A(t)_{\mathrm{IR}}\right)^2 + V_{\mathrm{eff}}(r) + E_{\mathrm{XUV}}(t)\hat{r},$$

where the effective potential V_{eff} is due to the ion and the remaining bound electrons and $A(t)_{\mathrm{IR}}$ is the vector potential in the Coulomb gauge with $E(t)_{\mathrm{IR}} = -\partial A(t)_{\mathrm{IR}}/\partial t$. This is the so called single active electron approximation. Solving the fully numerical simulations of TDSE is not easily accomplished. Therefore, it is useful to make a few suitable approximations:

1. **Ionization process without NIR laser ($A_{\mathbf{IR}}(t) = 0$):** without the laser field the electron wave packet is a replica of the XUV pulse. The XUV pulse can be calculated from the photoelectron spectrum when the transition dipole matrix element $\mathbf{d_p}$ is known. The transition amplitude a_p for the population of the final continuum state $|p\rangle$ is given by Quéré et al. [35]:

   $$a_p = \langle p|\psi(t)\rangle = -i\int_{-\infty}^{\infty}\mathrm{d}t\;\mathbf{d_p}\mathbf{E}_{\mathrm{XUV}}\exp\left(i\left(\frac{p^2}{2} + I_p\right)\right),$$

   where $\mathbf{E}_{XUV}$ is the electric field of the ionizing field, $\mathbf{d_p}$ is the dipole matrix element from the ground state to the continuum state $|p\rangle$.

2. **NIR-streaking field present during photoemission:** considering the case in which a streaking laser field is present, then the transition amplitude in the strong field approximation (SFA) is given by:

   $$a_p = -i\int_{-\infty}^{\infty}\mathrm{d}t\mathbf{d}_{\mathbf{p}(\mathbf{t})}\mathbf{E}_{\mathrm{XUV}}(t-\tau)\exp\left(i\left(I_p t - \int_t^{\infty}\mathrm{d}t'\frac{p^2(t')}{2}\right)\right),$$

   where the momentum of the free electrons in the laser field is given by $p = (p_0 + A(t_i)) - A(t)$, and τ is the time delay between the XUV and NIR-pulse. In the SFA it is assumed that the effect of the ionic potential on the electron motion after ionization can be neglected. Rearranging the terms in the integral, the equation can be rewritten as

   $$a_p = -i\int_{-\infty}^{\infty}\mathrm{d}t\exp\left(i\phi_V(t)\right)\mathbf{d}_{\mathbf{p}(\mathbf{t})}\mathbf{E}_{\mathrm{XUV}}\exp\left(i\left(\frac{p^2}{2} + I_p\right)\right), \tag{2.5}$$

with the Volkov phase

$$\phi_V(t) = -\int_{-t}^{\infty} \mathrm{d}t'(pA(t') + A^2(t')/2).$$

The photoelectron spectrum $I(p,\tau)$ for a delay τ between the XUV and IR pulse, is given by the square of the transition amplitude

$$I(p,\tau) = |a_p(\tau)|^2 \,. \tag{2.6}$$

These equations can be used to retrieve the pulse properties from the measured spectrograms.

As can be seen from Equation (2.5), the modulated spectrum of the photoelectrons depends on the time τ at which the electron wave packet emerges into the continuum.

This dependence can be used to measure the relative arrival time between photoelectrons from different energy levels or between photoelectrons and electrons from longer-lived intermediate states, like Auger electrons. The arrival time difference is translated into an offset along the delay axis of the streaking curves. An electron that is released later into the streaking laser field experiences a different phase of the field.

In Figure 2.15 a), a streaked spectrum for a non-chirped XUV pulse is shown. The electron distribution is a replica of the XUV pulse and has a duration in the femtosecond range. The electron momenta are decreased or increased by the superimposed streaking field depending on its phase at the time of ionization. On the rising slope of the vector potential, the measured electron spectrum is broadened compared to the initial spectrum. The broadening of the measured spectrum depends on the XUV pulse length; for longer XUV pulses the broadening becomes more pronounced.

Using this principle gives access to the time dynamics of the photoexcitation process. The resolution of these measurements is determined by being able to extract the shift between the streaking curves and is influenced by the strength of the streaking field and the statistics of the streaked photoelectron spectra.

2.4.3. Reconstruction of the Linearly Chirped Gaussian Pulses

The time dependence of the phase modulation $\phi(t)$ of the electron wave packet makes it difficult to reconstruct the timing structure of the XUV pulse. Only for some special cases, where a few suitable approximations can be made, it is possible. We assume that the XUV pulse has only a linear chirp and a Gaussian envelope. For a linearly polarized laser field $E_{streak} = E_0 \cos(\omega_{streak} t)$ and if also $U_p << W$, as for most streaking experiments, then the phase modulation which can be written as a sum of three different terms:

$$\begin{aligned}
\phi(t) &= \phi_1(t) + \phi_2(t) + \phi_3(t) \\
\phi_1(t) &= -\int_t^\infty \mathrm{d}t\, U_p(t) \\
\phi_2(t) &= \frac{\sqrt{8WU_p(t)}}{\omega_{\text{streak}}} \cos\theta \cos(\omega_{\text{streak}} t) \\
\phi_3(t) &= -\frac{U_p(t)}{2\omega_{\text{streak}}} \sin(2\omega_{\text{streak}} t),
\end{aligned} \tag{2.7}$$

ϕ_2 is the dominant term and by setting $\theta = 0$ for electrons with a momentum parallel to the polarization of the laser field and inserting $\phi(t) = \phi_2(t)$ into Equation (2.6) the spectrum becomes:

$$I(p,t) \propto \exp\left(\frac{-a(\omega-\omega_0)^2}{2(a^2+(c\pm s/2)^2)}\right),$$

where c is the linear chirp of the Gaussian XUV pulse, $a = 1/4\tau_{\text{XUV}}^2$ and s is the streaking speed given by

$$s = \frac{\partial \delta W}{\partial t} = \pm\sqrt{8U_p(0)\omega_0}\omega_{\text{streak}}.$$

Then the width of the measured spectrum is

$$\sigma_s = \sqrt{\sigma_{\text{XUV}} + \tau_{\text{XUV}}(s^2 \pm 4cs)}\,.$$

To determine the pulse duration of the chirped spectrum, the measured spectra have to be deconvoluted:

$$\sigma_{1,2} = \sqrt{\sigma_{s_{1,2}}^2 - \sigma_{\text{XUV}}^2},$$

and $1, 2$ refer to the different signs of the vector potential and can experimentally realized by utilizing two detectors in opposite directions. In Figure 2.15 b), the streaking spectra with a chirped XUV pulse are shown. Comparing measurement with a positive and negative slope of the vector potential (measured with two TOFs in opposite directions) shows that for a positive slope of the vector potential, the spectrum gets broader, and for a reversed slope, the spectrum gets narrower.

Solving the equations for the XUV pulse lengths gives

$$\tau_{\text{XUV}} = \sqrt{\frac{\sigma_1^2+\sigma_2^2}{2s^2}}\,,$$

and then the linear chirp rate is

$$c = \frac{\sigma_1^2 - \sigma_2^2}{8s\tau_{\text{XUV}}^2}.$$

3. Experimental Setup

In this chapter, the experimental setup for the laser-based generation of the XUV- and THz-pulses will be described. The XUV pulses are needed to photoionize the atoms and molecules in the interaction region. The THz pulse is required for THz streaking, used to obtain the timing information of the emitted photo- and Auger electrons. Firstly, a short overview of the laser system is given, whose femtosecond IR pulses are used for the nonlinear generation of XUV and THz radiation. The experimental setup of the XUV and THz-sources is described, as well as the TOF detectors and streak camera setup, which are used for the time-of-flight measurements of the electrons. In the last part, the experimental setup for the COLTRIMS measurements is described.

3.1. Laser System and General Setup

The laser system is a commercially available Ti:sapphire laser from the laser company Amplitude (Aurora CEP 1 kHz). The laser medium here is a sapphire crystal which is doped with Ti^{3+} ions. The laser system uses chirp pulse amplification [3] to generate ultrashort 25 fs pulses with a repetition rate of 1 kHz. The central wavelength is 795 nm, and the $1/e^2$-spectral width is 85.3 nm.

The system, see Figure 3.1, consists of a Ti:sapphire oscillator (Venteon Pulse One) with a repetition rate of 79.99 MHz and a mode-locked output power of about 240 mW ($\widehat{=}$ 3 nJ pulse energy). Firstly, the IR pulses from the oscillator are stretched in the all-reflective Öffner triplet stretcher, to reduce the peak intensity on the crystals in the subsequent amplifiers. Afterward, the chirped pulses are amplified with a regenerative amplifier. Additionally, the pulses are amplified by several multipass amplifiers until the required pulse energy is reached. In the regenerative amplifier, a Pockels cell is used to select the

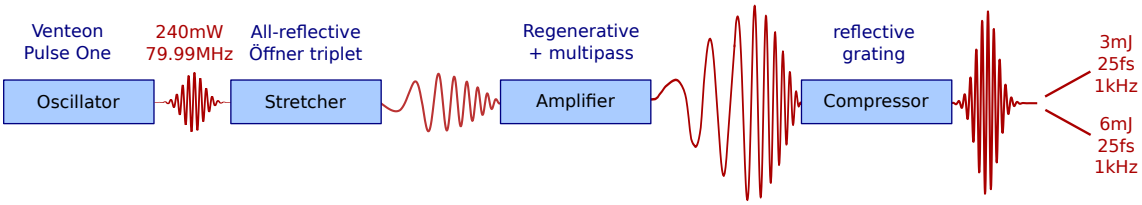

Figure 3.1.: The laser system and the available output pulse energies for the two branches with a pulse energy of 3 mJ and 6 mJ. For both output beams, the pulse length is approximately 25 fs after the compressor.

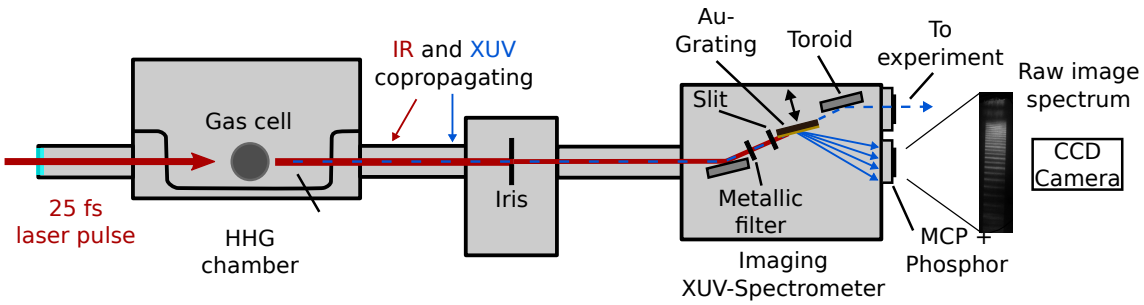

Figure 3.2.: A schematic of the generation and detection setup for high harmonic generation. The IR pulses are focused into the gas tube inside the HHG vacuum chamber. The generated XUV pulses propagate collinearly with the IR and are separated by an iris and a metallic filter (Al or Zr). The Au-grating can be moved in and out of the XUV beam path to stir the beam to the MCP-phosphor detector of the spectrometer or via the focusing toroidal mirror to the experimental chamber. For diagnostics, the harmonic spectrum is measured with a stacked MCP and phosphor detector and then recorded with a camera.

pulses to achieve a repetition rate of 1 kHz. Finally, the IR pulses are compressed using a reflective grating compressor.

The laser has two branches which have a different number of multipass amplifier stages. They deliver output pulse energies of 3 mJ or 6 mJ. In the following experiments, the pulse energy of 6 mJ was used. The laser system is placed in an adjacent laboratory to the experimental setup. The laser beam has to propagate approximately 10 meters in the air to the first vacuum chamber. So a beam stabilization system (Aligna, TEM Messtechnik) was installed to compensate for drifts of the laser system and also disturbances along the beam path to the experimental setup. Along the beam transport, the beam size is kept large to avoid nonlinear effects like self-focusing. In addition to the stabilization, stable optomechanics are used to avoid jitter.

3.2. HHG Setup

The following section describes the setup for the generation of XUV pulses (Figure 3.2) via HHG. The HHG setup was developed and assembled within this project together with Martin Ranke. The IR laser is focused by a curved mirror with focal length $f = 1.5$ m, into a vacuum chamber, through a 1 mm thick SiO_2 window. The whole process of XUV generation and propagation takes place under vacuum since the absorption length of XUV radiation in air is in the order of a few centimeters. Inside the target chamber, a thin-walled, gas-filled tube with a diameter of 3 mm is placed. The tube is filled with neon gas and is placed in the focus of the laser. Two small holes are burnt into the tube on each side where the laser has passed. This process is more precise than to drill in holes in the tube beforehand and then having to align the tube holes along the beam axis. Afterward, the laser co-propagates with the generated XUV radiation. To separate IR and

XUV radiation, an iris diaphragm is used, since the IR radiation has a greater divergence than the XUV radiation. Therefore the IR beam is larger than the XUV beam and can be spatially blocked by an iris diaphragm. The remaining part of the IR pulse is blocked by a thin metal filter, which allows a large part of the XUV radiation to pass through, but absorbs most of the IR radiation.

An imaging spectrometer is used to measure the spectrum of the generated XUV pulse. The XUV pulse is diffracted by an Au-coated grating with 1200 lines/mm, designed for photon energies of about 80 eV. The different harmonic orders are spatially separated and can be measured using a micro-channel plate (MCP) detector with an additional P46-phosphor screen. The image of the phosphor screen is recorded with a camera.

3.3. THz Setup

As described in Section 2.3.1 the generation of laser based near single-cycle THz pulses is achieved with high efficiency using a tilted-pulse front pumping scheme. The THz setup is located close to the experimental chamber to minimize transport of the THz radiation in air, which might lead to losses due to water absorption lines. For the experiments the fundamental IR beam is split into two parts, for the HHG and the THz generation, by a 50:50 beamsplitter. For the THz generation setup, the 800 nm beam is transported to the THz setup, still using 2 inch mirrors to minimize the B-integral of the beam.

For the THz generation, the beam size has to be reduced to achieve the required intensity of the pump beam in the LN crystal. The THz setup is shown in Figure 3.3. It was adapted from a design made by Anastasios Dimitriou.

In order to get a smaller beam size, a telescope consisting of a lens and a convex mirror is used. For the streaking experiments the beam path of the XUV and THz beam should have the same length to create a temporal overlap of the pulses in the interaction zone. An additional delay stage in the THz beam path is used to change the temporal overlap between the THz radiation and the XUV pulse during the streaking experiments. When the IR beam hits the grating (1800 lines/mm), a pulse front tilt is introduced. After the grating, the different wavelengths of the IR beam are spatially separated, and an achromatic focusing lens ($f_2 = 75$ mm) is used to image the beam into the MgO-doped cLNB crystal.

Several setups of the telescope were tested to change the shape and spot size at the crystal to find the best THz efficiency. Using cylindrical lenses to achieve an elliptical beam shape on the crystal could be beneficial to increase the effectively used area in which THz radiation is created, but due to limitations with the different divergence of the IR beam in the horizontal and vertical direction, see Section 4.1.5, it was hard to find a good combination of lenses and mirrors. In the end a telescope using a convex lens and sperical mirror was used to reduce the beam size.

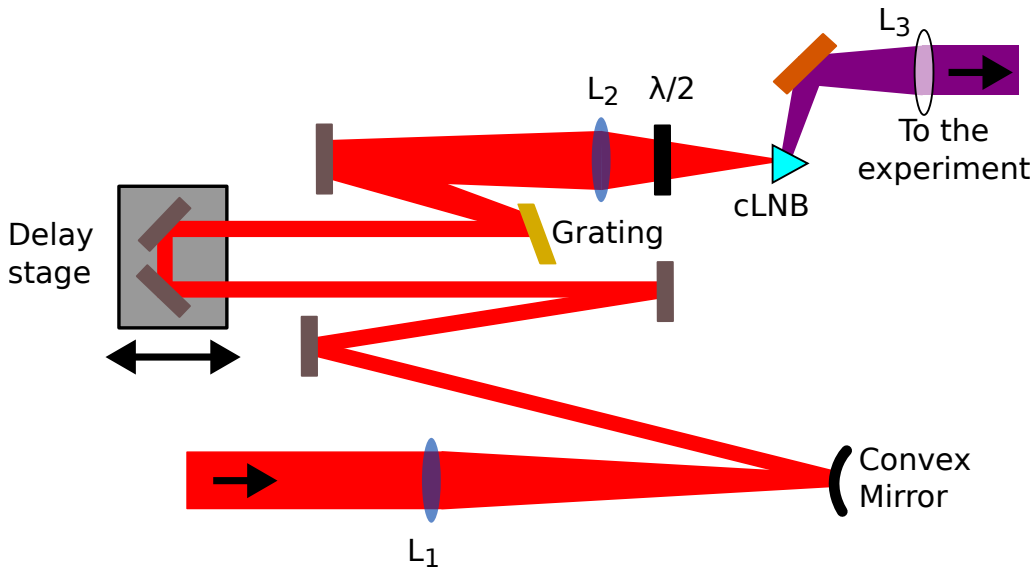

Figure 3.3.: Setup for the THz generation: The first focusing lens (L_1) and the convex mirror are used as a telescope. The delay stage shifts the time delay between the THz and XUV pulses in the interaction point. Afterward, the grating induces a pulse front tilt, and the achromatic lens (L_2) focuses the IR-radiation on the cLBN (c-cut Lithium-Niobate) crystal. Finally, the Teflon lens (L_3) collimates the generated THz radiation for further transportation to the experiment.

Before the cLNB crystal, a $\lambda/2$-plate is used to rotate the polarization of the pump beam to be parallel with the optical axis of the crystal. The THz radiation which is emitted from the crystal is highly divergent. Therefore, a PTFE lens ($f_3 = 100\,\text{mm}$) is used to collimate the beam behind the crystal. PTFE has a high transmission for THz radiation but is opaque in the visible range, which helps to block scattered IR radiation coming from the crystal. The now collimated THz beam is then guided to the experimental chamber using 2 inch copper mirrors.

3.4. Streaking Experiment

The streaking experiments are performed inside a vacuum chamber, which is placed at the interaction region of the XUV- and THz focus (determined by the position of the COLTRIMS setup, see Section 3.6). A scheme of the setup is shown in Figure 3.4. A toroidal mirror is used to image the XUV beam from its point source in the HHG chamber into the interaction zone of the experiment, without causing astigmatism. Using a spherical mirror instead of the toroidal mirror would cause more beam distortions, due to astigmatism. The toroidal mirror has two different radii for focusing in the sagittal and tangential plane. For the given grazing incidence of the XUV radiation, the radii are chosen to match the focal lengths $f_{\text{tang}} = f_{\text{sag}} = 572\,\text{mm}$ and make it possible to focus the XUV beam on a small spot. The THz radiation is coupled into the chamber using a TOPAS window with 3 mm thickness and is focused using an off-axis parabolic mirror

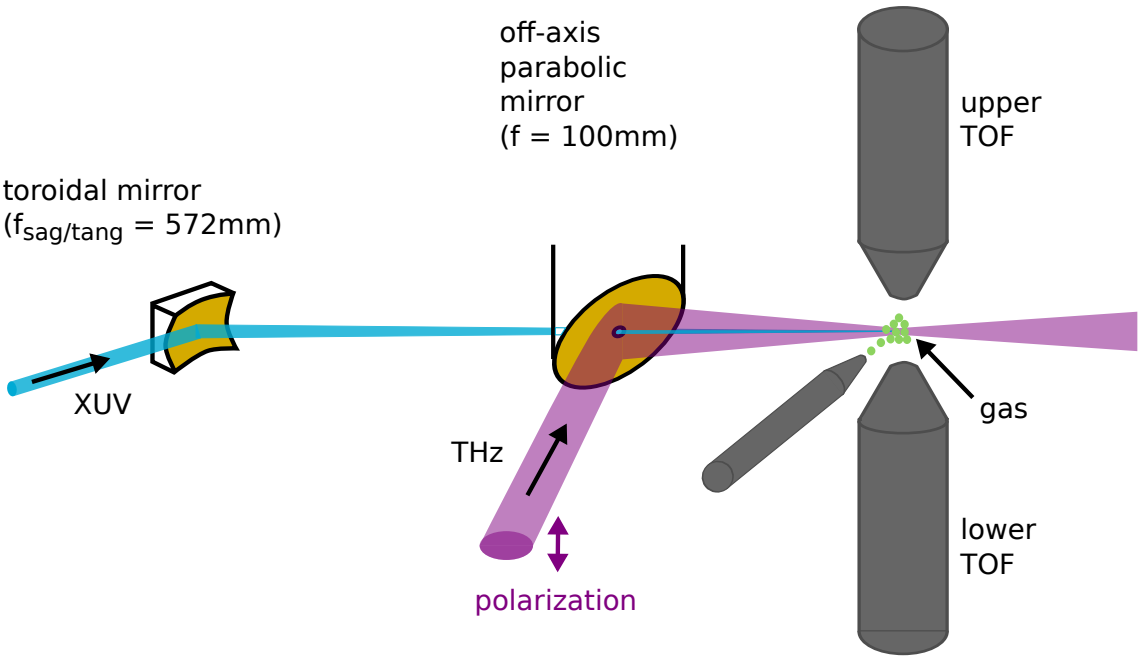

Figure 3.4.: Setup of the streaking experiment. A toroidal mirror focuses the XUV beam with a sagittal and tangential focal length of $f \approx 572\,\text{mm}$. The XUV passes through the hole of an off-axis parabolic mirror ($f = 100\,\text{mm}$), which is used to focus the THz radiation into the interaction region. The XUV ionizes the target gas, and the free electrons are measured using two TOFs. The TOFs are perpendicular to the beam and in the direction of the THz polarization.

with f = 100 mm and a small hole to let the XUV beam through. The THz radiation is s-polarized, to match the THz-polarization with the direction of the TOFs, which are placed perpendicular to the incoming beams. The target gas is supplied by a gas nozzle close to the interaction zone, and the vacuum chamber is pumped using three turbomolecular pumps, one for the main chamber and two before the flight tubes of the MCPs to achieve a back pressure in which the MCPs can be safely operated.

3.5. Electron Time-of-flight Spectrometer

Electron time-of-flight spectrometers (TOFs) measure the time of flight of photoelectrons and Auger electrons and, thus indirectly their energy. The entrance aperture of the TOFs is located about 5 mm from the interaction zone. Directly behind the entrance aperture, there are six electrostatic lenses which help to increase the transmission of the TOFs in order to collect more electrons. Furthermore, the TOFs consist of a flight tube, which is approximately 670 mm long, and at the end of the flight tube, the MCP detectors are located. The arriving electrons trigger an electron cascade with amplification factors of 10^6 - 10^7. The resulting secondary electrons hit an anode, and an anode current is generated. This current is converted into a voltage signal with the help of resistors, and an oscilloscope then measures the signal. By applying an additional retarding voltage, the flight

times of the electrons can be increased or decreased. The resolution and transmission of the TOFs are best for flight times corresponding to electron energies of about 10 eV to 30 eV, so shifting the flight times into this region increases the resolution of the TOFs.

Depending on the process, however, the original photoelectron or Auger electron energies differ from this value. Only a certain percentage of the electrons generated during the ionization process can be measured with the TOFs. The percentage depends on the acceptance angle of the TOFs. The acceptance angle is the angle between the initial momentum of the electrons and the spectrometer axis. According to simulations, the acceptance angle is in the range of 15-20° [33, 36].

Furthermore, it should be noted that a broadening of the measured energy spectra occurs due to an extended interaction zone. Electrons with the same initial energy but a different starting point follow different trajectories, and thus a broadened energy distribution is measured.

3.6. Design of the COLTRIMS Setup

One of the main goals using the lab-based XUV and THz sources was to do coincidence measurements of ICD electrons and ion fragments following the ionization of neon dimers. For these experiments, a collaboration with the group of Prof. Dr. Till Jahnke (Goethe Universität, Frankfurt am Main) was planned.

In the ICD process, a photoelectron, an ICD electron, and two positively charged ions are produced. The fragments of the process can be measured coincidentally with a COLTRIMS (Cold Target Recoil Ion Momentum Spectroscopy) detector, using two time- and position-sensitive detectors for detecting negatively and positively charged particles.

The COLTRIMS detector, see Figure 3.5, (also called Reaction Microscope) is used to measure the momentum vector and charge state of charged particles emerging from an ionization event in coincidence. In the intersection region, a supersonic gas beam and an XUV-beam are crossed at a right angle, and the created ions and electrons are guided by electric and magnetic fields to large area position- and time-sensitive detectors. The electric field is generated by ring-shaped electrodes along the flight path of the particles inside the vacuum chamber, and the magnetic field is produced by large Helmholtz coils, which are placed around the vacuum chamber. The electrons fly along a circular path, due to the magnetic field, which confines them inside the volume of the spectrometer. From the measured time and position, the kinetic energies and the emission angle of the electrons can be calculated. For the fragment ions, the kinetic energy release (KER) and the fragmentation direction can be calculated. The KER can give insight into the internuclear distance at the instant of ICD emission.

Since the ions and electrons which are detected should come from the same atom or molecule, the target density and the ionization rate should be adjusted to ensure that the

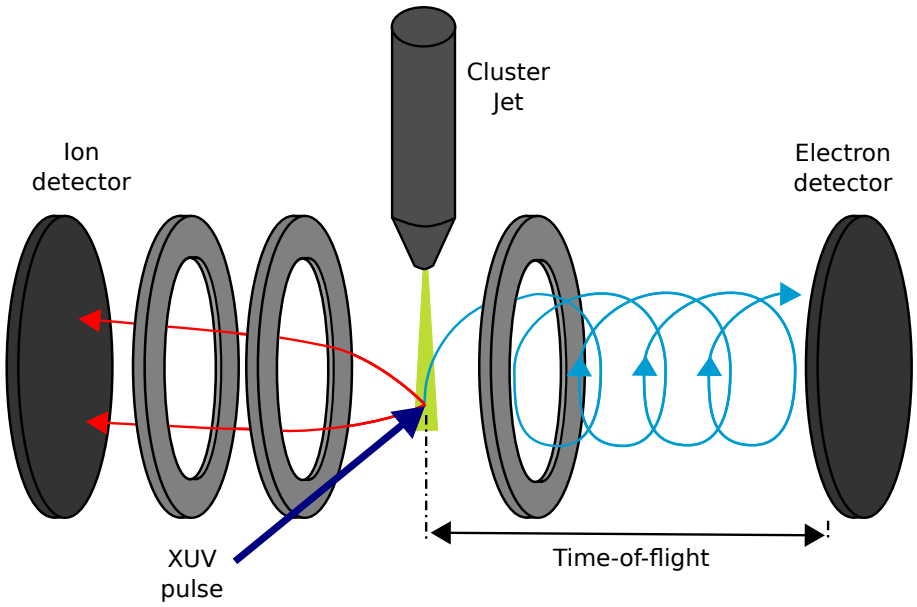

Figure 3.5.: Charged particles are created by ionizing atoms or molecules of a supersonic gas jet with an XUV beam. The charged particles are then guided to large position- and time-sensitive MCP detectors by magnetic and electric fields.

reaction rate is much below one per ionizing pulse. The dimer-to-monomer ratio of the target gas, additionally influences the effectively measurable ICD events.

Performing experiments with lab-based XUV and THz sources places several requirements and also restrictions on the setup:

- The relatively low repetition rate of the laser (1 kHz) compared to other sources like synchrotrons (several MHz) may lead to much longer measurement durations, therefore the stability of the setup is of extreme importance.
- The THz beam transportation is sensitive to air (water absorption lines) so beam transportation outside the vacuum should be minimized.
- The long wavelength of the THz ($\lambda_{1\mathrm{THz}} = 0.3\,\mathrm{mm}$) radiation makes it harder to achieve a small focal size, so shorter focal lengths or higher THz intensity are needed.
- Due to the confined laboratory space, some experimental parts must be removable and easily reassembled.

The planned setup is shown in Figure 3.6, where the COLTRIMS detector should be placed next to the optical table, in a row with the HHG and the spectrometer chamber. Again, the beam path is split in front of the HHG chamber with a 50:50 beamsplitter to provide equal pulse energy for the generation of the XUV and THz pulses. In our setup, the XUV beam is focused using a toroidal mirror, whereas in other experiments, a multilayer mirror is used. With multilayer mirrors, the XUV is sent at a slight angle through the experimental chamber and then refocused into the interaction zone. This setup is not

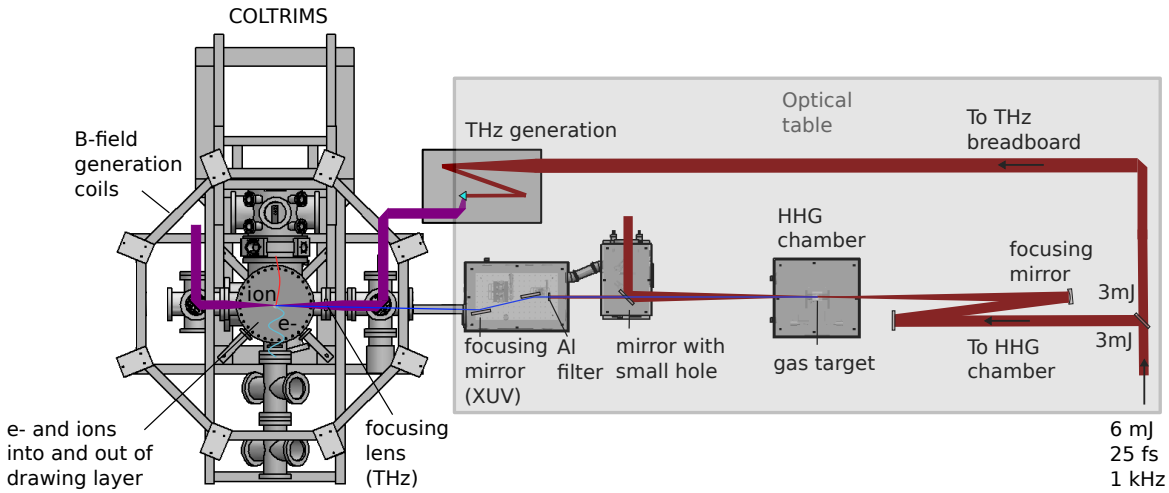

Figure 3.6.: Planned experimental setup with COLTRIMS detector. The XUV pulses ionize the target beam, while the electric field of the THz pulses induces a momentum change on the electrons to map the temporal information onto the electron momentum. Guiding the charged fragments (ions and electrons) with electric fields into and out of the drawing layer to the time- and position-sensitive detectors.

possible with COLTRIMS, since the copper plates of the spectrometer inside the main vacuum chamber do not allow a setup like this, due to unwanted ionization events of the XUV beam passing the chamber. The spectrometer is made of several copper plates, which are spaced approximately 5 mm, to form the electric field. Sending the XUV beam twice through the experimental chamber might lead to noise due to unwanted ionization events. In this setup, we chose a toroidal mirror for focusing. The mirror is broad-band reflective, and therefore a wide range of harmonics can be used for the experiments. This increases the number of photons in the interaction region but also has the disadvantage of having photoelectrons at different energies for each harmonic.

Another reason, why the spectrometer places difficulties on the setup is the THz incoupling. Since THz radiation has really long wavelengths compared to visible light or light in the XUV region, it is harder to get a small focus. The beam waist ω_0 scales linearly with the focused wavelength. To achieve a small focus size, focusing with shorter focal lengths would be beneficial. The experimental interaction region spanned by the supersonic gas jet and the perpendicular XUV beam is about $1\,\mathrm{mm}^3$ in size. In this region, the THz should be homogeneous to have similar streaking speeds for all electrons and correctly map the timing information onto the momentum of the electrons.

Having a too large focal size also reduces the achievable streaking speed, which leads to a lower temporal resolution. Then the change in momentum is too low in comparison to the spectral width of the peaks and might not be resolved.

In Figure 3.7, the focal size, and the radial intensity distribution are plotted for three different focal lengths. In similar experiments [21, 37] using light-field streaking with

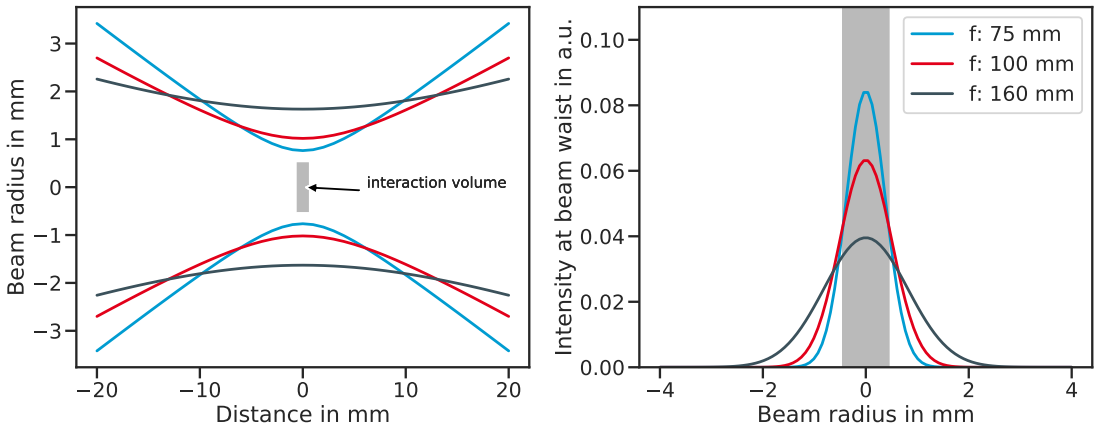

Figure 3.7.: Left: Size of the beam radius along the beam propagation direction with an initial beam diameter of 30 mm for different focal lengths. Blue corresponds to f = 75 mm, red to f = 100 mm and gray to f = 160 mm. Right: The intensities at the beam waist (at longitudinal position z = 0) for the different focal lengths. The intensity distribution for the THz focus is assumed to be Gaussian. In both plots, the gray area corresponds to an interaction volume of approximately 1 mm^3.

THz, the THz radiation was focused using lenses or parabolic mirrors with focal lengths of 75 mm or 100 mm. Due to the size of the vacuum chamber for COLTRIMS (with a diameter of $d = 300$ mm), which houses the spectrometer made of copper plates, it is not possible to place a focusing lens or mirror very close to the interaction zone inside the vacuum chamber. Therefore, a setup where a focusing lens could be placed as close as 7160 mm to the interaction zone was designed, see Figure 3.8. Comparing the waist size for $f = 75$ mm and for $f = 160$ mm, an increase from $w_0 = 0.64$ mm to $w_0 = 1.36$ mm is expected. Therefore the maximum intensity in the interaction zone decreases, which leads to a lower streaking speed and negatively influences the time resolution of the measurements.

The electrons and ions are guided by electric fields to the detectors, which are perpendicular to the XUV beam and along the direction of the THz polarization. An additional set of generation coils is placed around the vacuum chamber. It generates the magnetic field to confine the electrons inside the chamber.

Due to the confined space of the laboratory, the THz breadboard, which should be as close as possible to the experimental chamber to reduce THz beam transportation in air, had to be placed on an extra breadboard. The breadboard protrudes beyond the table and can be removed to set up the COLTRIMS chamber and then be reinstalled afterward.

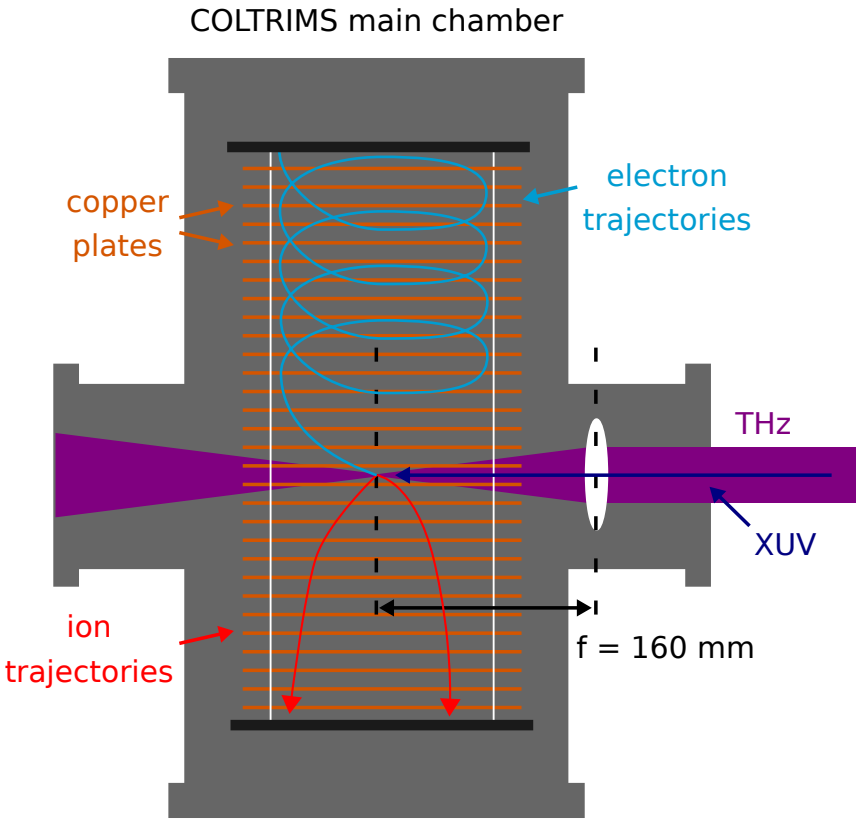

Figure 3.8.: COLTRIMS setup with the THz lens with f = 160 mm. The copper plates of the spectrometer prevent the THz lens from being placed closer to the interaction zone. Along the beam propagation, parts of the copper plates must be cut to avoid disturbances from the THz field (cuts not shown in plot).

4. Characterization of the Light Sources

There are certain requirements for the XUV and THz sources in order to perform the time-resolved measurements. They need to have a stable pointing and the intensity should not fluctuate too much between shots. In this chapter, the performance and stability of the sources is evaluated. The XUV beam properties in the interaction point are also measured. Its focus needs to be small enough that the THz-field is relatively constant and the electrons originate from approximately the same point. This was also investigated in the next chapter.

4.1. High Harmonic Source

At first, the performance of the HHG is evaluated. One important property of the source is the achieved cutoff-energy, which is the energy of the highest harmonic order. A spectrometer was placed in the vacuum chamber behind the high harmonic generation to examine the output of the XUV, see Figure 3.2. The spectrometer, which consists of a movable grating and a MCP detector, can be used daily to examine the performance of the XUV generation. With the movable grating, the beam path can be switched inside the vacuum. The beam can either be guided to the experimental chamber or to the diagnostics setup, where the high harmonic spectrum can be measured.

4.1.1. Spectrum

The spectrum of the high harmonics can be measured using a diffraction grating which spatially separates the different wavelength components of the high harmonics. For a wave with an incident angle α to the normal of the grating, the grating equation is given by:

$$d(\sin\alpha - \sin\beta_m) = m\lambda,$$

where d is the spacing between the slits (the grating period), m the order of diffraction, and β_m is the diffraction angle.

The setup used for the measurements is shown in Figure 3.2, where the harmonics are first separated from the fundamental IR beam using an iris and an additional metallic filter (Al or Zr), which can not only be used to block the fundamental beam, but also help determine the order of the harmonics. A slit before the grating helps to illuminate only a limited number of grooves on the gold-coated grating, so the different wavelengths have

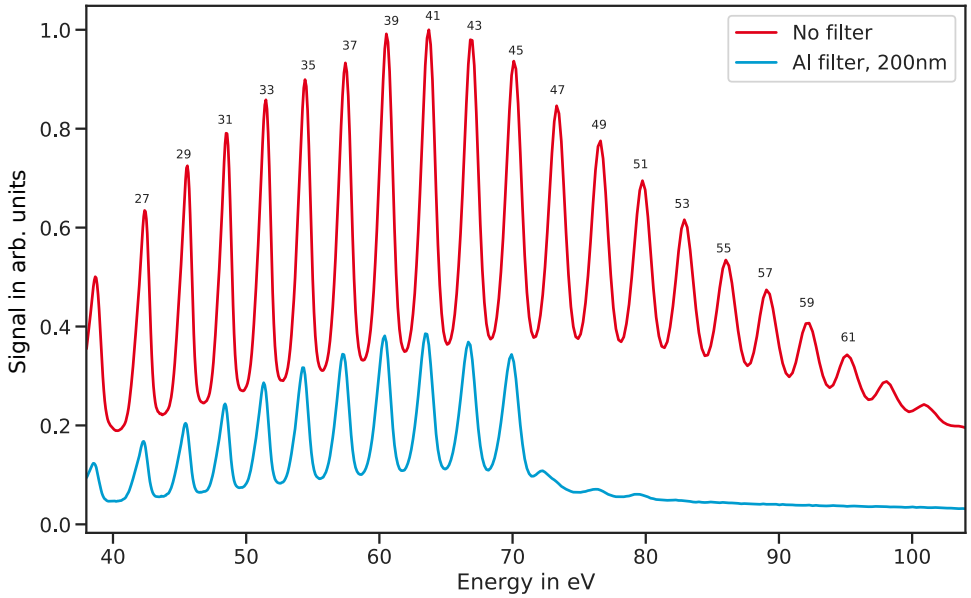

Figure 4.1.: A spectrum measured with the imaging spectrometer with and without a 200 nm thick aluminum filter. The aluminum transmission has a clear cutoff between the 45th, and 47th harmonic and can be used to determine the harmonic orders of the measured spectra. The lower harmonics' signal strength is dominated by the smaller reflectivity of the Au-grating for low-energy harmonics; therefore, the harmonics in the plateau-region seem to have a weaker intensity for lower harmonic orders.

a confined space of origin and can be clearly separated on the phosphor screen. A spectrum which was measured using this setup is shown in Figure 4.1. The measurements were performed with and without an Al filter to determine the order of the harmonics.

Incoming and outgoing angles on the grating cannot be measured precisely. Therefore, the exact position of each harmonic order of the grating is not known. Aluminum has a clear edge for the transmission of radiation in the XUV range around 70 eV. For our fundamental wavelength λ = 800 nm, the cut-off lies between the 45th and 47th harmonic of the spectrum. Using an aluminum filter and determining which harmonics are absorbed helps to label the peaks. This information is used to calibrate the x-axis, and the measured spectrum can then be plotted over the energy-axis instead of the measured pixel position.

The signal height of the spectrum is determined by the reflectivity of the Au-coated grating. The reflectivity is not constant over the measured energy range, and therefore the measured HHG spectrum does not show the expected behavior with a plateau region and the cut-off energy. The amplitudes must be corrected for the reflectivity of the grating to get more accurate peak heights. Unfortunately, the MCP-phosphor detector is not calibrated, so it does not give an absolute number for the energy of each harmonic.

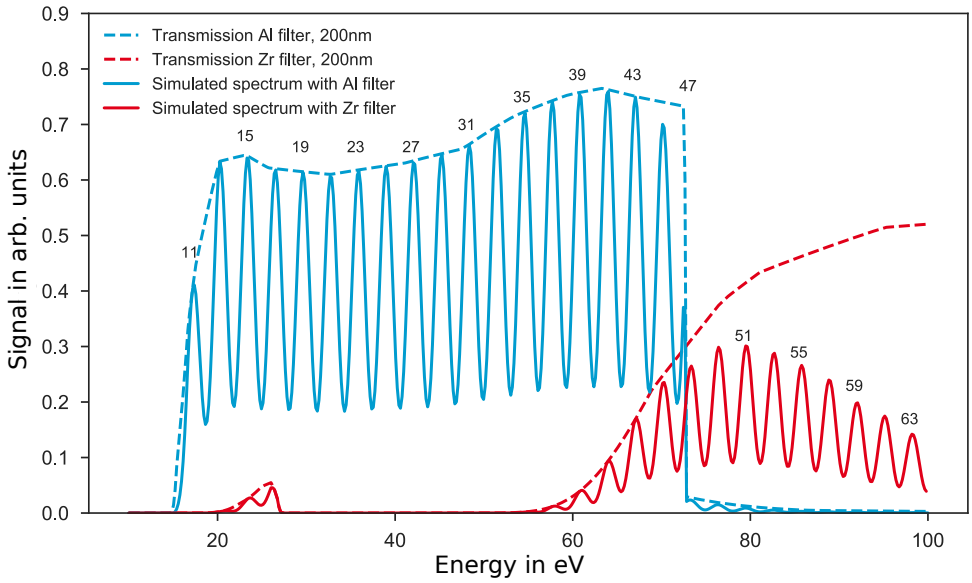

Figure 4.2.: A calculation of the spectra after a 200 nm thick Al or Zr filter.

Therefore, the XUV pulse energy is measured using a XUV photodiode (see Section 4.1.2). Nevertheless, the detector can be used to tune the harmonic source to increase the overall output and determine the cut-off of the HHG.

Different harmonic orders can be selected for the measurements depending on the target gas and the type of experiment which should be performed. The mirrors used along the beam path of the XUV are spectrally broad, and no multilayer mirrors are used. Therefore the range of the harmonic spectrum can be selected using different metallic filters. In our setup, it is possible to switch between an aluminum or a zirconium filter (each with a thickness of 200 nm). In Figure 4.2, the resulting spectra after the filters are plotted. An aluminum filter can be used to select the orders 11 to 45 of the harmonic spectrum and with the zirconium filter, harmonics having an energy of 60 eV or higher can be selected. It has to be noted that the initial spectrum in Figure 4.2 was simulated since it is not possible to measure the whole range of the harmonic orders from 11 to 61 with the spectrometer setup at the same time. The problem is the limited size of the MCP detector, which is too narrow for the whole spectrum and also the aforementioned bad reflectivity of the Au-coated grating for lower harmonics.

With this setup, it is impossible to select a single harmonic (which is often done in experiments which require one ionization energy), since neither a multilayer mirror nor some type of monochromator setup is used. Therefore, a broad range of harmonics is used to ionize the target gas, which leads to different photoelectron energies for each harmonic. The influence on the analysis of the measured electron spectra is discussed in Chapter 5.

4.1.2. Pulse Energy

To get a measurement of the pulse energy of the high harmonic pulses, a photodiode which is sensitive in the XUV range was used. The diode (SPD-1UVHCM, Technoxan Ltd.) has an amplifier gain of 1.1 mV/fC and a spectral responsitivity of 0.25 A/W for photons of 80 eV energy. The spectral curve is approximately flat for the measured spectral range, so we assume the responsitivity to be approximately the same for all harmonics.

The measurements of the pulse energy were performed in the focal point of the toroidal mirror, where the experiment's interaction point will be.

The energy can be calculated from the measured signal of the XUV diode by:

$$E_{\mathrm{XUV}} = \frac{\text{measured voltage}}{\text{amplifier gain} \times \text{spectral response}}.$$

For a specific harmonic order, the energy of a single photon can be calculated by:

$$E_{\text{single photon}} = \frac{hc}{\lambda_{\mathrm{XUV}}}.$$

Then the number of photons is given by:

$$\text{Number of photons} = \frac{E_{\mathrm{XUV}}}{E_{\text{single photon}}}.$$

Depending on the combination of filters that were used, we can select a different range of harmonics. So, in this case, not a single harmonic was measured, but a range of harmonics. The percentage of each harmonic of the total harmonic signal needs to be known to calculate the number of photons for a single harmonic.

Using the harmonic spectrum measured in Figure 4.1 and taking into account the different transmissions of the metal filters, the contribution of each harmonic to the total signal can be estimated.

Finally, the pulse energy for each harmonic and the number of photons for each harmonic can be calculated if the different single-photon energies of the harmonics are taken into account.

After two aluminum filters a voltage of $\Delta V = 355$ mV was measured. The total energy of all harmonics is then:

$$E_{\text{XUV, all harmonics}} = \frac{355\ \text{mV}}{1.1\ \text{mV/fC} \times 0.25\ \text{A/W}} = 1.3\ \text{pJ}.$$

The aluminum filters transmit the harmonics of the orders 11 to 45, so a total of 18 harmonics. Assuming that each harmonic contributes equally to the total pulse, as this is in

Table 4.1.: Number of photons in the interaction zone using an aluminum filter.

harmonic order	number photons
11	26250
13	22210
15	19250
17	16980
19	15195
21	13750
23	12550
25	11550
27	10690
29	9960
31	9315
33	8750
35	8250
37	7800
39	7400
41	7040
43	6710
45	6420

the plateau region of the high harmonic spectrum, see Figure 4.2, then each harmonic has a pulse energy of approximately:

$$E_{\text{single harmonic}} = \frac{E_{\text{XUV, all harmonics}}}{18} = 72.2 \text{ fJ}.$$

The number of photons for each harmonic is calculated by dividing with the energy of a single photon. In Table 4.1, an overview of the number of photons expected in the interaction zone is shown. For the ICD experiments, electrons from the 2s orbital of neon need to be removed. The binding energy of the neon 2s orbital is 48.5 eV. Therefore the 33rd up to the 45th high harmonic orders (with the Al filter) contribute to the process. The expected number of electrons from these 7 harmonic orders is around $N_{\text{photons, 33rd to 45th order}} = 52000$ per pulse in the interaction point.

4.1.3. XUV Focus

Another important beam property is the focal size of the XUV and THz beams in the interaction zone. The XUV beam size should be noticeably smaller than the THz focus, so that the THz electric field is uniform over the whole interaction region. The XUV focus was measured using a MCP-phosphor detector, placed in the interaction zone of the toroidal mirror. The toroidal mirror is placed with a certain distance to the interaction

zone and the source of the HHG. The thin lens equation determines the distances:

$$\frac{1}{b} + \frac{1}{g} = \frac{1}{f},$$

where b is the image distance, g is the object distance, and f is the focal length of the toroid (for both the sagittal and tangential direction). The object, which is the source of the harmonics in the HHG chamber, is imaged with a magnification factor given by $m = b/g$.

A picture of the XUV focus is shown in Figure 4.3. The XUV focus seems to be elliptical in the interaction region, so a Gaussian fit is used to determine the horizontal and vertical beam size. The horizontal beam size is $w_{0,x} = (85 \pm 4)$ μm and the vertical beam size is $w_{0,y} = (204 \pm 7)$ μm. The vertical beam size is relatively large, but still good enough, since the interaction zone has roughly a size of 1 mm^3.

As follows from the thin lens equation, the XUV focus should be an image of the focus of the fundamental beam during the high harmonic generation. So the elliptical shape might come from a misalignment of the toroidal mirror or could be a property of the fundamental beam, see Section 4.1.5.

4.1.4. XUV Stability

Evaluating the data from the focus measurements with the MCP over several pulses shows the pulse energy stability and also the pointing stability of the focus. The signal was integrated over 15 pulses since the MCP-camera setup was not sensitive enough to record single shot pictures. It is clearly visible that the intensity changes quite a bit between zero and the saturation value of the camera sensor, see Figure 4.5. For our measurements, this is no problem. With the TOFs, the spectra usually are an acquisition of several thousand shots, so only the average count rate is important. For the ICD experiments, only those measurements with only one photoelectron, one ICD electron, and the two ion fragments are used for the analysis. If the HHG intensity fluctuates, there might be a few more shots without signal. This might slightly increase the measurement time to measure a complete spectrum, but the intensity fluctuations of the HHG are not a general problem for the measurement principle.

The fluctuation of the XUV pulse intensity is also observed while measuring the XUV harmonic spectrum. They might result from fluctuations in the intensity of the IR beam coming from the laser amplification process and might be stronger due to the nonlinear nature of the high harmonic generation. Another possible source for the fluctuations might be the gas pressure during the HHG process, as the gas pressure might not be constant shot-to-shot, and therefore the XUV intensity might fluctuate.

To examine the pointing stability of the XUV pulse in the focal region, again, the Gaussian fit, as shown in Figure 4.3 was performed for each measurement, and the center position was taken. The center positions in the horizontal and vertical direction are shown in

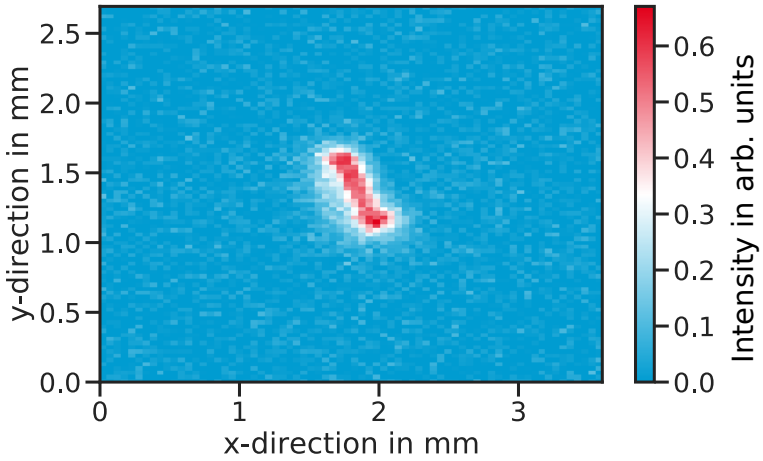

Figure 4.3.: Focus size of the XUV pulse at the interaction point. Measured using a MCP-phosphor detector and a Basler camera.

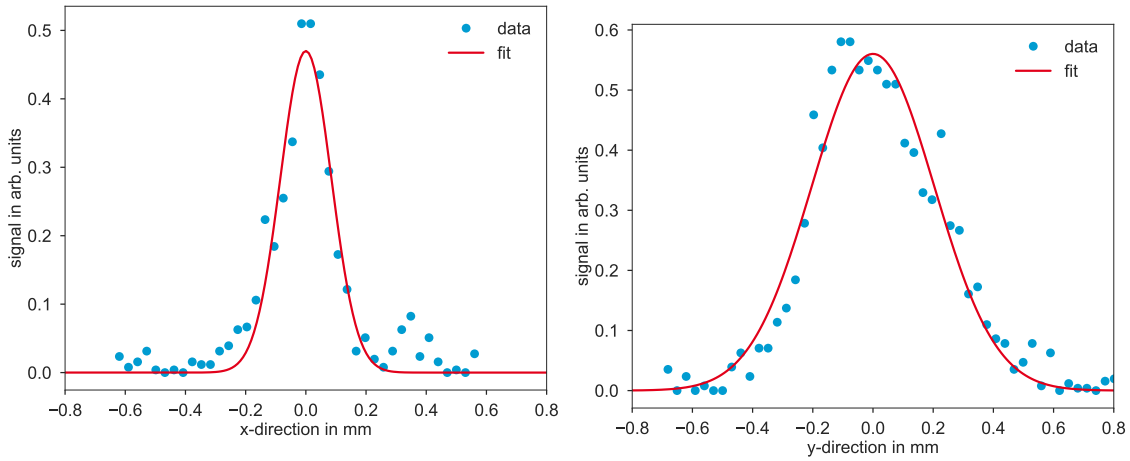

Figure 4.4.: Beam radius of the XUV beam in horizontal and vertical direction. The data is fitted assuming a Gaussian shape to get the horizontal $w_{0,x}$ (left) and vertical $w_{0,y}$ (right) beam waists.

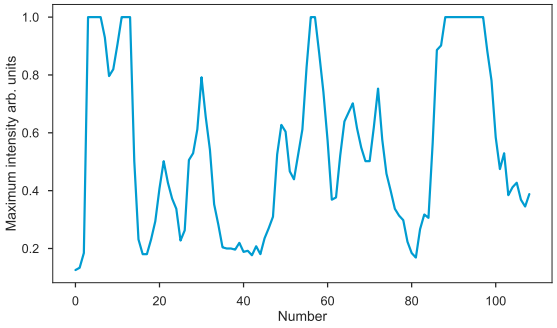

Figure 4.5.: The intensity of consecutive pictures taken with a MCP detector. Each measurement is integrated over 15 pulses, since the single shot single was too low to detect.

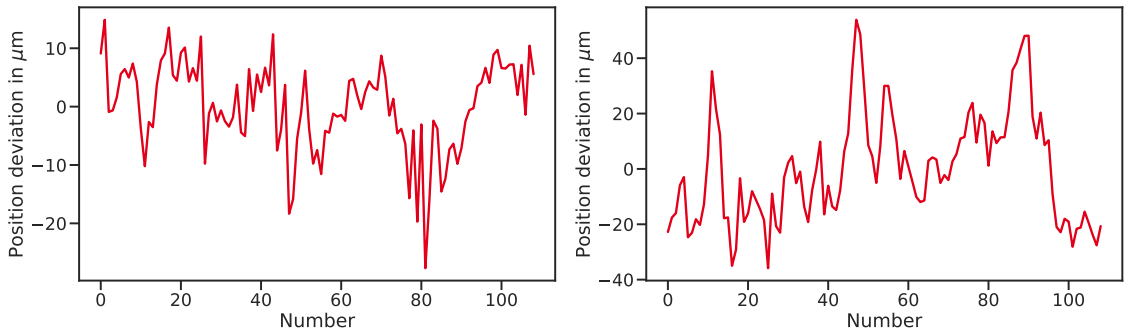

Figure 4.6.: Center position of the XUV focus obtained by the Gaussian fit in horizontal (left) and vertical (right) direction.

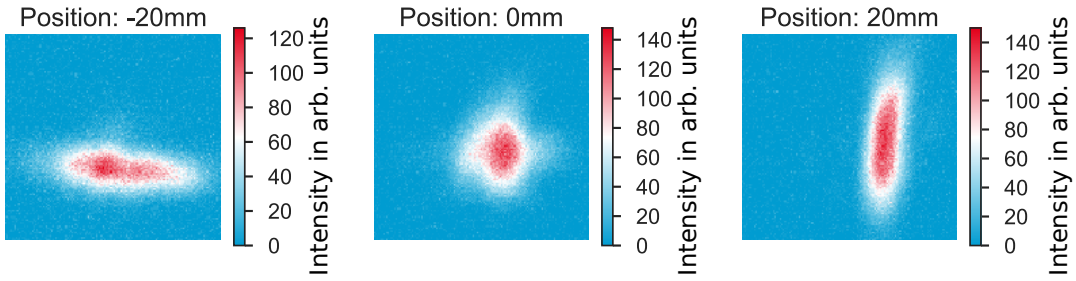

Figure 4.7.: Focus of the fundamental beam at three different positions along the beam path. The vertical and horizontal foci are not at the same point which is a sign for astigmatism. The beam is shown at the positions: z = -20 mm (left), 0 mm (center), 20 mm (right).

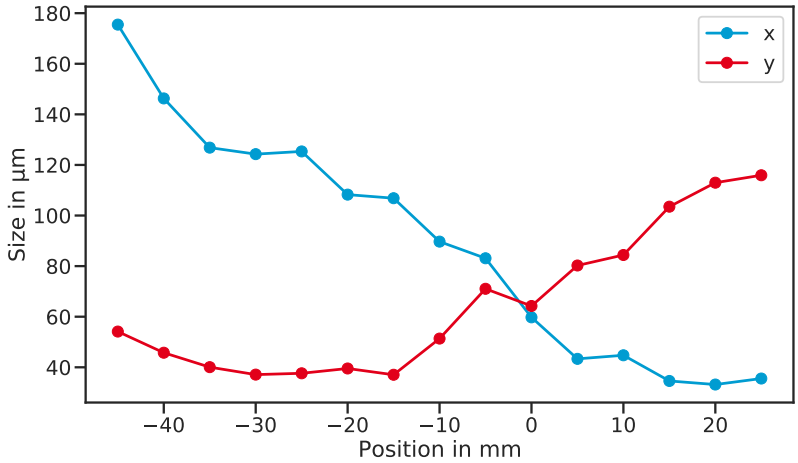

Figure 4.8.: Focus size of the fundamental beam in the high harmonic chamber along the propagation direction. For the horizontal (x) and vertical (y) direction.

Figure 4.6. The standard deviation of the focus position in horizontal direction is Δx_{cen} = 10.8 μm and in vertical direction $\Delta y_{\text{cen}} = 23.0$ μm. This is about 1/10th of the beam size.

The pointing stability seems to be satisfactory, which might come from the fact that for the IR beam, a beam stabilization system is used (Aligna, TEM Messtechnik). It is placed in front of the HHG chamber before the IR beam is coupled into the vacuum chamber. The stabilization system corrects beam fluctuations along the several meters long beam transport from the laser compressor to the vacuum chambers.

4.1.5. Focus of the Fundamental Beam

To get a better understanding of the shape of the XUV focus, the focus of the IR beam in the HHG chamber was investigated. A measurement of the focus of the IR beam in the HHG chamber was performed using a beam profile analyzer (Thorlabs). The results are shown in Figure 4.7 and Figure 4.8.

Along the propagation direction through the focus, the beam profile is initially highly elliptical with the long axis parallel to the optical table, then becomes almost circular and finally elliptical with the long axis perpendicular to the optical table (Figure 4.7). This kind of optical aberration, where the foci are spatially apart, is called astigmatism. Astigmatism describes an optical system, where rays coming from two perpendicular planes have different foci. Often high harmonic sources are operated so that the gas cell is behind the focus of the beam. So it might be possible that the gas cell is placed at a position where the beam is elliptical. This is only a guess since the harmonic source was optimized by shifting the gas cell, so its exact position regarding the IR focus is unknown.

Astigmatism might result from several factors:

- **Different divergence in horizontal and vertical direction:** Measurements of the beam radius and divergence before the HHG chamber shows that the beam is already elliptical and also has different divergence in horizontal and vertical direction. The beam radius was measured using a knife-edge scan, where a sharp blade is used to block some parts of the beam while measuring the resulting power behind it. The results are shown in Figure 4.9.

  The radius in horizontal direction is $r_x = (11.1 \pm 0.1)$ mm and in vertical direction is $r_y = (9.04 \pm 0.09)$ mm. The knife-edge scan was performed at different positions along the beam path of the fundamental IR beam to calculate the divergence of the beam, see Figure 4.10. The beam radius was measured directly after the compressor and several meters along the beam line. Since the measurements were performed after the compressor, it was assumed that the divergence is approximately the opening angle of the beam size.

  In Figure 4.10 (right side) the difference in focal length due to different divergence of the beam in horizontal and vertical direction is plotted. The difference for a nominal focal length of $f = 1500$ mm is $\Delta f_y = +27$ mm and $\Delta f_x = +46$ mm, so the difference due to the different divergence of the beam is approximately $\Delta f = 19$ mm.

- **Imaging errors from focusing mirror:** When light hits a spherically curved mirror under a substantial angle against the optical axis, additional astigmatism is introduced. Due to some geometric constraints, the incidence angle on the focusing mirror is approximately $5.5^\circ - 6^\circ$.

  The difference in the focal lengths coming from rays in the sagittal (horizontal) and tangential (vertical) direction causes two foci at positions S and T, see Figure 4.11 a). Figure 4.11 b) shows the difference between the sagittal and the tangential rays in dependence of the incidence angle on the concave mirror for a radius of curvature of $r = 3000$ mm. The astigmatism leads to a difference between the sagittal and tangential focus of about 13.8 mm - 16.5 mm.

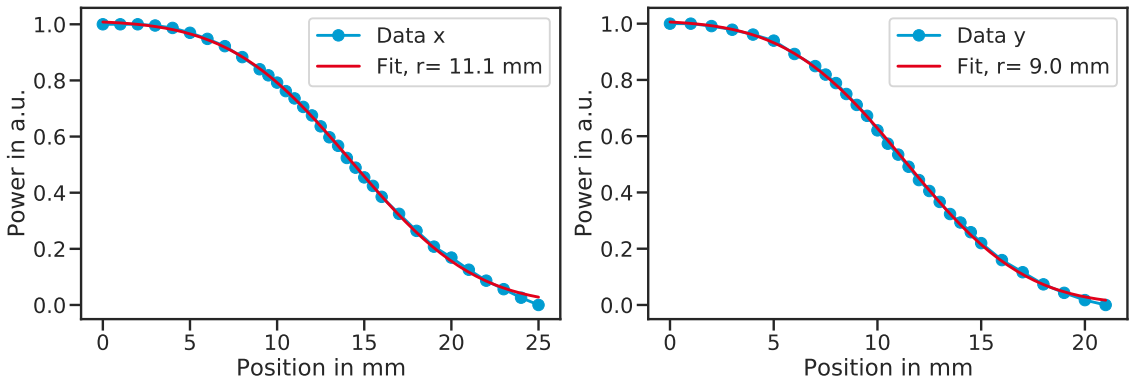

Figure 4.9.: Power measured performing a knife edge scan. The fit gives the beam radius of fundamental IR beam in horizontal (left) and vertical (right) direction.

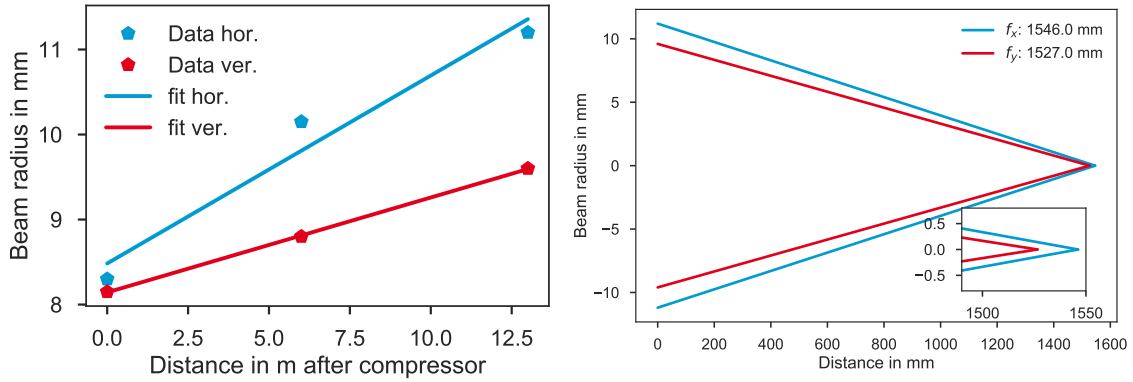

Figure 4.10.: Left: Beam size of the fundamental beam at different positions behind the exit of the compressor for the horizontal (blue) and vertical (red) beam direction. A fit to extract the slope can be used to give an estimate of the divergence of the beam in horizontal and vertical direction. Right: Different horizontal and vertical foci due to different divergence of the fundamental beam in horizontal and vertical beam direction.

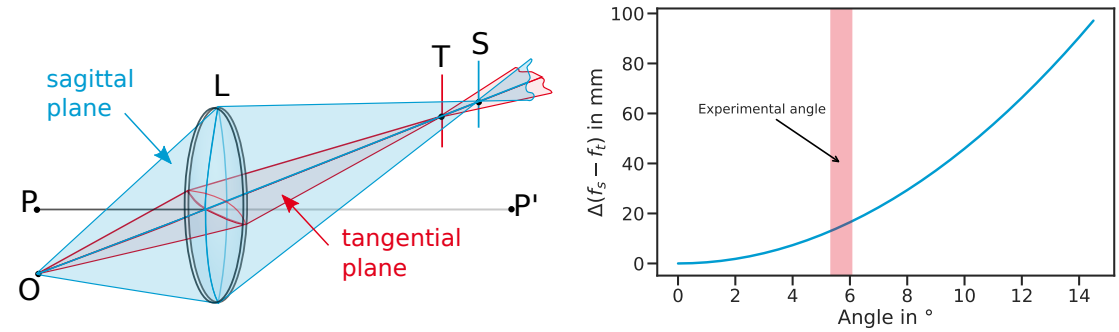

Figure 4.11.: a) Due to off-axis rays incident upon spherical lenses and spherical curved mirrors, rays from the sagittal and tangential plane have different foci at positions T and S. b) Difference between the sagittal and tangential focus due to astigmatism caused by an incidence angle differing from zero on a concave mirror with a curvature of $r = 3000$ mm.

4.2. THz Source

In order to perform streaking experiments, the THz beam's focus should be small enough to achieve sufficiently high intensities. Furthermore, the focus position and intensity should be stable during the measurements. The following section describes the results from the characterization measurements of the THz beam.

4.2.1. Stability and Pulse Energy

Several measurements were performed to examine the stability of the THz pulse. The fluctuations of the intensity can be measured using a pyroelectric detector. The detector is based on a crystal with the ability to generate a transient voltage when it is heated or cooled. For the intensity measurements, the pyroelectric detector was placed in the THz beam's focus, and the generated voltage of the crystal was measured using an oscilloscope. The fluctuations over 1000 consecutive pulses are shown in Figure 4.12 a). The standard deviation of the intensity is approximately 5.9%.

The measured fluctuations could be a property of the beam or be due to the measurement method. Pyroelectric detectors do not measure the incident radiation directly but only respond to the generated heat. Therefore they are sensitive to fluctuations of the ambient temperature. A reference measurement, measuring the ambient temperature fluctuations simultaneously would be needed to eliminate this effect. Since no reference measurements were performed simultaneously, another measurement setup was used to verify if the fluctuations are caused by intensity fluctuations of the THz beam.

This method measures the electric field of the THz pulse directly. The results of the electro-optical measurements are shown in Figure 4.12 b). In electro-optical crystals, a change of polarization is induced by the electric field of the pulse. The change in this polarization can be translated into a voltage. The voltage was measured over several consecutive pulses. Again, a standard deviation of approximately 6.6% was measured. Since electro-optic measurements are direct measurements of the electric field of the THz pulse, the fluctuations are a real effect of the beam and not caused by the measurement method. The results of the electro-optic measurements are described in Section 4.2.3 in more detail. Fluctuations in the THz electric field strength might influence the streaking measurement, as the measured shift in electron kinetic energy is proportional to the THz electric field. Since the fluctuations are symmetrical, this will broaden the peaks in the electron spectra measured with THz, but should not distort the results, as the center position of the peak stays the same.

4.2.2. Divergence and Focus

It is important to know the focus of the THz beam, since it influences the achievable streaking speed and therefore the timing resolution of the measured streaking spectra.

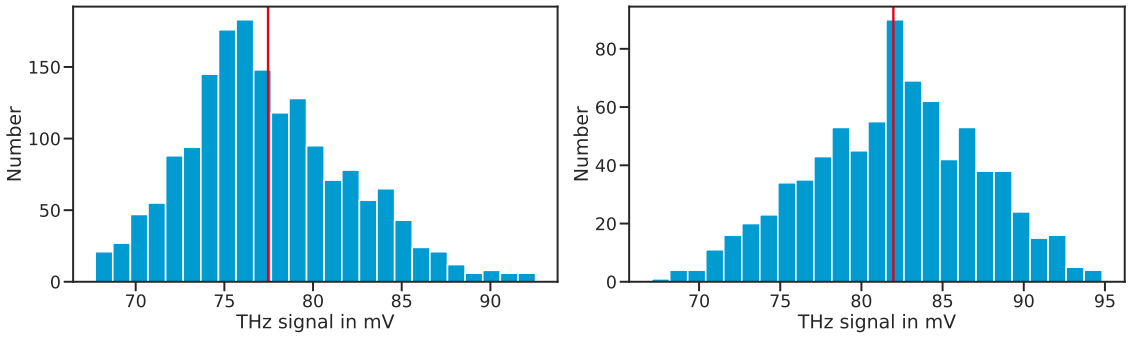

Figure 4.12.: a) Voltage of the pyroelectric detector for 1000 consecutive pulses. The standard deviation is approximately 5.9%. The intensity of the pulses is measured indirectly. b) Voltage induced in electro-optical crystal, which directly depends on the electric field of the THz pulse. The standard deviation is approximately 6.6%. The average generated voltage is plotted in red.

The focus size depends on the collimation of the THz beam and the alignment of the off-axis parabolic mirror, which is used for focusing the THz beam. A measurement of the THz focus at the interaction zone was performed using a Pyrocam III (Ophir Spiricon, pixel pitch 80 μm). This camera consists of a pyroelectric array of size 12.8 mm $\times$ 12.8 mm, so the whole THz beam in the focal region can be measured. The camera was used to optimize the focus in the interaction region of the experimental chamber. A measurement of several accumulated pulses with the Pyrocam is shown in Figure 4.13.

The focus appears to be nearly circular, but fitting the horizontal and vertical beam size by assuming a Gaussian beam profile gives a horizontal beam radius of $w_{0,x} = (0.99 \pm 0.02)$ mm and a vertical beam radius of $w_{0,y} = (0.82 \pm 0.01)$ mm. Compared to the measurements of the beam waist which were performed using EOS, see Section 4.2.4, the measured beam waist with the Pyrocam is smaller. The Pyrocam can only measure signals above a certain threshold, so the tails of the intensity distribution are below the threshold and the measured beam size appears to be smaller.

4.2.3. Electo-optic Sampling

It is useful to measure the electric field of the THz pulse to get some information about the beam parameters, such as the maximum electric field strength, which determines the achievable streaking speed for THz streaking. Electro-optic sampling can be used to measure the electric field of the THz pulse. Electro-optic sampling depends on the electro-optic effect, which describes the change of the refractive index in a material due to an electric field, see Section 2.3.4. It can be measured using a setup, as shown in Section 3.3, where a balanced detector setup is used to measure the signal. The delay between the THz pulse and the XUV pulse can be changed using the translation stage in the THz setup, and the THz electric field can be measured in the time domain. It is shown in Figure 4.15. Calculating the Fourier transform (FFT) of the electric field gives the amplitude spectrum of the THz pulse, see Figure 4.16. Since the trailing edge of the

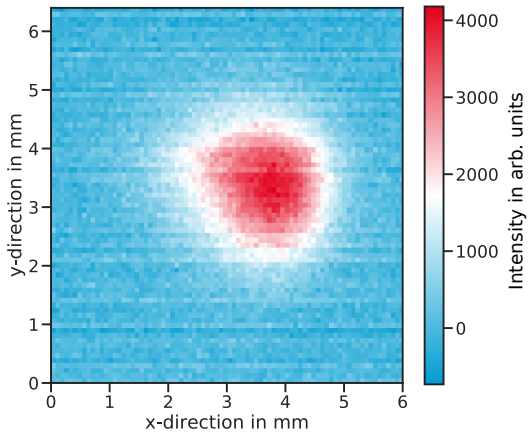

Figure 4.13.: Accumulated measurement of the THz focus at the interaction zone of the experiment, measured with a Pyrocam III. The focal length of the off-axis parabolic mirror was $f = 100$ mm.

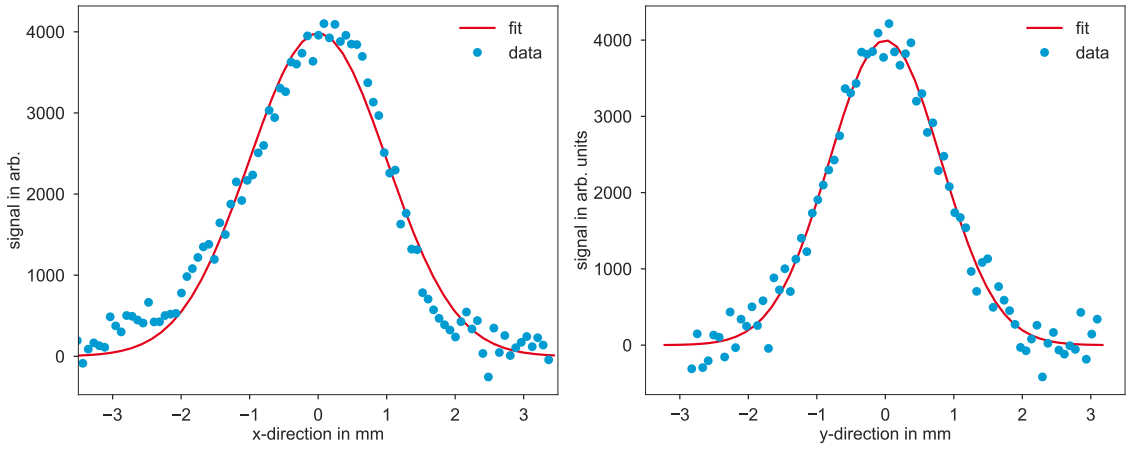

Figure 4.14.: Horizontal (left) and vertical (right) beam size of the THz focus.

pulse was not measured, the resolution in the frequency domain is relatively low. Getting the maximum frequency gives a value of $f_{\mathrm{THz,\,max}} = 0.52\,\mathrm{THz}$. This value is similar to the value we obtained from fitting the electric field with a Gaussian envelope in Figure 4.17. In this case, the frequency of the THz-field from the fit was $f_{\mathrm{THz}} = 0.51\,\mathrm{THz}$. Although the resolution of the spectrum obtained from the FFT is relatively low, the dominant frequency can be estimated from the spectrum.

4.2.4. Gouy Phase Shift

The Gouy phase [38, 39] describes the effect of a Gaussian beam propagating through a focus. It experiences an additional phase shift with respect to a plane wave. This effect has important consequences in optics, it determines for example the resonant frequencies in laser cavities. The Gouy phase results from transverse spatial confinement, which, due to the uncertainty principle, introduces a spread in transverse momenta. This leads to a shift in the expectation value of the axial propagation constant, which is just the Gouy phase. In the Rayleigh range from $-z_R$ and z_R the Gouy phase changes from $\pi/4$ to $-\pi/4$.

The Gouy phase shift is given by:

$$\phi_G(z) = -\arctan\left(\frac{z}{z_R}\right), \tag{4.1}$$

where z_R is the Rayleigh range of the beam and the propagation direction of the beam is along the z-direction with the position of the beam waist at $z = 0$.

Using the EO-sampling technique, it is possible to measure the Gouy phase through the focal region of the THz beam. The THz electric field changes with the Gouy phase and is given by:

$$E(t) = A\exp\left(-\frac{(t-t_0)^2}{\sigma^2}\right)\cos(\omega_0\cdot(t-t_0)) + \phi_G), \tag{4.2}$$

where A, σ are the amplitude and the pulse width and t_0 and ω_0 are the temporal offset and the angular frequency of the THz field.

The electric field changes throughout the focal region of the THz beam, due to the change of $\phi_G(z)$ along the propagation direction. It was measured by mounting the ZnTe crystal on a translation stage and measuring the electric field through EOS at every position. The curves obtained at different positions are shown in Figure 4.17.

To get the real amplitude of the electric field Equation (2.2) was used to calculate the field strength from the measured voltage change. The electric field changes before and after the focus position. The electric field was fitted using Equation (4.2) to obtain the phase at every position. The phase at every position was then fitted with Equation (4.1) to obtain the Rayleigh range. The measurement was performed several times and the results are

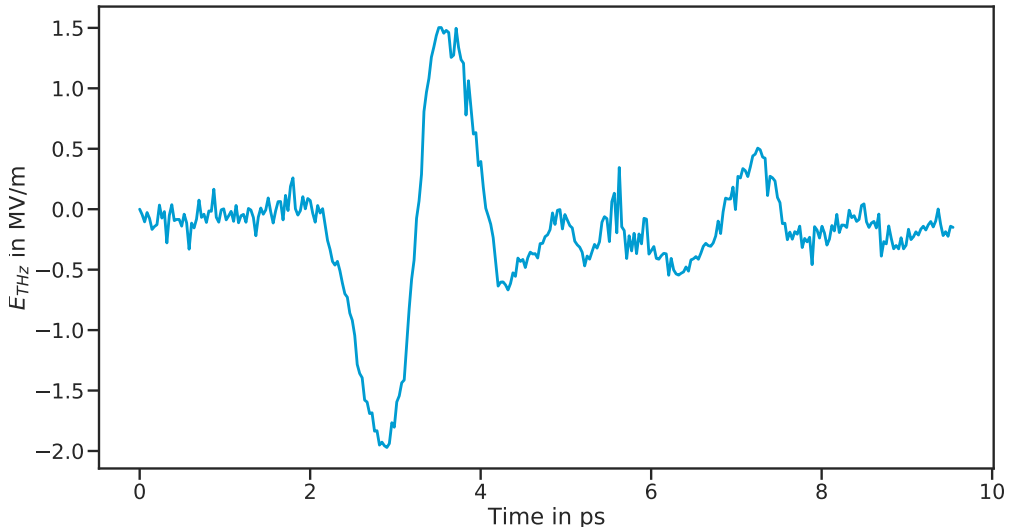

Figure 4.15.: Electric field of the THz pulse in the time domain measured with EO sampling.

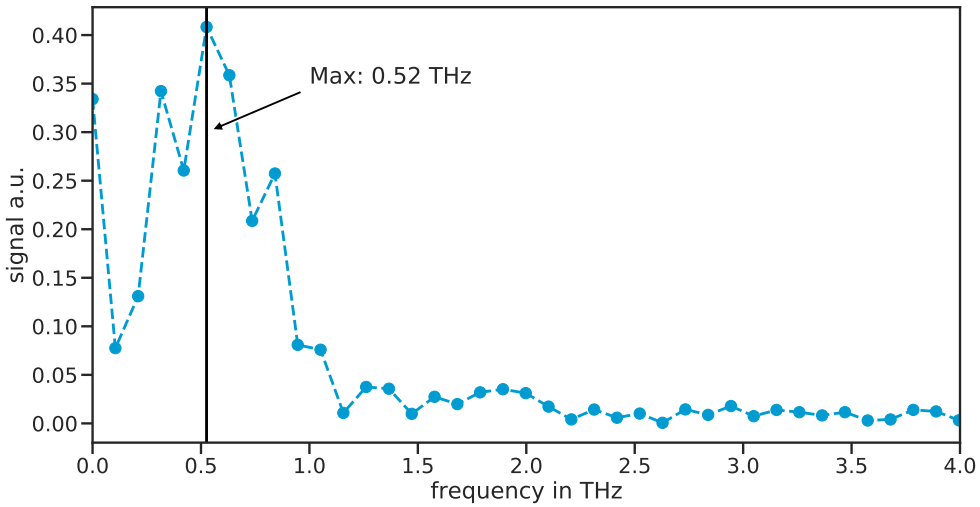

Figure 4.16.: Amplitude spectrum of the THz pulse in the frequency domain, which is obtained through FFT of the THz electric field. The frequency component with the highest amplitude is at 0.52 THz.

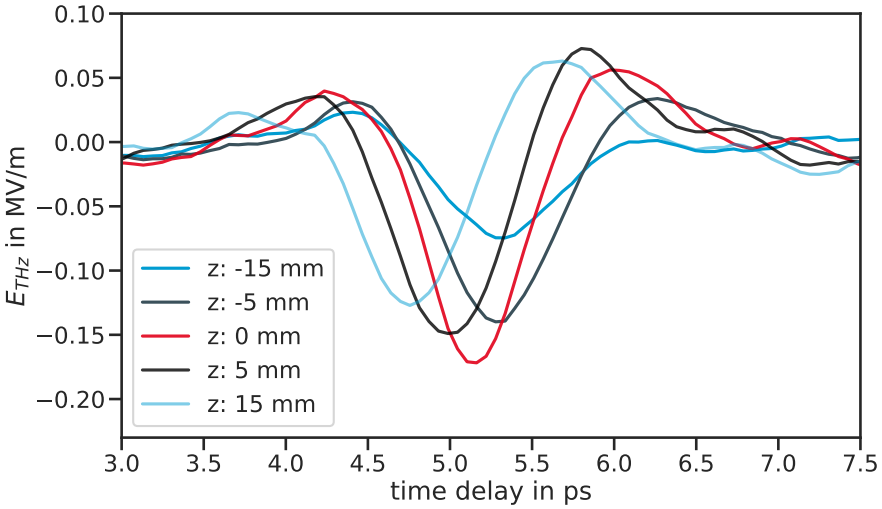

Figure 4.17.: Electric field of the THz beam along several positions along the focal region. The direction of beam propagation is along the z-axis, and z=0 mm is the position of the focus. The phase undergoes a shift of π through the focus.

shown in Figure 4.18. Due to the Gouy phase shift, the streak field shifts along the interaction zone relative to the time of the electron emission (Figure 4.19 (left)). To estimate the influence of the Gouy phase on the measurements, the length of the interaction zone has to be known. In [40] measurements were carried out by moving the gas nozzle transversely and measuring the number of electrons in the TOF. The length was determined to be $d_{\text{Gas}} = 0.75\,\text{mm}$. The phase shift along the interaction zone can be calculated by:

$$\tau_{\text{Gouy}} = \frac{d_{\text{Gas}} \mathrm{d}\phi}{2\pi f_{\text{THz}}}, \tag{4.3}$$

where $\mathrm{d}\phi$ is the change of the Gouy phase, d_{Gas} the length of the interaction zone and f_{THz} is the THz frequency. The change of the Gouy phase $\mathrm{d}\phi$ along the interaction zone is assumed to be approximately linear. The value of $\mathrm{d}\phi$ can be determined by fitting a straight line to the measured data points around $z = 0$ (Figure 4.19 (right)). The slope of the curve is determined to be $\mathrm{d}\phi = (0.134 \pm 0.05)\,\text{rad/mm}$. Using the THz frequency $f_{\text{THz}} = (0.54 \pm 0.26)$ THz, the time shift is $\tau_{\text{Gouy}} = (30 \pm 14)$ fs.

To calculate the beam size from the measurements, the Rayleigh range and the wavelength of the THz are needed. The THz wavelength was calculated from the measured frequency f_{THz}. The beam waist w_0 can be calculated:

$$w_0 = \sqrt{\frac{z_R \lambda_{\text{THz}}}{\pi}},$$

and the results are shown in Table 4.2. The beam waist size is approximately $w_0 = (1.3 \pm 0.3)$ mm. This is larger than the results from the Pyrocam THz camera, since the Pyrocam is not so sensitive to the tails of the beam intensity distribution and therefore the beam radius seems smaller. For the Gouy measurements, a monochromatic beam with

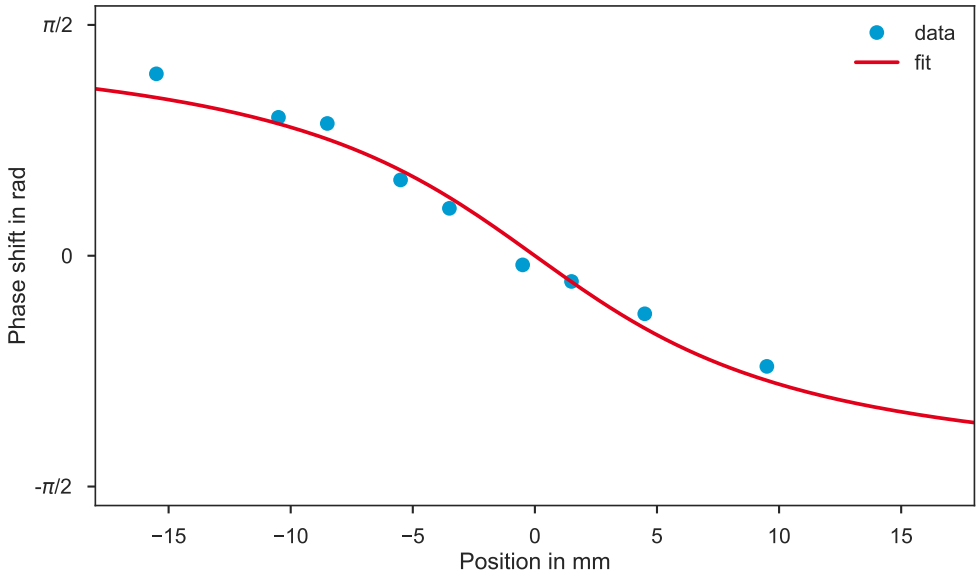

Figure 4.18.: Gouy phase shift through the focus of the THz beam. The phase changes from $\pi/2$ to $-\pi/2$, before and after the focus. In blue are the data points for the measurement of the phase through the focus and the Gouy phase fit is shown in red.

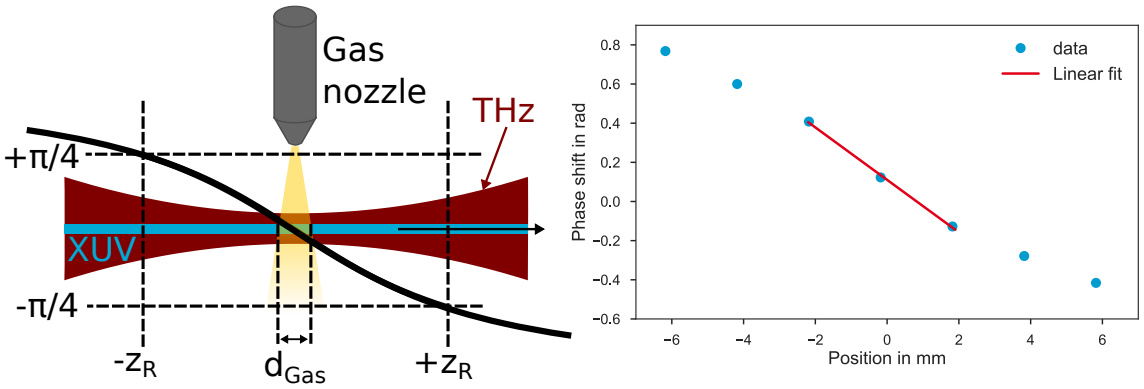

Figure 4.19.: Left: Gouy phase shift along the propagation direction. From $-z_R$ to $+z_R$ the Gouy phase changes from $+\pi/4$ to $-\pi/4$. The phase difference along the interaction zone d_{Gas} has influence on the streaking measurements. Right: Linear fit through the interaction zone to determine the change of the Gouy phase along the propagation direction.

Table 4.2.: Rayleigh range and beam waist calculated from the Gouy phase scans

	Rayleigh range in mm	beam waist in mm
1	10.4 ± 1.1	1.4 ± 0.3
2	8.4 ± 0.7	1.2 ± 0.3
3	7.6 ± 1.2	1.2 ± 0.3
Mean	$\mathbf{8.8 \pm 0.6}$	$\mathbf{1.3 \pm 0.3}$

a Gaussian transverse distribution was assumed [39]. The THz pulses used for the measurements are broadband pulses with a wide frequency range, as shown in Figure 4.16. The assumption of a monochromatic beam is not accurate in this case. To compensate for theses deviations from an idealistic monochromatic beam, the fluctuations of the THz frequency were estimated from the measurements shown in Figure 4.16 and the wavelength used for the calculations is $\lambda_{\mathrm{THz}} = (0.6 \pm 0.3)$ mm.

5. Experimental Results with THz Streaking

In this chapter, the results from the experimental measurements of the Auger electron lifetimes of xenon and iodomethane are presented. To extract the lifetimes from the measured timeshift, the XUV pulse length needs to be known. In Section 5.2, a method to measure the XUV pulse length from the streaking curves is described and the measured values of the XUV pulse length are presented. Since the electron emission time is encoded in the streak curve phase, by measuring the signal of the emitted electrons, the emission times of the Auger electrons relative to the photoelectrons can be estimated. Measuring known Auger decays is a good method to test the setup. In this thesis, the NOO Auger electrons of xenon will be used to benchmark the experimental setup. This process helps to show that the temporal resolution to measure ICD electron lifetimes is achieved. In Section 5.3, the results from the measurements of the Auger lifetimes are presented for different target gases. From these benchmark measurements the temporal resolution for ICD lifetime measurements can be estimated, see Section 5.4.

5.1. Energy Calibration

The TOFs measure the flight time of the electrons. In order to get the energy of the electrons, the calibration of the TOFs has to be known. This can be done either by building a model of the TOFs and simulating the electron traces (with the software SimIon) or by calibration measurements with a known spectrum. Then the calibration parameters can be determined by a fit. In general, the dependence between the electron energies and the measured flight-time is:

$$E_{\text{kin}} = \frac{C^2}{(t - t_0)^2} - U_{\text{ret}} \,, \tag{5.1}$$

where C is a calibration parameter, t_0 is a time shift and U_{ret} corresponds to the retardation voltage. A retardation voltage can be applied to the TOFs to shift the electron energies. For example faster electrons can be slowed down to shift their flight-times to a range which has a better resolution.

Since the time to energy calibration is not a linear relationship, the signal height has to be adapted, too. The area under the peak should be the same, so the new signal height is

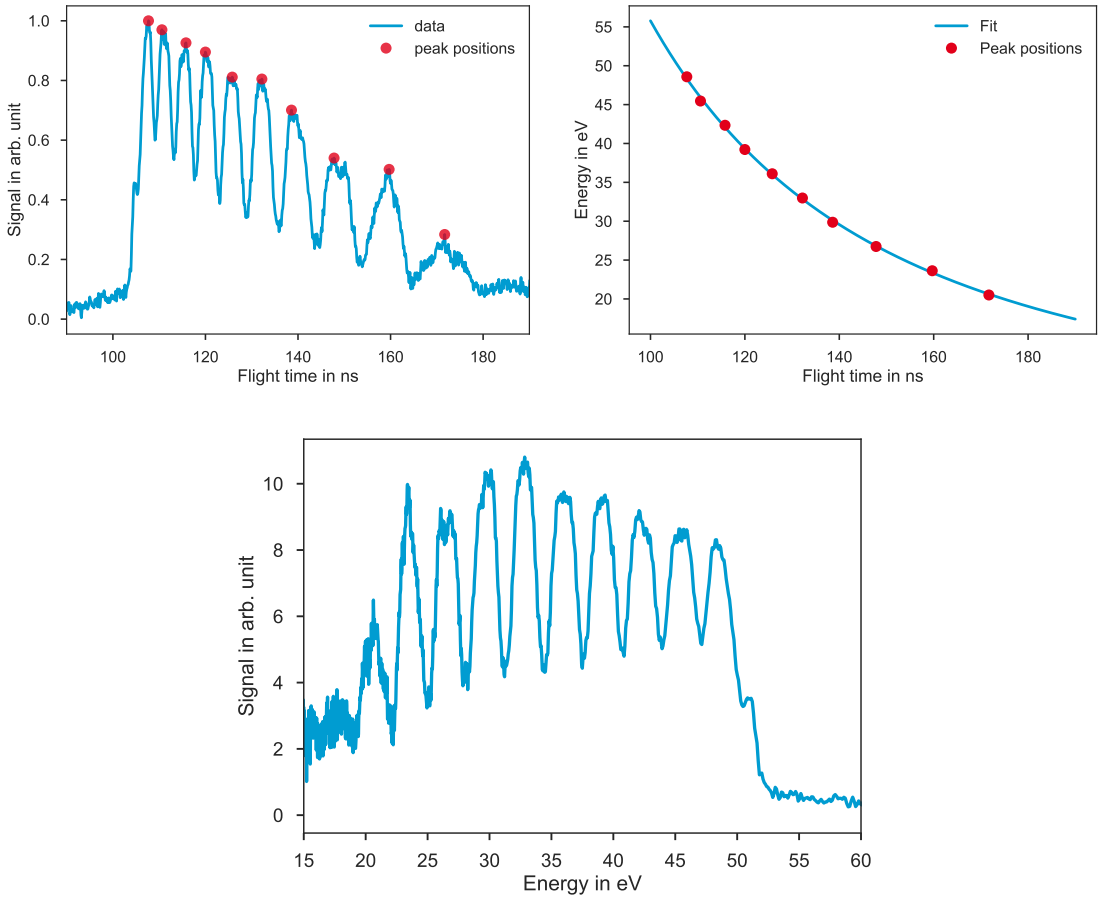

Figure 5.1.: a) Measured spectrum with neon as the target gas and using an aluminum filter. The photopeaks originate from ionization of the 2p orbital. b) The peak positions in flight time and the peak energies calculated are calibrated from the XUV harmonic energies minus the electron binding energy of 21.6 eV. A fit using Equation (5.1) gives the calibration parameters to calculate the energy from the flight-times. c) Measured neon spectrum with corrected signal heights over electron energies.

given by:

$$h_{\text{corr}} = \frac{h_{\text{Signal}}}{2} \frac{C}{(E_{\text{kin}} + U_{\text{ret}})^{3/2}} , \tag{5.2}$$

where h_{Signal} is the measured signal height.

For the calibration measurements, neon was used as the target gas. The spectrum has known photoelectron lines and no overlapping peaks in our measurement range. A reference spectrum measured with neon and an aluminum filter to select the XUV radiation of the harmonic orders 11 to 47 is shown in Figure 5.1 a). The photon energies of the harmonics, which are transmitted through the aluminum filter, are known. Using the binding energy of the neon 2p electron ($I_p = 21.6\,\text{eV}$), the expected electron energies can be calculated. In neon, the electrons are ionized mainly from the 2p orbital, since the partial cross-section for the 2p orbital is higher within this photon energy region [41]. Extracting the peak positions from the measured spectrum gives the flight-times for the electrons. Fitting the flight-times using the expected energies and Equation (5.1) the calibration parameters can be calculated. An exemplary fit is shown in Figure 5.1 and the resulting spectrum over the electron energies is shown. From this plot, it can be seen that the photoelectron peaks originate from the harmonics of the XUV radiation, and the peaks are spaced equally with a step size twice the energy of the fundamental radiation.

5.2. Measurement of the XUV Pulse Duration

Since the measured time shift between Auger electrons and photoelectrons is a convolution of the Auger lifetime and the XUV pulse duration, the XUV pulses length has to be known. THz streaking can also be used to characterize the XUV pulse, so measurements were performed to determine the pulse length of the XUV. As described in Section 2.4.3, some assumptions about the XUV pulse have to be made in order to determine the pulse length. It is assumed that the XUV pulse has a linear chirp and a Gaussian spectrum. Then the XUV pulse length can be determined from the measured streaking curves. To determine the XUV pulse length, the electron spectra have to be measured with and without the THz field. From the measurement with the THz field, the initial widths $\sigma_{\text{no THz}}$ of the Auger electron and photoelectron peaks can be determined. The spectra with the THz field should be recorded at the zero-crossing of the vector potential of the THz field. There the net change due to the THz field is approximately zero (Figure 5.2), so the center position of the electron peaks is not shifted. Furthermore, around the zero-crossing, the change of the vector potential is linear (see vector potential at position 2), with a constant streaking speed s. For a XUV pulse with a pule length of zero (which is impossible), the widths of the electron peaks would not change. But for longer XUV pulse lengths, the THz field changes the kinetic energy of the electrons generated from the ionization with the XUV pulse. This change of the kinetic energy of the electrons is reflected in the width

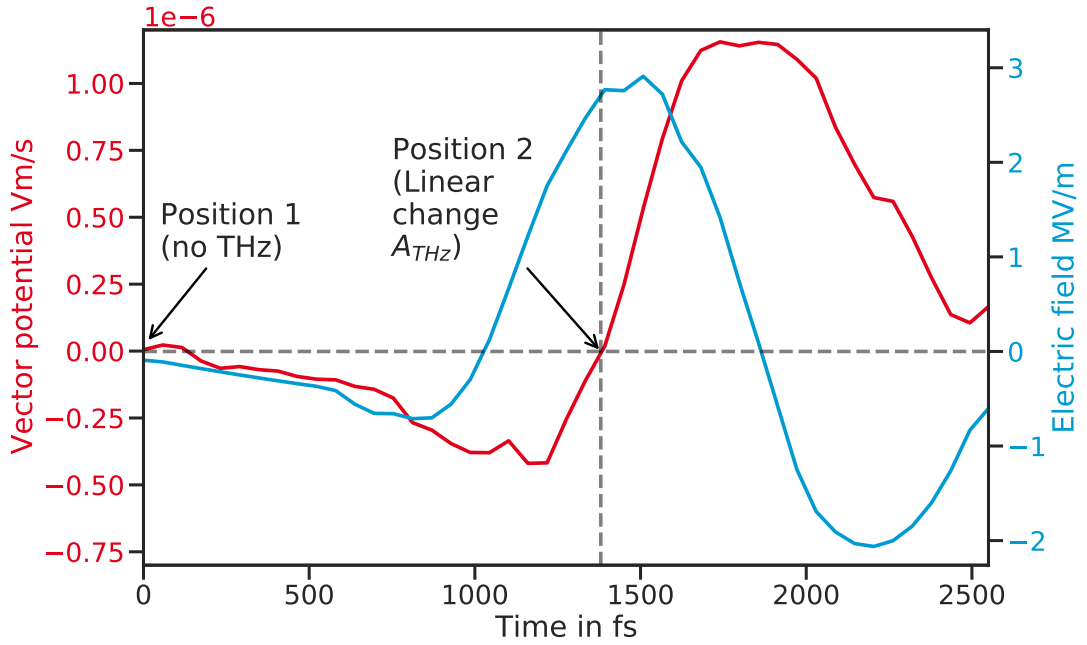

Figure 5.2.: Vector potential and electric field for measurement of XUV pulse length. Measurements were taken at position 1, where the THz field is zero and at a point with high electric field and a net shift of zero due to the vector potential. The change of vector potential is approximately linear in this region.

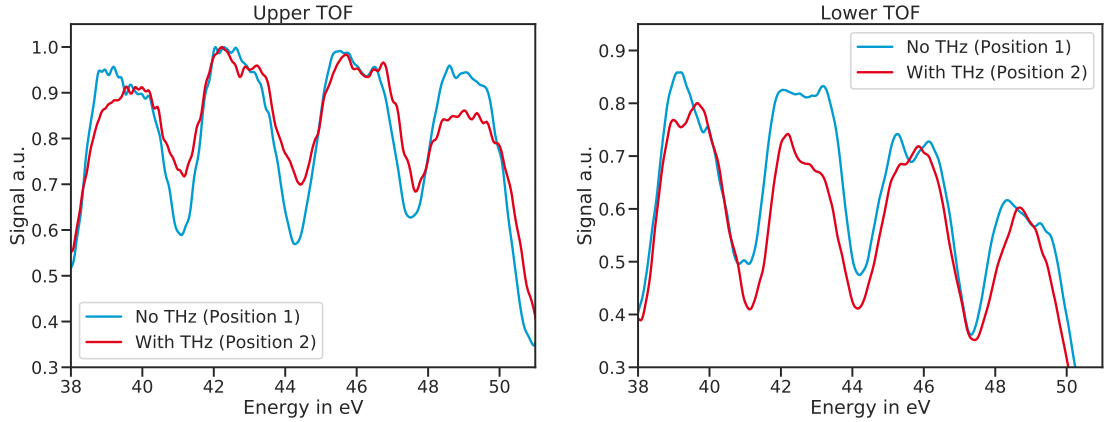

Figure 5.3.: Widening of the spectrum through THz streaking. For one TOF (left side) the peaks become wider, whereas with the other TOF (right side) narrower peaks are measured.

Table 5.1.: Measurement of the XUV pulse length from the peak widths of the spectrum with and without THz.

$\sigma_{\text{No THz, +}}$	$\sigma_{\text{streak +}}$ in eV	$\sigma_{\text{No THz, -}}$ in eV	$\sigma_{\text{streak -}}$ in eV	s in eV/fs	$\sigma_{\mathbf{XUV}}$ in fs	c eV/fs
0.97 ± 0.01	1.09 ± 0.02	0.97 ± 0.01	0.95 ± 0.01	0.008 ± 0.001	$\mathbf{44 \pm 8}$	2.5 ± 1.1
0.98 ± 0.01	1.04 ± 0.01	0.91 ± 0.01	0.89 ± 0.01	0.008 ± 0.001	$\mathbf{29 \pm 7}$	3.2 ± 1.8

of the electron peaks. Measuring the change of the electron peak widths gives the XUV pulse length.

However, it was assumed that the XUV pulse length has a chirp, so the electrons generated at the head of the XUV pulse have a different energy compared to electrons generated at the tail of the XUV pulse. Therefore it is not sufficient to measure the electron spectra with only one TOF. Instead, two TOFs that are placed in opposite directions are required. For one TOF the spectral width of the peaks increases $\sigma_{\text{streak+}}$ and for the TOF in the opposite direction the spectral width decreases $\sigma_{\text{streak-}}$, see Figure 5.3. The pulse length of the XUV pulse can then be calculated by:

$$\tau_{\text{XUV}} = \sqrt{\frac{(\sigma^2_{\text{streak +}} - \sigma^2_{\text{no THz}}) + (\sigma^2_{\text{streak -}} - \sigma^2_{\text{no THz}})}{2s^2}}, \tag{5.3}$$

where $\sigma_{\text{streak} \pm}$ are the widths measured with the two TOFs in opposite direction and s is the approximately constant streaking speed at position 2. After the XUV pulse length is measured, the chirp of the XUV pulse can be determined:

$$c = \frac{(\sigma^2_{\text{streak +}} - \sigma_{\text{no THz}}) - (\sigma^2_{\text{streak -}} - \sigma_{\text{no THz}})}{8s\tau^2_{\text{XUV}}}. \tag{5.4}$$

Table 5.1 presents two measurements of the reconstructed XUV pulse length.

The fundamental pulse of the laser before the high harmonic generation has a pulse duration of around 27 fs (FWHM). Assuming that the XUV pulse has a similar pulse duration due to the generation process, a pulse length of 12 fs rms is expected. The measured results are much larger with (44 ± 8) fs and (29 ± 7) fs. This might come from the fact that the streaking speed $s = 0.01\,\text{eV}\,\text{fs}^{-1}$ is relatively low and therefore the change in the measured peak widths with and without THz radiation is very small (only 0.02 eV - 0.12 eV change). The measured pulse length also has to be corrected for the Gouy phase shift along the interaction region. Due to this phase shift, the XUV pulse length is a convolution of the Gouy phase shift with the measured pulse length:

$$\tau_{XUV} = \sqrt{(\tau^2_{\text{XUV,meas}} - \tau^2_{\text{Gouy}})}\,.$$

From the measured values, the XUV pulse length corrected by the Gouy phase shift is $\sigma_{\mathrm{XUV}} = (33 \pm 17)$ fs for a measured length of $\sigma_{XUV,meas} = (44 \pm 8)$ fs. For a measured length of $\sigma_{XUV,meas} = (29 \pm 7)$ the deconvolution could not be calculated, since $\sigma_{XUV,meas} < \tau_{Gouy}$. These measured deviations from the expected value were also found in many other experiments [42, 37]. In these measurements, significantly longer XUV pulse lengths were measured.

5.3. Measurement of the Auger Electron Lifetimes

Now the Auger electron lifetimes should be determined from measurements of the time shift between photoelectrons and Auger electrons. Photoelectrons are assumed to be emitted instantaneously, even though previous experiments measured small shifts in the attosecond range between photoelectrons emitted from different orbitals [43]. However, these small delays will not play a role in the experiments performed for this thesis, as we are interested in measuring lifetimes in the range of several femtoseconds. Therefore it can be assumed that the photoelectron emission rate represents the temporal profile of the ionizing light pulse. The profile of the photoelectrons is then given by a Gaussian pulse (like the ionizing XUV pulse):

$$I_{PE}(t) = \exp(-t^2/2\sigma^2)\,,$$

where σ is the rms pulse duration of the ionizing XUV pulse. The emission of the Auger electrons can be described by a convolution of the temporal distribution of the ionization of the atoms and the evolution of the Auger decay process, which is given by:

$$A_{\mathrm{decay}}(t) = \begin{cases} A\exp(-(t-t_0)/\tau_{\mathrm{Auger}}) & \text{for } t \geq t_0 \\ 0 & \text{for } t \leq t_0 \end{cases}$$

where t_0 is the delayed starting time of the Auger decay process, A is the amplitude and τ_{Auger} is the decay lifetime of the Auger process. The temporal profile of the Auger emission process is:

$$\begin{aligned} I_{AE}(t) &= (I_{PE} * A_{\mathrm{decay}})(t) \\ &= \int_{-\infty}^{\infty} I_{PE}(t-t')A_{\mathrm{decay}}(t')\,\mathrm{d}t' \\ &= A\frac{\sqrt{2\pi}\sigma}{2}\exp\left[\frac{1}{\tau_{\mathrm{Auger}}}\left(t_0 - t + \frac{\sigma^2}{2\tau_{\mathrm{Auger}}}\right)\cdot\left[1-\mathrm{erf}\left(\frac{1}{\sigma\sqrt{2}}\left(t_0 - t + \frac{\sigma^2}{\tau_{\mathrm{Auger}}}\right)\right)\right]\right]. \end{aligned}$$

The Auger emission rate is plotted in Figure 5.4 for a XUV pulse length $\sigma = 12.7$ fs, a start time $t_0 = 0$ and an Auger lifetime $\tau_{\mathrm{Auger}} = 6$ fs, which is the reference lifetime of the

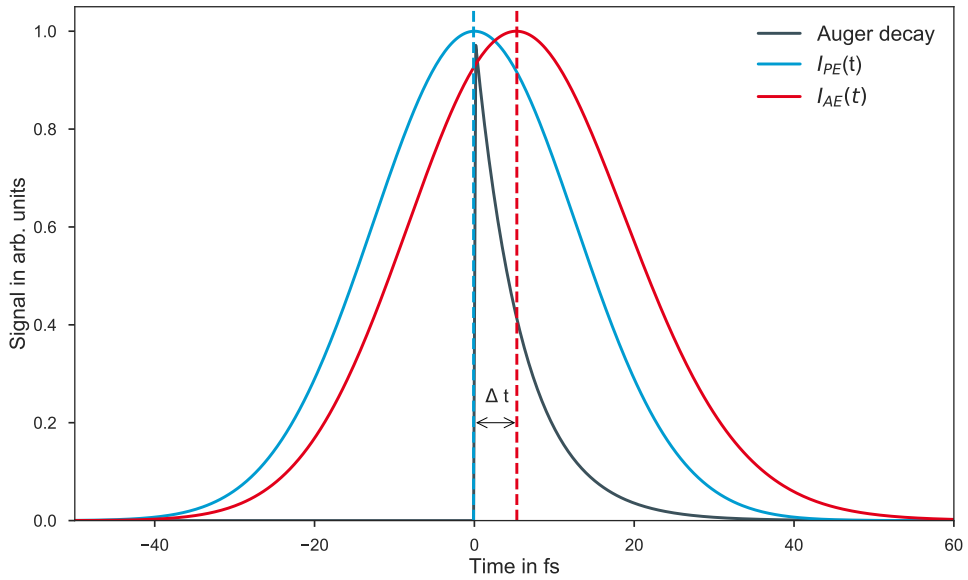

Figure 5.4.: Emission rates of photo and Auger electrons, where we assumed that the Auger decay had $\sigma_{\mathrm{XUV}} = 12.7\,\mathrm{fs}$ ($t_0 = 0$), and the Auger lifetime τ_{Auger} =6 fs was assumed. A shift $\Delta t \approx 5.3\,\mathrm{fs}$ between the photoelectron and Auger electron curves can be seen, due to a non vanishing Auger lifetime. The shift decreases for shorter lifetimes τ_{Auger}.

Auger process NOO in Xe, which is a well-studied process [44, 45]. With these values, the expected time shift between the maxima of the photoelectron and Auger electron emission curves is $\Delta t = 5.3\,\mathrm{fs}$. Measuring this known Auger lifetime allows us to show the ability and accuracy of our experimental setup. If the XUV pulse length is longer than the Auger lifetime, the Auger emission rate is also Gaussian shaped. For longer XUV pulse durations, the time shift becomes larger, but is less dependent on the Auger lifetime, as seen from Figure 5.5. The shift of the maxima of between the Auger electron and photoelectron curves means that they are generated and emitted at another phase of the THz field. Thus, by measuring the emission rate for different time delays between the ionizing pulse and the THz pulse, the time shift can be measured.

5.3.1. Measurements at FLASH

To show the capability of our setup, a benchmark experiment measuring the NOO-Auger electron lifetimes in xenon was performed. Using a known lifetime of a well-studied Auger decay can help to prove the ability and test the accuracy of the setup. For Auger electrons of a pure one-atomic system, the lifetime can be inferred from the spectral widths of the electron spectra. For xenon 4d electrons, the Auger lifetimes are about $\tau_{4\mathrm{d}_{3/2}}$ = (6.3 ± 0.2) fs and $\tau_{4d_{5/2}}$ = (5.9 ± 0.2) fs [45, 44]. For more complex systems like molecules, it is no longer possible to use the spectral width to measure the lifetime of the

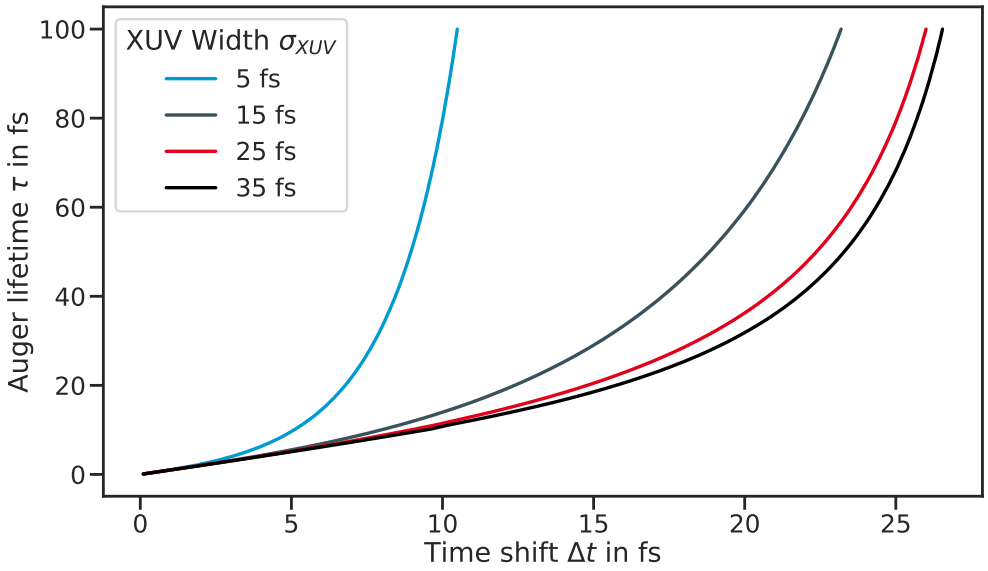

Figure 5.5.: Dependence of the Auger lifetime on the time shift Δt between the maxima of the measured photoelectron and Auger electron signal for different durations of the ionizing XUV pulses. For short pulse lengths, the Auger lifetime changes drastically with the measured time shift. For longer pulse durations, the dependence is less sensitive.

Auger electrons. For these systems, a time-domain approach is useful. Using the streaking technique, the electron emission time is encoded in the phase of the streaking curve, and the Auger lifetime can be calculated by measuring a phase shift between streaked electron curves for photo and Auger electrons.

An experiment that used a known Auger decay as a benchmark to test the experimental setup was performed at FLASH [1]. In this experiment, krypton 3d Auger electrons were used to test the setup. The experimental setup was similar to ours. The target system was ionized using soft x-ray pulses at 200 eV, which were superimposed with the THz radiation for streaking the electrons. In [1], both the x-ray pulses and the THz pulses were generated from a free-electron laser. Therefore they have very different pulse properties compared to the laser-based setup used during this thesis. The impact of these properties on the measurements will be discussed in Section 5.4.

In Figure 5.6, electron spectra of krypton recorded for different delays between the ionizing soft x-ray pulse and the THz are shown. The MNN-Auger electrons have energies around 40 eV, and the initial energy of the 3d photoelectrons without the THz is 107.5 eV. By fitting Gaussian curves to the peaks, their centers can be determined. By plotting these centers for one of the Auger electrons and the photoelectron curve and then fitting a sinusoidal, the phase difference between the curves can be determined. The phase shift between the Auger and photoelectron curves reflects the averaged delayed emission of the Auger electrons. This timeshift can be used to determine the corresponding lifetime

of the Auger electrons. The method was successfully used to measure an Auger lifetime of (8 ± 5) fs for the krypton MNN-Auger electrons, whose lifetime is known to be $\tau_{AE} = 7.9^{+1}_{-0.9}$ fs.

5.3.2. Xenon Spectrum

The measurements of the Auger lifetimes which are used to test the experimental setup were performed with xenon. A Zr filter was used to select the harmonics for these measurements. The selected photon energies ranged from 65 eV to 105 eV. A photon energy higher than the 4*d* threshold of xenon ($4d_{3/2}$ = 67.5 eV and $4d_{5/2}$ = 69.5 eV) is needed to create Auger electrons. Photoelectrons originate from the 4d orbital, can be seen in Figure 5.7. Above 70 eV and up to the 3d electron binding energy of xenon, the 4d partial cross section is much higher than for the 5p and 5s orbitals. Therefore the photoelectrons originating from the 4d orbital result in more prominent peaks in the spectrum and the peaks from the 5p and 5s orbitals can be neglected. The measured electron spectrum consists of $N_{4,5}OO$ Auger electrons mainly in the energy range between 30 eV to 36 eV. A series of xenon photo- and Auger electron spectra which were taken for different delay times between the THz and XUV pulses is shown in Figure 5.8. The red lines show the prominent features of the Auger lines and the weaker and broader white lines at around 24 eV and 27 eV are photoelectron lines.

The orbitals are also termed O and N orbitals, so the Auger electrons resulting from a 4d vacancy are labeled NOO-Auger electrons. The Auger NOO-electrons are displayed in Figure 5.9. The data for Figure 5.9 was taken from [46]. In the range between 28 eV and 38 eV there are nine Auger peaks, see Table 5.2. For pure atomic Auger electrons the spectral widths of the Auger peaks corresponds to their lifetime. For Auger electrons, the spectral widths was measured to be 107 meV and 114 meV [45] for the NOO Auger electrons generated by photoionisation of the 4d orbitals in xenon. Due to the limited resolution of the TOFs not all Auger peaks can be resolved. As seen in Figure 5.10, only three of the peaks are resolved and two of them are still double peaks. The Auger electrons with a weaker signal can not be resolved as single peaks.

A simulation of the xenon 4d photopeaks was calculated using the harmonic spectrum measured with the Zr filter (Figure 5.10 (left)). The measured spectrum, shown in Figure 5.10 (right), contains the 4d photopeaks and the xenon $N_{4,5}OO$ Auger peaks. The XUV radiation up to the harmonic order of 69 was used to calculate the energies of the photopeaks, and the height of the photopeaks was scaled according to the measured spectra. The widths of the Auger peaks are set from the spectral resolution from the TOFs. The Auger electrons overlap with some of the photopeaks. To get better results for our analysis, we select only a few of the peaks for further fitting. The part of the spectrum which is selected for the fit is shown in the red rectangle in Figure 5.10 (right).

In this part of the spectrum, two peaks originate only from photoelectrons and three of the peaks originate mainly from Auger electrons with a small background of photoelectrons. This background can be neglected in the analysis since the shape and the widths

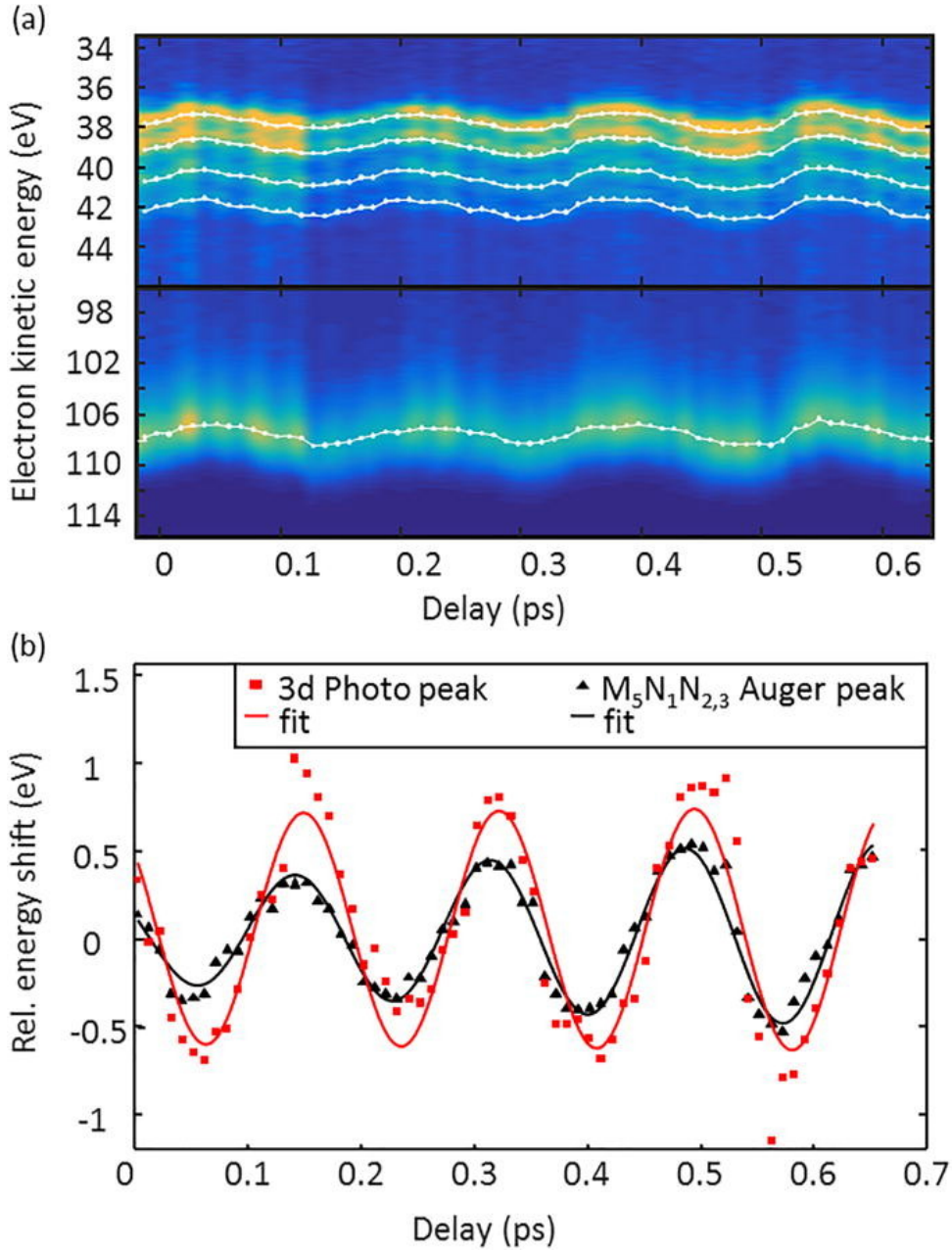

Figure 5.6.: a) Krypton spectra taken with 200 eV soft x-ray pulses for different delays between the THz and x-ray pulses. Gaussian curves were fitted to the peaks to obtain the center energies of each peak. b) A sinusoidal curve was fitted to the energy shift of the photo- and Auger electron lines (taken from [1]).

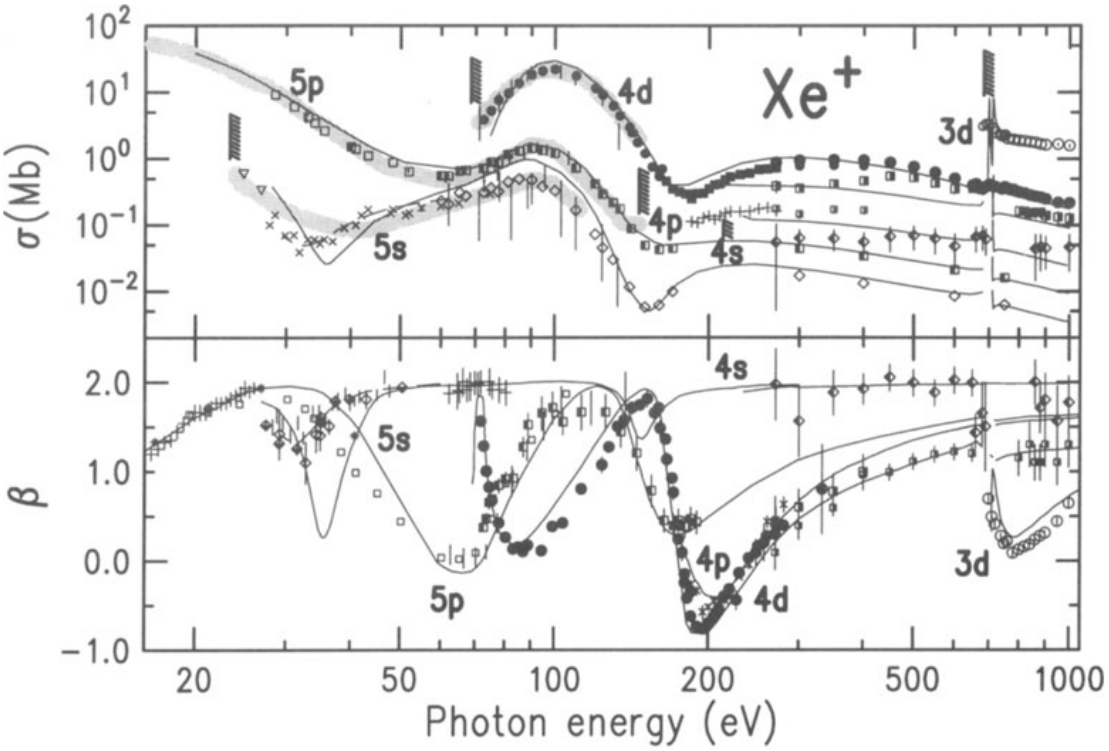

Figure 5.7.: The partial cross section and angular distribution parameter β for the 5p, 5s, 4d, 4p as a function of the photon energy for xenon. For photon energies above 70 eV and below the 3d electron binding energies of about 680 eV, the 4d partial cross section is the dominant term [41].

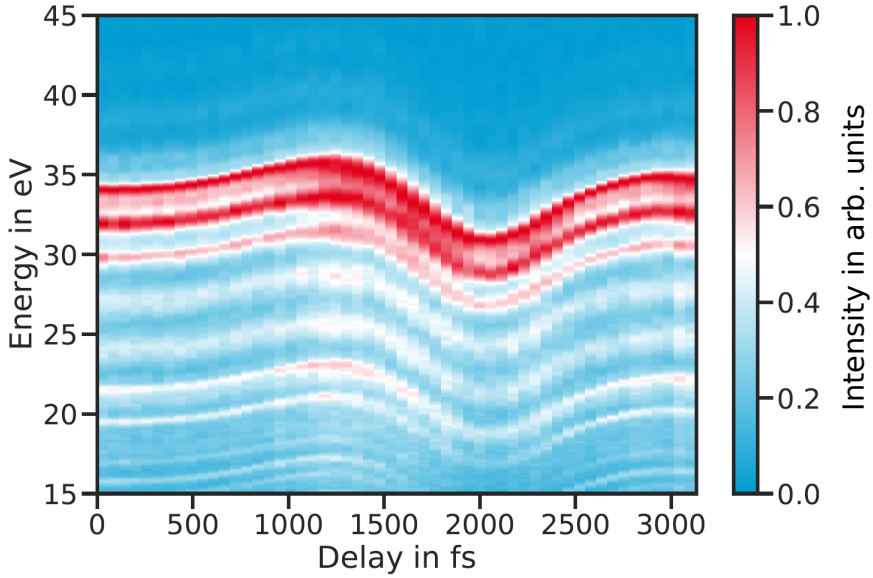

Figure 5.8.: Series of xenon photo- and Auger electron spectra taken for different delay times between the THz and the XUV pulses.

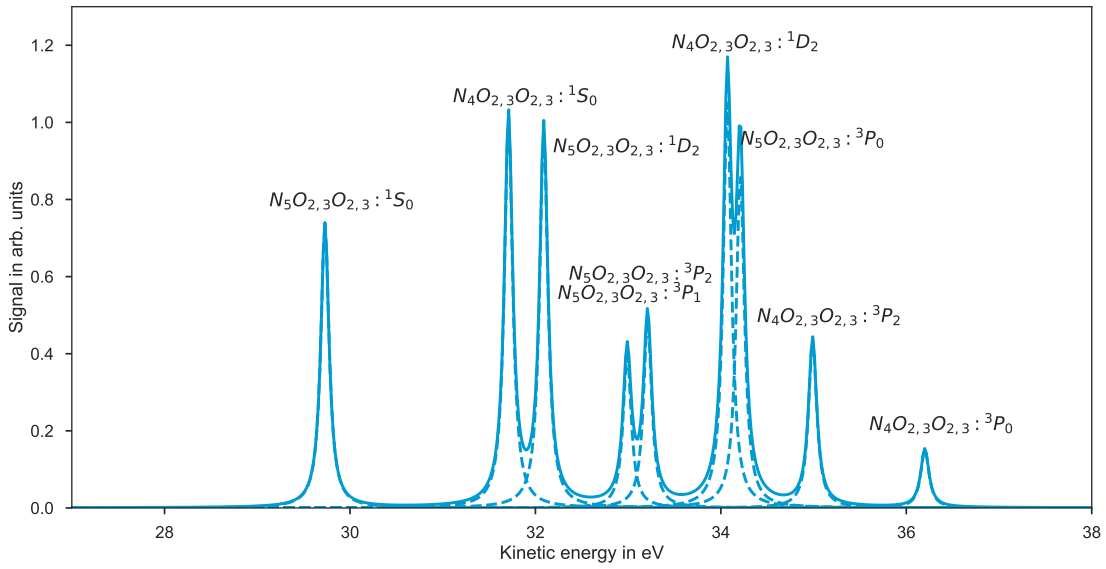

Figure 5.9.: Xenon $N_{4,5}OO$ Auger spectrum, only the kinetic energy range around 30 eV to 35 eV is shown, since theses lines are observed in the experimental spectra. The values are taken from [46].

Table 5.2.: Auger electron peaks, values taken from [46].

Line	Kinetic energy in eV	Assignment
1	36.20	$N_4O_{2,3}O_{2,3}:{}^3P_0$
2	34.99	$N_4O_{2,3}O_{2,3}:{}^3P_2$
3	34.21	$N_5O_{2,3}O_{2,3}:{}^3P_0$
4	34.07	$N_4O_{2,3}O_{2,3}:{}^1D_2$
5	33.21	$N_5O_{2,3}O_{2,3}:{}^3P_2$
6	32.99	$N_5O_{2,3}O_{2,3}:{}^3P_1$
7	32.09	$N_5O_{2,3}O_{2,3}:{}^1D_2$
8	31.71	$N_4O_{2,3}O_{2,3}:{}^1S_0$
9	29.73	$N_5O_{2,3}O_{2,3}:{}^1S_0$

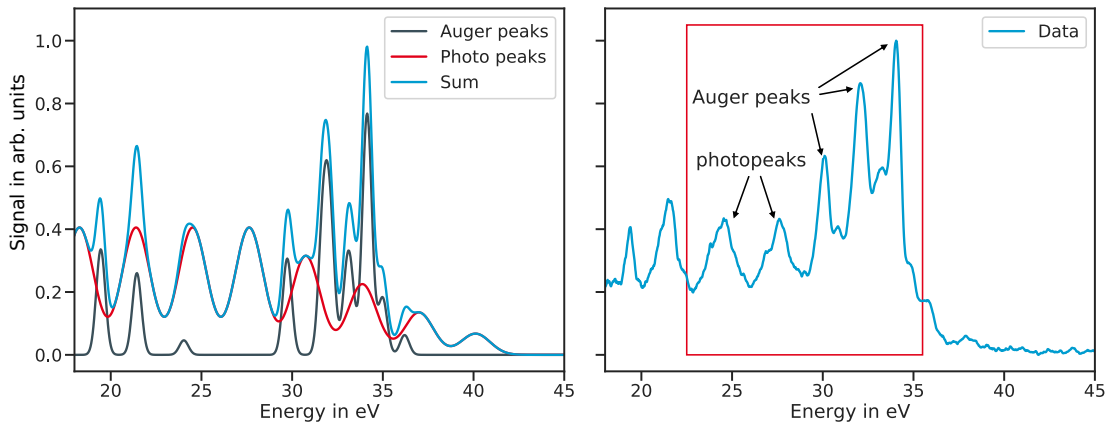

Figure 5.10.: Left: A simulation of the Auger (gray) and photopeaks (red) contribution to the total measured spectrum. The 4d photoelectrons originate from XUV radiation up to the 69th order. Right: A measured spectrum with xenon. The red rectangle shows the part of the spectrum which will be used for the fitting with two photopeaks and three peaks which originate mainly from the Auger electrons (shape and center of the peaks are dominated by Auger electrons).

of the peaks are dominated by the Auger electrons. Mainly the amplitude is affected due to the additional signal background from the photoelectrons. Since only the center and widths are important for the later analysis, this does not affect the results. Only the Auger peak at around 30 eV is a single peak coming from the $N_4O_{2,3}O_{2,3}$:$^1S_0$ process, the other clearly visible peaks at around 32 eV and 34 eVare double peaks, where the substructure of two peaks can not be resolved by the TOFs.

Several methods to fit the peaks in the selected part of the spectrum were tested. At first, we tried to model the spectrum with all the components, as shown in the simulation in Figure 5.10 (left). The selected part of the spectrum then contains 7 Auger peaks (lines 3 to 9) and four photopeaks. All peaks were modeled as Gaussian peaks and are shown in the left plot of Figure 5.11. Since many of the peaks overlap in the region between 30 eV to 35 eV, some assumptions were made. Neighboring photopeaks have to have a distance of two times the energy of the fundamental (distance between the high harmonics of the XUV pulse). We also set an upper limit for the widths of the peaks and the Auger peaks should be less wide than the photopeaks. Even with these conditions, it was hard to achieve a good fit. Although the difference between the combined model and the measured data was good, the single components of the fit did not match our expected components of the spectrum. Therefore further simplifications were made. All Auger peaks which could not be resolved with the TOFs were modeled as a single peak, thus reducing the amount of Auger peaks from seven to four. We also eliminated the photopeaks above 30 eV. This made the fitting routine much easier and faster. The result for one fit is shown in the right plot of Figure 5.11 (right). The total fit is still in good agreement with the data. We noticed that the fitting routine sometimes had problems

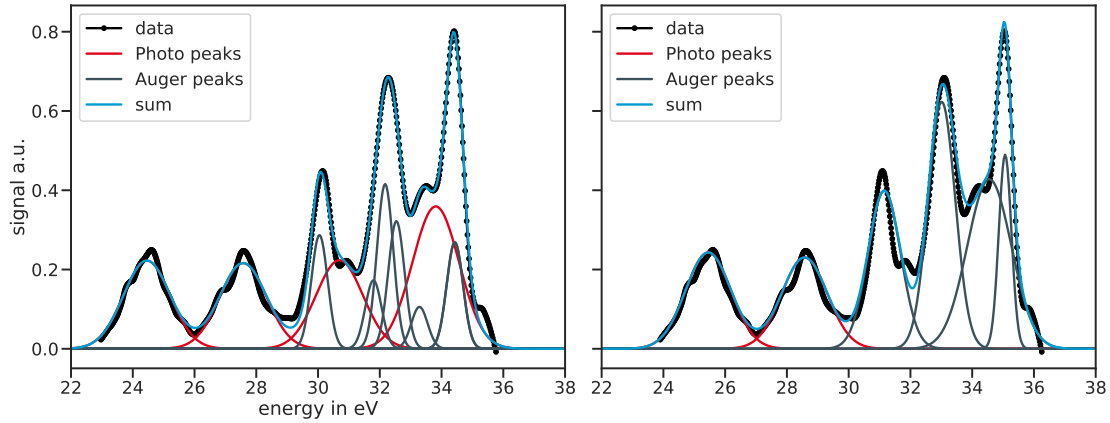

Figure 5.11.: Left: Fitting the spectrum with all components. Four photoelectron peaks and 7 Auger electrons peaks (with Auger electron peaks 3 to 9) were used. Right: Combining all double Auger peaks, which can not be resolved, into single peaks to reduce the amount of fitting parameters and using only two photopeaks in the energy region without an overlap with the Auger peaks.

for the peak which combines lines 5 and 6 since this peak is not very pronounced. Some results for these peaks were not clearly recognizable. They were eliminated from further analysis. Therefore, the fit was reduced to only three Auger peaks and two photopeaks. The results of fitting the selected part of the xenon spectrum to obtain the energy of the photo and Auger peaks is shown in Figure 5.12. Performing this fit for every time delay between the XUV and the THz pulse gives the energy shift for every Auger and photoelectron peak.

5.3.3. Time Shifts

In order to obtain the Auger lifetimes, the time shift between the streaking curves for the photoelectron and the Auger electrons must be determined. The streaking curves follow the behavior of the THz pulse and can be described by a Gaussian envelope:

$$E(t) = A \cdot \exp\left(-\frac{(t-t_0)^2}{\sigma^2}\right) \sin\left(\omega(t-t_0)+\varphi\right),$$

where A is the amplitude of the energy shift, ω is the angular frequency of the THz field, φ the phase and σ the width.

In Figure 5.13 the streaking curves for a xenon 4d photoelectron and an Auger electron line are shown. The Auger energies have higher initial energy, and therefore the energy shift is higher for the Auger energies. A Gaussian envelope is fitted to both curves. The same pulse parameters ω, σ of the THz field are assumed during the fit. Taking the results for each pair of Auger and photoelectrons and analyzing several streaking measurements of xenon, the time shift between Auger- and photoelectrons was determined as:

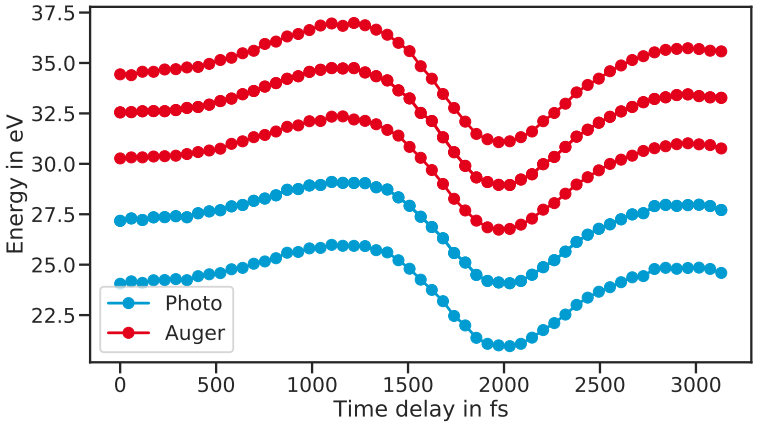

Figure 5.12.: The energy of the peaks over the delay time between the XUV and the THz pulse. A Gaussian fit for the three Auger electron peaks and the two photoelectron peaks was performed for each electron spectrum.

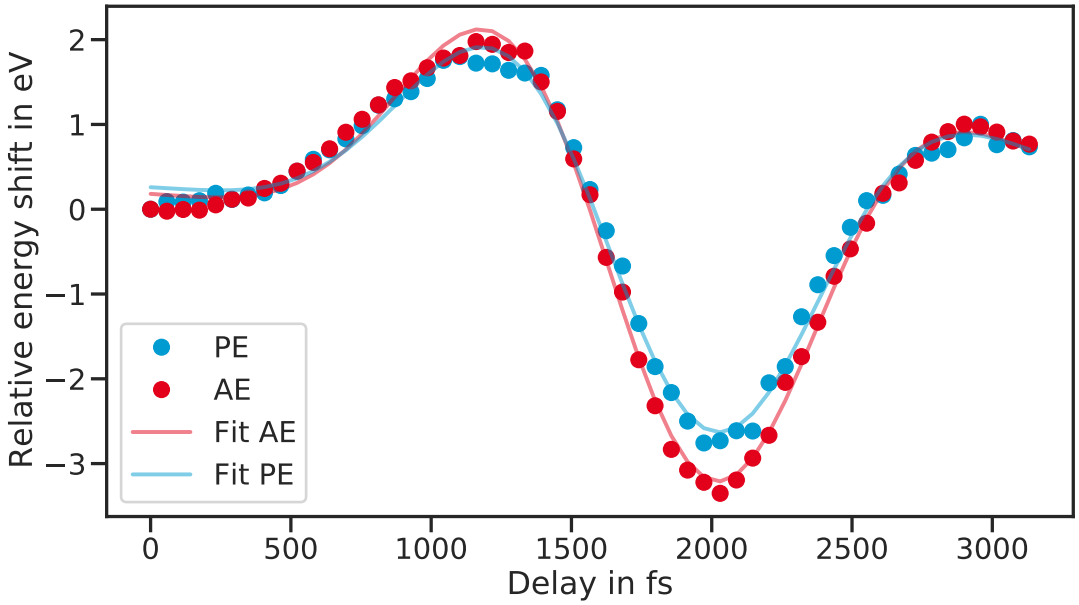

Figure 5.13.: Gaussian envelops are fitted to the energy shift of the photo- and Auger electron peaks of the spectra. Since the expected time shift between the Auger and photoelectrons is only a few femtoseconds, it is hard to see in the plot.

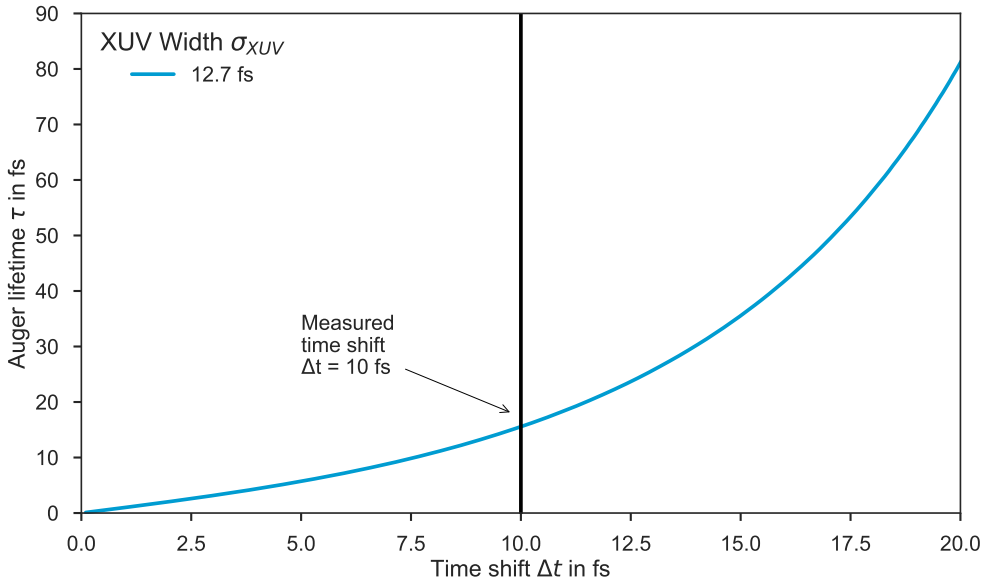

Figure 5.14.: Dependence of the Auger lifetime on the measured time shift for a XUV pulse with $\sigma_{\mathrm{XUV}} = 12.7\,\mathrm{fs}$.

$$\Delta t = (10 \pm 6)\ \mathrm{fs}.$$

The error is determined from the standard deviation of all the results for Δt. In the next step, the Auger lifetime is calculated from the results. The XUV pulse is assumed to have a rms duration of $\sigma_{\mathrm{XUV}} = 12.7\,\mathrm{fs}$ (for a fundamental pulse length of 30 fs FWHM for the HHG). In this case, the dependence of the Auger lifetime on the time shift is shown in Figure 5.14. The expected Auger lifetime for a time shift of $\Delta t = (10 \pm 6)$ fs is:

$$\tau_{\mathrm{Auger}} = (14^{+27}_{-11})\ \mathrm{fs}.$$

As visible from Figure 5.14, the distribution of Auger lifetime is not symmetrical. Comparing this value with the expected literature value of around 6 fs for 4d xenon Auger electrons shows that the expected value lies within our distribution of Auger lifetimes. For lifetimes as small as a few femtoseconds like the Auger lifetime of 6 fs, the uncertainty is relatively high.

5.3.4. Iodomethane

In this section, the Auger decay in a molecular system will be investigated. The system chosen for this study is CH_3I, where the ionization of the 4d orbital in iodine is the dominant feature. In this case the Auger electrons do not emerge from a pure ionic state and therefore have different decay characteristics. In this case the Auger peaks are broadened

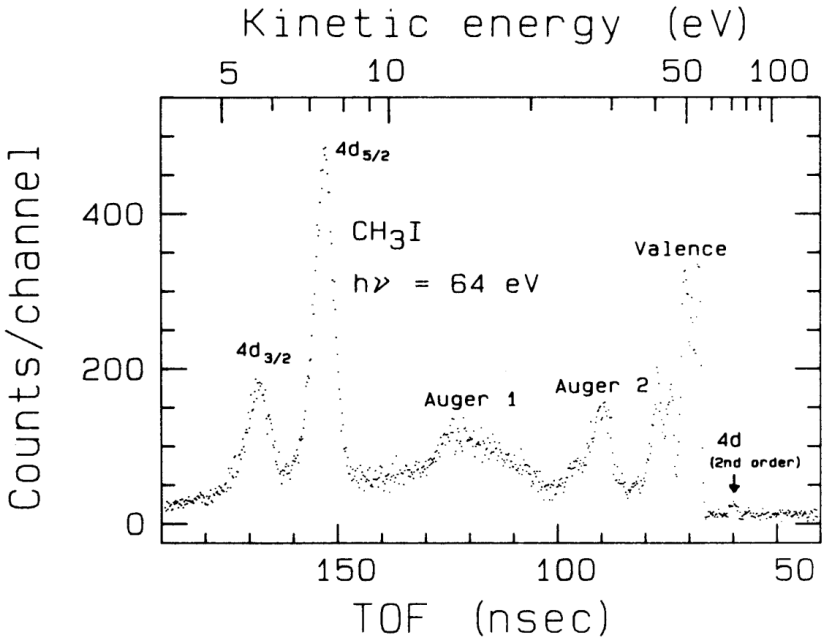

Figure 5.15.: The spectrum for a photoionization energy of 64 eV. The Auger peaks result from the decay of the 4d vacancy and are located around15 eV to 20 eV and 25 eV to 30 eV (taken from [47]).

and have many contributions. They are not single peaks with a spectral width associated with their lifetime.

A reference time-of-flight spectrum for a photoionzation measurement with photons at 64 eV is shown in Figure 5.15 [47]. The binding energies of the $4d_{5/2}$ and the $4d_{3/2}$ states are 56.6 eV and 58.4 eV [48, 49], respectively. The partial cross section for the ionization of the $4d_{5/2}$ and $4d_{3/2}$ orbitals are different (Figure 5.16). Therefore the photopeaks have different intensities. In Figure 5.17, a comparison of the simulated spectrum and the measured spectrum is shown. The photopeaks are scaled with the intensity of the high harmonic orders measured with a Zr-filter. There are contributions from the $4d_{5/2}$ and $4d_{3/2}$ orbitals for each photon energy. Due to the overlap of the different photopeaks, the peaks are not very distinct, which makes it harder to fit. The Auger peaks ($N_{4,5}VV$) result from the decay of the 4d vacancy states and have energies around 15 eV to 20 eV and 25 eV to 30 eV. As these are molecular Auger peaks, they have a broader distribution from the different rotational and vibrational states of the molecule, which contribute to the peak. Only the Auger peak around 28 eV is visible in the data, the weaker Auger signal around 15 eV can not be resolved. The measured spectrum shows data taken with a Zr filter. For CH_3I, the Auger peaks are broader compared with the pure atomic Auger peaks in xenon, see Figure 5.17, right side.

Performing a measurement with our high harmonic source and using an aluminum filter to select the 11th to 47th harmonic order, a spectrum with CH_3I was measured. Due to the lower binding energy of the 4d orbital, the Auger signal with the Al filter was stronger

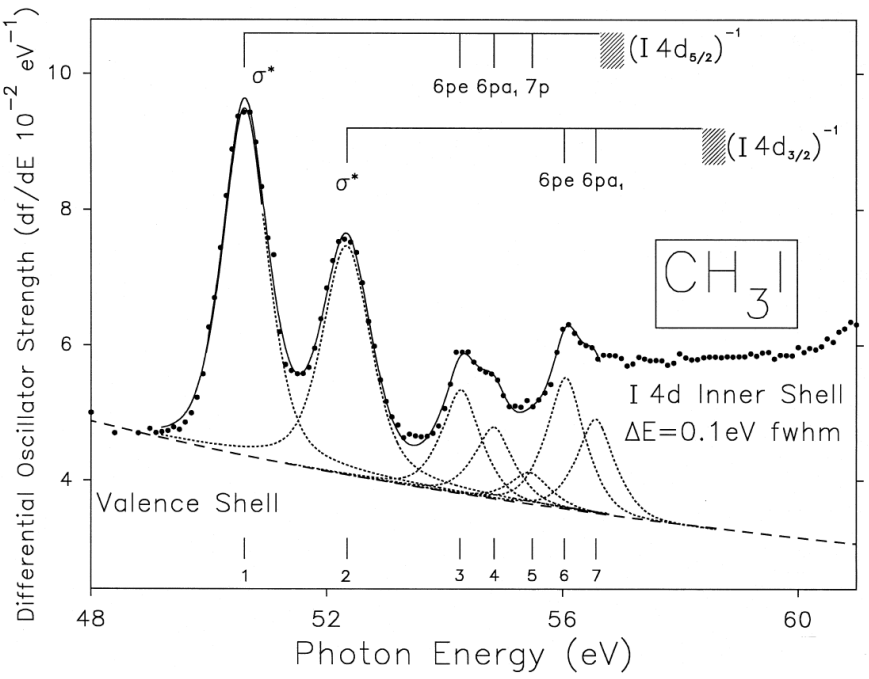

Figure 5.16.: Dipole photoabsorption oscillator strength spectrum of CH_3I in the I 4d region (taken from [49]).

for CH_3I compared to the xenon measurements. The full scan for different time delays between the XUV and THz pulses is shown in Figure 5.18. There is a broad range of electron curves, and again, the Auger electrons curves overlap with some photoelectron curves. Due to our limited choice in selecting harmonic orders by using either an Al or Zr filter, this can not be completely avoided.

In Figure 5.19, one example spectrum of a measurement with Al is shown. The data was again fitted with Gaussian peaks to get the energy of the photo- and Auger electrons. Due to the lower signal of the $4d_{3/2}$ photoelectrons, these peaks could not be fitted separately. Only the stronger $4d_{5/2}$ peaks were fitted. This changes the fitted widths of the peaks but should not influence determination of the peak positions. As already done with the xenon data, the photopeaks, which overlap with the Auger peaks, were omitted in the fit to facilitate the fitting procedure.

The results for a complete streaking scan are shown in Figure 5.20. Here one of the photopeaks and the Auger peak are fitted with a Gaussian envelope. The results for the time shift between the photocurves and Auger curve is:

$$\Delta t = (2 \pm 13)\ \text{fs}.$$

Calculating the Auger lifetime from this curve results in:

$$\tau_{\text{Auger}} = (2^{+34}_{-13})\ \text{fs}.$$

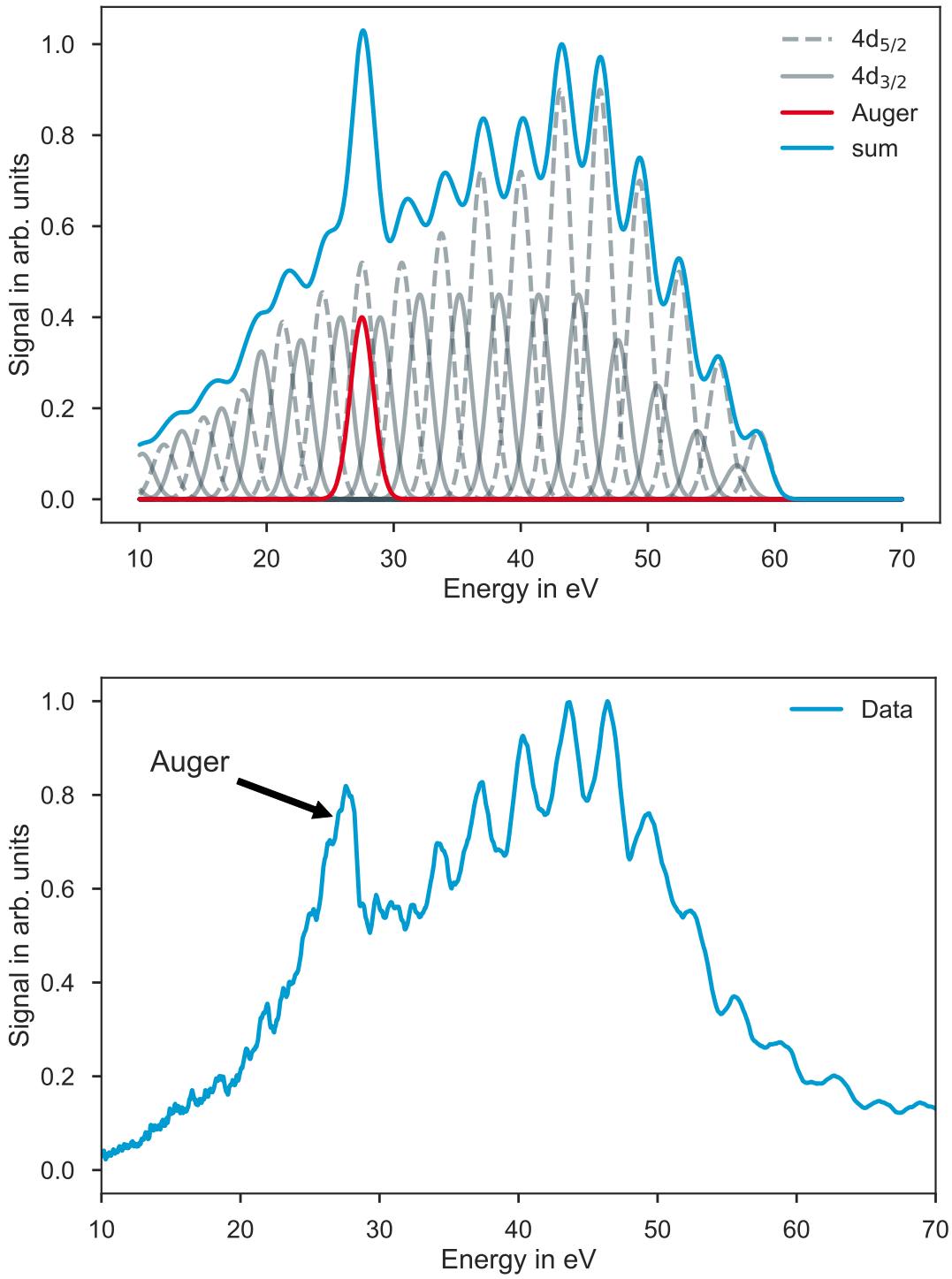

Figure 5.17.: Comparison between a simulated spectrum (top) and measured data using a Zr filter (bottom). The photopeaks result from the $4d_{5/2}$ and $4d_{3/2}$ orbitals and are not well distinguished. The $4d_{3/2}$ orbital has a lower partial cross section and the peaks can not be resolved. The Auger peaks around 28 eV overlap with some of the photopeaks.

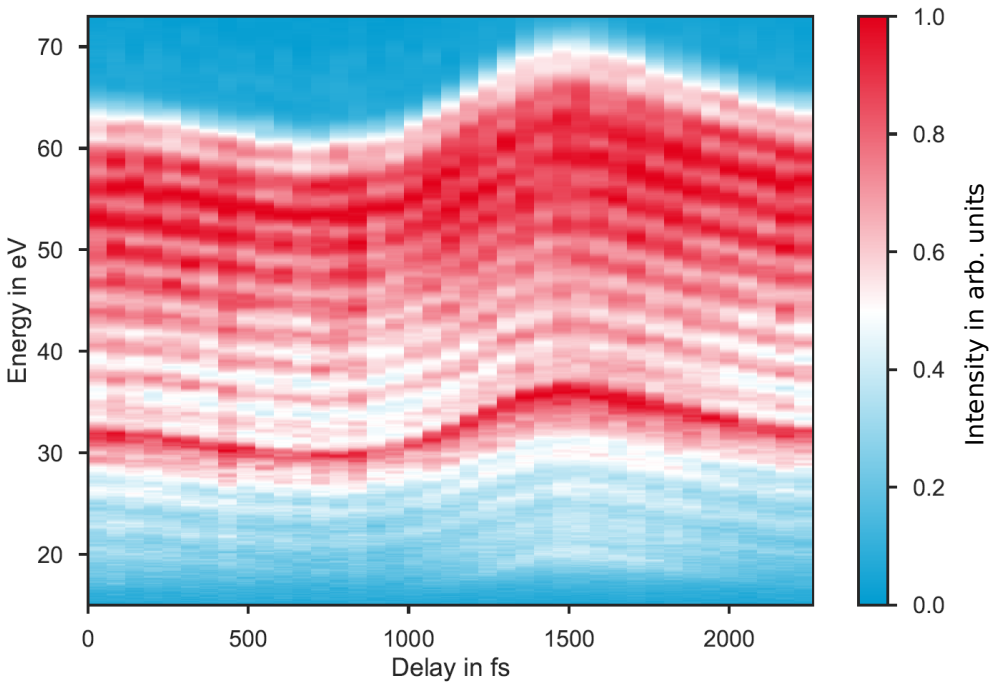

Figure 5.18.: Spectra from CH_3I measured for different delay times between the XUV and THz pulse.

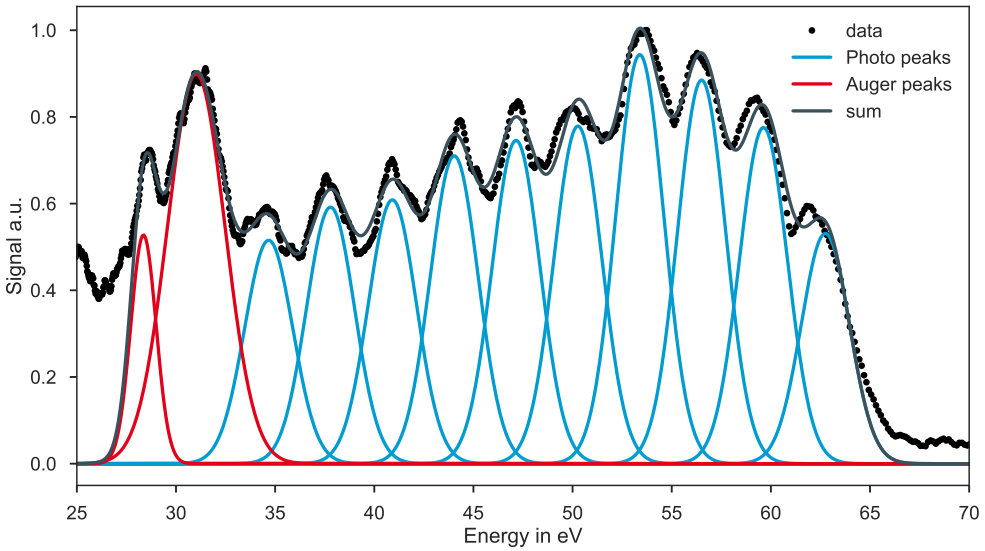

Figure 5.19.: Spectrum fitted with Gaussian peaks to obtain the position of the photo- and the Auger peaks. Only photopeaks for the $4d_{5/2}$ are fitted because the weaker $4d_{3/2}$ peaks are not resolved.

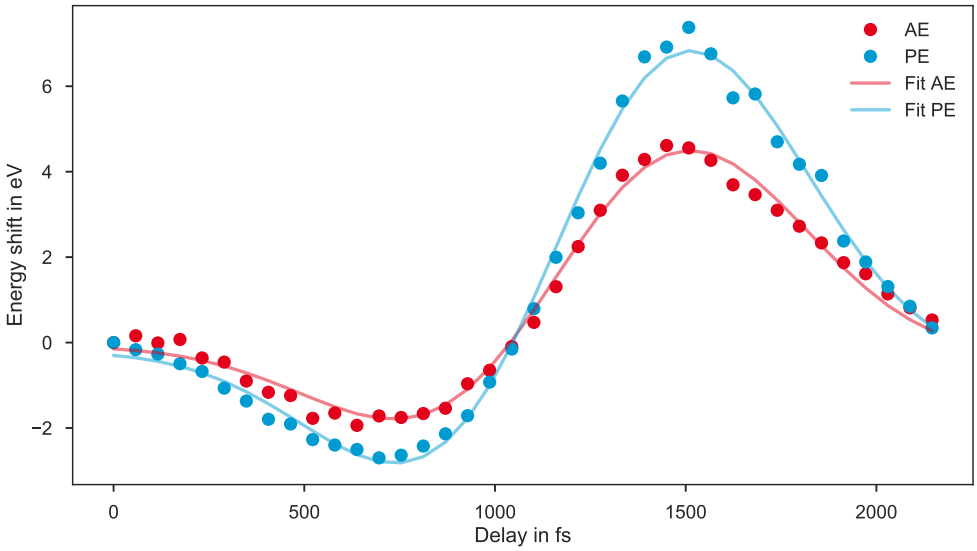

Figure 5.20.: Energy shift of a photoelectron and the Auger peak. Fitting a Gaussian envelope to the curves to determine the time shift between them.

For the Gaussian fit of the electron peaks, a few assumptions were made, like taking only the $4d_{5/2}$ peaks into account and having an Auger peak with no contribution from photoelectrons at this energy. For CH_3I, the photo and Auger curves overlap even more than in the xenon spectrum, which decreases the capability to distinguish between the photo and Auger peaks, so the last assumption of a pure Auger electron peak might not be correct.

So, instead of making the above assumptions for the Gaussian fit, a simple peak finding algorithm was used as a different method to determine the peak positions for each spectrum. Using the results from the peak finder, a Gaussian envelope was fitted to the curves of the Auger electrons and photoelectrons (Figure 5.21). With this procedure, the results for the timeshift and the Auger lifetime are:

$$\Delta t = (7 \pm 11)\ \text{fs},$$

and

$$\tau_{\text{Auger}} = (9^{+50}_{-13})\ \text{fs}.$$

The larger uncertainty for the Auger lifetime with the second method results from the fact, that the dependence of the Auger lifetime on the time shift is not linear and for larger time shifts (7 fs from the peak finder instead of 2 fs for the Gaussian fits) the uncertainty on the Auger lifetime also becomes larger.

For the Auger lifetime measurements of iodomethane, the uncertainty in the results is more significant than for the measurements with xenon. One factor might be the overlap

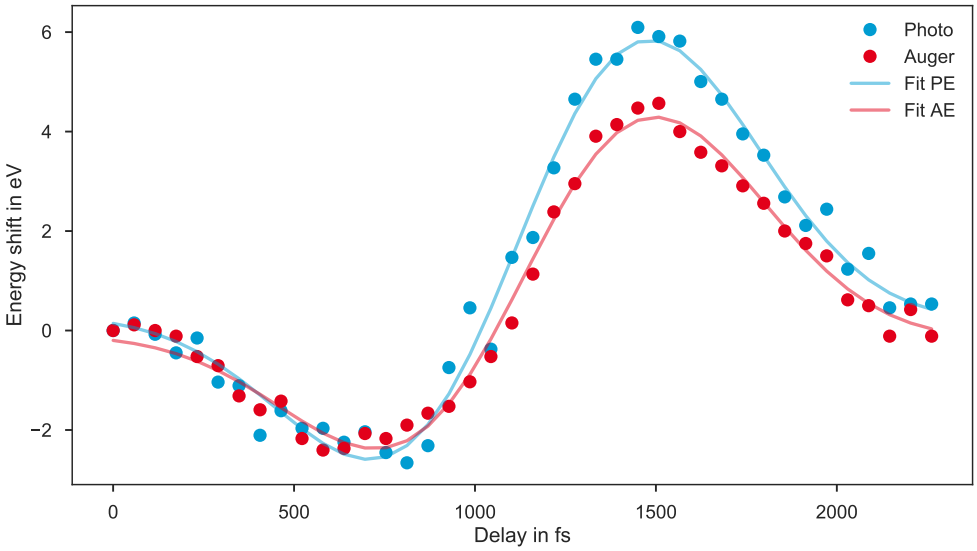

Figure 5.21.: Energy shift of a photoelectron and the Auger peak. The energy shift was determined by using a peakfinder for the single spectra and the curves were fitted using a Gaussian envelope.

between the photoelectron and the Auger electron peaks. To improve these measurements, it would be better to have the photoelectron peaks at different energies than the Auger electron peak. Unfortunately, we were limited in the choice of harmonics; it was not possible to select the harmonics without overlap with the Auger peak. Another factor might be the unresolvable photoelectron peaks of the $4d_{5/2}$ and $4d_{3/2}$ orbitals.The peaks of the photoelectrons were not as pronounced as, for example, from the measurements with neon, so this might have decreased the accuracy of the fit.

5.4. Comparison of Measurements and Simulation

To better understand why the measurements of the Auger lifetime have such large measurement uncertainties, the temporal resolution of the setup will now be investigated in more detail. For this purpose, the measurements performed with the laboratory sources will be compared with the measurements performed at FLASH. In order to compare the measurements, the behavior of the two measuring methods was simulated. The parameters of both sources were used as values for the THz frequency and the width of the Gaussian envelope. Thus, the different behavior of the measurements can be better understood.

First the behavior of the photoelectrons and Auger electrons of the laboratory source is compared, see Figure 5.22. Since the photoelectrons and Auger electrons have different starting energies, the streaking amplitude is different for the two curves. With the kinetic energy values of 35 eV for the Auger electron and 27 eVfor the photoelectrons, the amplitude factor is about $\sqrt{(E_{0,\,\mathrm{AE}}/E_{0,\,\mathrm{PE}})} \approx 1.15$. In Figure 5.22 on the left, the two curves

representing the Auger electrons and the photoelectrons have no time offset. On the right side of Figure 5.22 the case for a time offset of 10 fs is shown. The laboratory source has a frequency of about 0.5 THz, and the time shift of 10 fs corresponds to a phase change of only $\pi/100$. It is challenging to determine this small phase change with fluctuating measurement data using the fit of the Gaussian envelope.

In contrast, FLASH uses an undulator to generate the THz pulses; thus, pulses with several oscillation periods are created. The frequency can be adjusted with the undulator. In the measurements in [1], the THz frequency was about 5 THz. In the left plot of Figure 5.23, the curves for the photo- and auger electrons are shown without time shift and in the right plot again with a time offset of 10 fs. Here, the time shift corresponds to a relative phase change of $\pi/10$. The relative phase change is thus much more significant for the FLASH measurements than for the laser-based ones. This larger relative phase shift makes it possible to determine the lifetime of the krypton Auger electrons at FLASH of $\tau_{\text{Kr, measured}} = (8 \pm 5)$ fs with a literature value $\tau_{\text{Kr,AE}} = 7.9^{+1}_{-0.9}$ fs, whereby a better accuracy is achieved than with the laboratory measurements. A higher THz frequency is recommended for the streaking measurements if time shifts in the range of 10 fs should be resolved since the relative phase change is more significant.

To estimate the required resolution to measure the ICD lifetimes, some simulations were performed. For states decaying by ICD, the average lifetime strongly depends on the extent of the system, its constituents, and the number of direct neighbors available to the excited atom or molecule. The lifetimes of ICD are typically slower than local Auger decay, but faster than a fluorescence decay in the same system. In experiments performed by K. Schnorr et al. [14] investigating the ICD lifetime of the Ne_2^+ ($2s^{-1}$) state, a lifetime of (150 ± 50) fs was found. Furthermore, an ICD lifetime of 85 fs was obtained for modeling neon dimers. Therefore the expected lifetime for the ICD is much longer than the Auger decay of the xenon NOO-Augers, which were investigated in the previous section.

For the simulations, an Auger electron trace was selected. For this curve, the measurement points were shifted by the amount expected if the measured timeshift Δt was 5 fs, 10 fs, 50 fs, 85 fs to the measured trace. For a timeshift of $\Delta t = 10$ fs, 50 fs, 85 fs the results are shown in Figure 5.24. The results were fitted with a Gaussian envelope. The timeshifts could be reproduced for all the curves. The fit error for the timeshift was the same for all traces (standard error 16 fs). The fit error seems to be influenced by the initial noise of the data. The initial data from fitting Gaussian peaks to the measured spectra has to improve to change the temporal resolution. One possibility is to have spectra without overlapping Auger and photopeaks where the peak fitting procedure can produce better results. Also, measuring shorter lifetimes with a higher THz frequency might be beneficial.

With the results shown in Figure 5.24, it is clear that the experimental setup might have some difficulties to resolve short Auger lifetimes below 10 fs with enough accuracy, but is well suited for measuring longer ICD lifetimes.

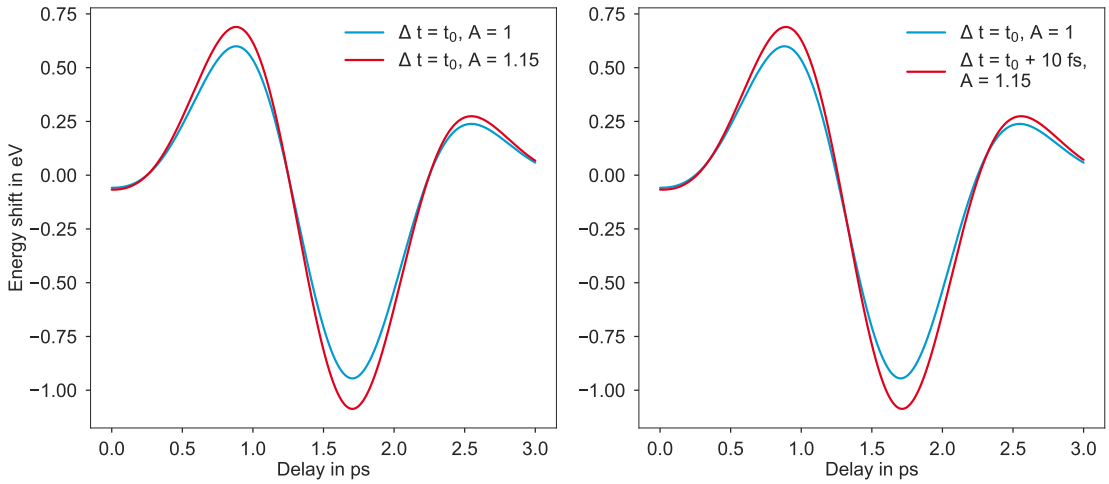

Figure 5.22.: Simulated streaking curves with similar parameters as measured. Left: No time shift between the curves. The red curve has a larger streaking amplitude (A=1.15) due to different initial energies. Right: Time shift of 10 fs between the curves. Again, the red curve has a larger streaking amplitude (A=1.15). The time shift corresponds to a relative phase shift of only $\pi/100$.

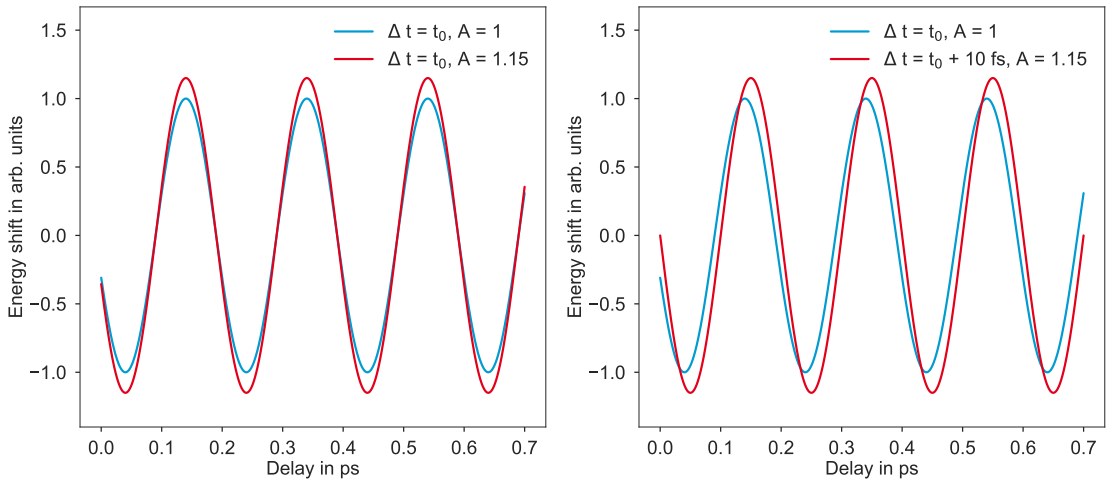

Figure 5.23.: Simulated streaking curves with THz pulse parameters according to the FLASH measurements [1]. Left: No time shift between the red and blue curve. Right: A time shift of 10 fs between the red and blue curve, which corresponds to a relative phase shift of $\pi/10$.

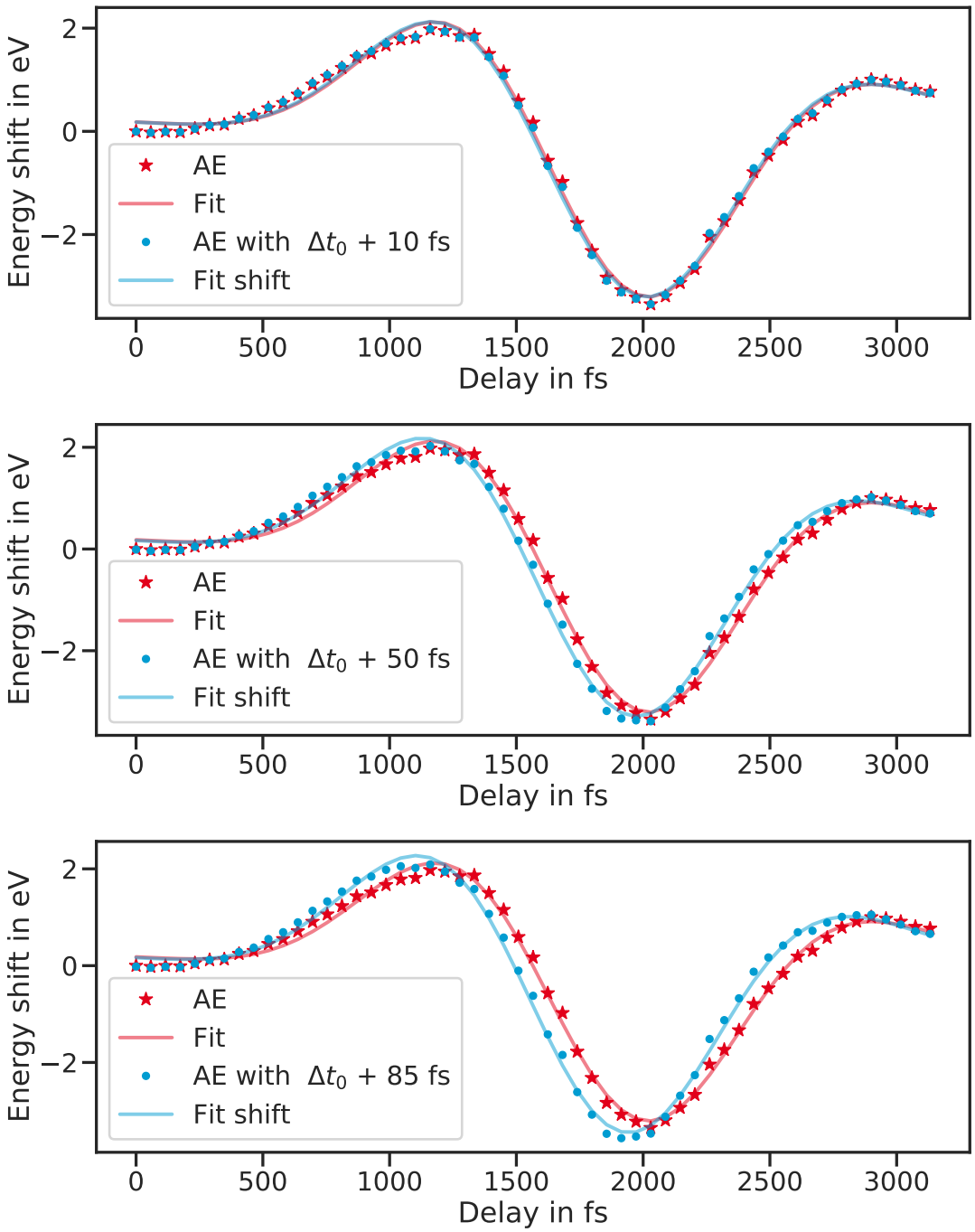

Figure 5.24.: Simulated data points for timeshifts $\Delta t_0 = 10\,\text{fs}$, 50 fs, and 85 fs.

6. Discussion

Within the scope of this thesis, an experimental setup for the measurement of time-resolved dynamics of Auger decays and interatomic Coulombic decays has been implemented. A THz streak camera, an ultrashort pulse laser-based XUV and a THz source were set up. To prove the functionality of the setup, the Auger lifetime of a known system, the $N_{4,5}OO$ Auger electrons of xenon, was measured. From these measurements, simulations of the setup could show that the temporal resolution is sufficient for the planned coincidence measurements of ICD electrons.

For this thesis, a HHG source was implemented and characterized. The XUV pulses are generated from focusing the IR pulses in a gas nozzle with neon as the target gas. A broad spectrum of the high harmonics can be selected for the experiments leading to a high number of photons in the interaction zone. Measurements with a calibrated XUV photodiode showed more than 6000 photons for each harmonic order in the interaction zone.

The single-cycle THz pulses were produced using a tilted-pulse-front setup. The fundamental 800 nm femtosecond pulses are imaged by a grating and a single achromatic lens into the $LiNbO_3$ crystal, and due to optical rectification, THz pulses are generated. The temporal profile of the THz pulses was characterized using electro-optical sampling. Electric-field amplitudes of around 2 MV/m were achieved.

Measurements of the XUV pulse length from the electron spectra measured with the TOFs and the THz field revealed longer pulse lengths than expected. This is attributed to the measurement method, which has problems of correctly measuring the XUV pulse length for low THz streaking speeds, as the measured change in the electron peak widths is relatively small. This is a known problem, which also appeared in [37, 42] With the limited temporal resolution of the TOFs, the XUV pulse length could not be clearly determined from the streaking measurements.

The goal of the characterization measurements of known Auger decays was to show that the temporal resolution to measure Auger and ICD lifetimes can be achieved. The reference measurements of the $N_{4,5}OO$ Auger electrons of xenon resulted in a measured lifetime of $\tau_{Auger} = 14^{+27}_{-11}$ fs. This result deviates from the reference value of $\tau_{\mathrm{Auger}} = 6$ fs and has a rather high uncertainty. Other measurements of the Auger lifetimes of iodomethane did not provide unambiguous results for the molecular Auger lifetimes. Comparing the results achieved with our method to the measurements of the experiments performed at FLASH [1], a lower time resolution was found. One of the advantages of using THz radiation from a free-electron laser was the higher THz frequency and

the multicycle nature of the pulses. A shift of a few femtoseconds leads to a more significant shift between the streaking curves of the Auger and photoelectrons for higher THz frequencies. Simulations of streaking spectra with different lifetimes for the decays show that the uncertainty is mostly influenced by the fluctuations of the measured energy shift. Problems like overlapping photoelectron and Auger electron peaks limited deteriorated the achievable accuracy. For typical lifetimes of the longer-lived ICD electrons, this limited resolution is not a problem. Therefore this method can be applied for the coincidence measurements with the COLTRIMS detector.

Some challenges remain for the coincidence measurements. The low repetition rate of 1 kHz would require longer measurement times, but due to the coincidence measurements, all the noisy data will be filtered out, which improves the quality of the measured spectra. Another factor to keep in mind is the weaker THz field strength in the interaction zone due to the longer focal length required due to the geometrical limitations of the setup. The THz source might need improvements like better optical components to reduce the detrimental effects on them and to achieve higher electric field strengths.

In conclusion, the measurements of the Auger decay lifetimes and the simulations with different values for the decay lifetimes showed that the setup is suitable for the planned coincidence measurements and that time-resolved measurements from a combination of the COLTRIMS measurement technique with THz streaking should be well suited to study the lifetime of ICD electrons in neon dimers.

A. Acknowledgments

There was a point to this story, but it has temporarily escaped the chronicler's mind.

Douglas Adams, So Long, and Thanks for All the Fish

An dieser Stelle möchte ich allen danken, die mich bei der Entstehung dieser Arbeit unterstützt haben. Zuerst möchte ich mich bei Prof. Dr. Ulrike Frühling für die Möglichkeit bedanken, diese Arbeit in Ihrer Arbeitsgruppe anzufertigen. Ich habe in der Zeit in Ihrer Gruppe sehr viel gelernt und auch bei Problemen konnte ich mich auf Ihre Unterstützung und gute persönliche Betreuung verlassen. Bei PD Dr. Michael Martins möchte ich mich für die Übernahme des Zweitgutachtens bedanken.

Außerdem möchte ich meinen aktuellen und ehemaligen Kollegen der ufast Gruppe danken. Mark Prandolini für das Korrekturlesen meiner Arbeit und das Diskutieren und Erklären vieler theoretischer Konzepte. Tasos Dimitriou für die Planung des THz-Setups, Martin Ranke für den gemeinsamen Aufbau der Harmonischen Quelle und die gemeinsame Arbeit im Labor und Markus Pfau für seine nette Unterstützung in Labor und die moralische Aufheiterung, wenn es nicht lief wie geplant.

Bei Dr. Marek Wieland für seine Ratschläge und das freundliche Ausleihen von Messequipment. Ohne diese Unterstützung würde doch einiges an meinem Experiment fehlen. Bei Oliver Becker möchte ich mich für die Unterstützung bei technischen Problemen bedanken und Yannic Ristau für die gute Zusammenarbeiten beim Fixen von Laser(chiller)problemen und beim Teilen der Laserzeit. Des Weiteren möchte ich der mechanischen Werkstatt unter Leitung von Stephan Fleig danken, für den Support und die Herstellung zahlreicher Bauteile.

Zudem möchte ich meiner Familie und meinen Freunden für die Unterstützung und Motivation danken. Meinem Schwager Marco und meinem Freund Nils für das Korrekturlesen und zudem Nils dafür, dass er immer für mich da war, auch wenn uns meist mehrere hundert bis tausend Kilometer trennten.

Eidesstattliche Versicherung

Hiermit versichere ich an Eides statt, die vorliegende Dissertationsschrift selbst verfasst und keine anderen als die angegebenen Hilfsmittel und Quellen benutzt zu haben.

Die eingereichte schriftliche Fassung entspricht der auf dem elektronischen Speichermedium.

Die Dissertation wurde in der vorgelegten oder einer ähnlichen Form nicht schon einmal in einem früheren Promotionsverfahren angenommen oder als ungenügend beurteilt.

Hamburg, den _____ Unterschrift: _____

Bibliography

[1] K. Wenig, M. Wieland, A. Baumann, S. Walther, *et al.*, "Electronic decay of core-excited HCl molecules probed by THz streaking," *Structural Dynamics* **6** 034301, 05, 2019.

[2] T. H. Strickland, "Stimulated optical radiation in ruby," *Nature* **187** 493 – 494, 1960.

[3] D. Strickland and G. Mourou, "Compression of amplified chirped optical pulses," *Optics Communications* **56** no. 3, 219 – 221, 1985. http://www.sciencedirect.com/science/article/pii/0030401885901208.

[4] U. Keller, G. W. 'tHooft, W. H. Knox, and J. E. Cunningham, "Femtosecond pulses from a continuously self-starting passively mode-locked ti:sapphire laser," *Opt. Lett.* **16** no. 13, 1022–1024, Jul, 1991. http://ol.osa.org/abstract.cfm?URI=ol-16-13-1022.

[5] A. McPherson, G. Gibson, H. Jara, U. Johann, *et al.*, "Studies of multiphoton production of vacuum-ultraviolet radiation in the rare gases," *J. Opt. Soc. Am. B* **4** no. 4, 595–601, Apr, 1987. http://josab.osa.org/abstract.cfm?URI=josab-4-4-595.

[6] P. Eckle, A. N. Pfeiffer, C. Cirelli, A. Staudte, *et al.*, "Attosecond ionization and tunneling delay time measurements in helium," *Science* **322** no. 5907, 1525–1529, 2008. https://science.sciencemag.org/content/322/5907/1525.full.pdf.

[7] L. Meitner, "Über die Entstehung der β-Strahl-Spektren radioaktiver Substanzen," *Zeitschrift für Physik* **9** 131–144, 1922.

[8] P. Auger, "Sur l'effet photoélectrique composé," *J. Phys. Radium* **6** 205–208, 1925.

[9] L. S. Cederbaum, J. Zobeley, and F. Tarantelli, "Giant intermolecular decay and fragmentation of clusters," *Phys. Rev. Lett.* **79** 4778–4781, Dec, 1997. https://link.aps.org/doi/10.1103/PhysRevLett.79.4778.

[10] S. Marburger, O. Kugeler, U. Hergenhahn, and T. Möller, "Experimental evidence for interatomic coulombic decay in Ne clusters," *Phys. Rev. Lett.* **90** 203401, May, 2003. https://link.aps.org/doi/10.1103/PhysRevLett.90.203401.

[11] T. Jahnke, A. Czasch, M. S. Schöffler, S. Schössler, *et al.*, "Experimental observation of interatomic coulombic decay in neon dimers," *Phys. Rev. Lett.* **93** 163401, Oct, 2004. https://link.aps.org/doi/10.1103/PhysRevLett.93.163401.

[12] T. Jahnke, A. Czasch, M. Schöffler, S. Schössler, *et al.*, "Photoelectron and ICD electron angular distributions from fixed-in-space neon dimers," *Journal of Physics B: Atomic, Molecular and Optical Physics* **40** no. 13, 2597–2606, Jun, 2007. https://doi.org/10.1088%2F0953-4075%2F40%2F13%2F006.

[13] S. Scheit, L. S. Cederbaum, and H.-D. Meyer, "Time-dependent interplay between electron emission and fragmentation in the interatomic coulombic decay," *The Journal of Chemical Physics* **118** no. 5, 2092–2107, 2003. https://doi.org/10.1063/1.1531996.

[14] K. Schnorr, A. Senftleben, M. Kurka, A. Rudenko, *et al.*, "Time-resolved measurement of interatomic coulombic decay in ne-2," *Physical review letters* **111** 093402, 08, 2013.

[15] F. Trinter, J. B. Williams, M. Weller, M. Waitz, *et al.*, "Evolution of interatomic coulombic decay in the time domain," *Phys. Rev. Lett.* **111** 093401, Aug, 2013. https://link.aps.org/doi/10.1103/PhysRevLett.111.093401.

[16] P. B. Corkum, "Plasma perspective on strong field multiphoton ionization," *Phys. Rev. Lett.* **71** 1994–1997, Sep, 1993. https://link.aps.org/doi/10.1103/PhysRevLett.71.1994.

[17] L. V. Keldysh, "Ionization in the field of a strong electromagnetic wave," *Soviet Phys. JETP* **20** 1307–1314, May, 1965. http://www.jetp.ac.ru/cgi-bin/e/index/e/20/5/p1307?a=list.

[18] M. V. Ammosov, P. A. Golovinsky, I. Y. Kiyan, V. P. Krainov, and V. M. Ristic, "Tunneling ionization of atoms and atomic ions in an intense laser field with a nonhomogeneous space–time distribution," *J. Opt. Soc. Am. B* **9** no. 8, 1225–1230, Aug, 1992. http://josab.osa.org/abstract.cfm?URI=josab-9-8-1225.

[19] J. Rothhardt, M. Krebs, S. Hädrich, S. Demmler, *et al.*, "Absorption-limited high harmonic generation in the tight focusing regime," in *Research in Optical Sciences*, p. HW3C.3. Optical Society of America, 2014. http://www.osapublishing.org/abstract.cfm?URI=HILAS-2014-HW3C.3.

[20] T. Popmintchev, M.-C. Chen, A. Bahabad, M. Gerrity, *et al.*, "Phase matching of high harmonic generation in the soft and hard x-ray regions of the spectrum," *Proceedings of the National Academy of Sciences* **106** no. 26, 10516–10521, 2009. https://www.pnas.org/content/106/26/10516.full.pdf.

[21] M. Ranke, *Investigation of low-energy photoelectron dynamics accelerated in terahertz light fields using a novel Velocity-Map-Imaging spectrometer*. PhD thesis, Universität Hamburg, 2019.

[22] A. Leitenstorfer, K. A. Nelson, K. Reimann, and K. Tanaka, "Focus on nonlinear terahertz studies," *New Journal of Physics* **16** no. 4, 045016, Apr, 2014. https://doi.org/10.1088%2F1367-2630%2F16%2F4%2F045016.

[23] K. Kawase, Y. Ogawa, H. Minamide, and H. Ito, "Terahertz parametric sources and imaging applications," *Semiconductor Science and Technology* **20** no. 7, S258–S265, Jun, 2005. https://doi.org/10.1088%2F0268-1242%2F20%2F7%2F017.

[24] J. Hebling, K.-L. Yeh, M. C. Hoffmann, B. Bartal, and K. A. Nelson, "Generation of high-power terahertz pulses by tilted-pulse-front excitation and their application possibilities," *J. Opt. Soc. Am. B* **25** no. 7, B6–B19, Jul, 2008. http://josab.osa.org/abstract.cfm?URI=josab-25-7-B6.

[25] J. A. Fülöp, L. Pálfalvi, G. Almási, and J. Hebling, "Design of high-energy terahertz sources based on optical rectification," *Opt. Express* **18** no. 12, 12311–12327, Jun, 2010. http://www.opticsexpress.org/abstract.cfm?URI=oe-18-12-12311.

[26] X. Wu, C. Zhou, W. R. Huang, F. Ahr, and F. X. Kärtner, "Temperature dependent refractive index and absorption coefficient of congruent lithium niobate crystals in the terahertz range," *Opt. Express* **23** no. 23, 29729–29737, Nov, 2015. http://www.opticsexpress.org/abstract.cfm?URI=oe-23-23-29729.

[27] K. Ravi, W. R. Huang, S. Carbajo, E. A. Nanni, *et al.*, "Theory of terahertz generation by optical rectification using tilted-pulse-fronts," *Opt. Express* **23** no. 4, 5253–5276, Feb, 2015. http://www.opticsexpress.org/abstract.cfm?URI=oe-23-4-5253.

[28] G. Cirmi, M. Hemmer, K. Ravi, F. Reichert, *et al.*, "Cascaded second-order processes for the efficient generation of narrowband terahertz radiation," *Journal of Physics B: Atomic, Molecular and Optical Physics* **50** no. 4, 044002, Jan, 2017. https://doi.org/10.1088%2F1361-6455%2Faa5405.

[29] K. Ravi, W. R. Huang, S. Carbajo, X. Wu, and F. Kärtner, "Limitations to THz generation by optical rectification using tilted pulse fronts," *Opt. Express* **22** no. 17, 20239–20251, Aug, 2014. http://www.opticsexpress.org/abstract.cfm?URI=oe-22-17-20239.

[30] Q. Meng, B. Zhang, S. Zhong, and L. Zhu, "Damage threshold of lithium niobate crystal under single and multiple femtosecond laser pulses: theoretical and experimental study," *Applied Physics A* **122** no. 6, 582, May, 2016. https://doi.org/10.1007/s00339-016-0120-x.

[31] J. Hebling, "Derivation of the pulse front tilt caused by angular dispersion," *Optical and Quantum Electronics* **28** no. 12, 1759–1763, Dec, 1996. https://doi.org/10.1007/BF00698541.

[32] B. Pradarutti, G. Matthäus, S. Riehemann, G. Notni, *et al.*, "Highly efficient terahertz electro-optic sampling by material optimization at 1060nm," *Optics Communications* **281** no. 19, 5031 – 5035, 2008. http://www.sciencedirect.com/science/article/pii/S0030401808006196.

[33] U. Frühling, *Lichtfeld getriebene Streak-Kamera zur Einzelschuss Zeitstrukturmessung der XUV-Pulse eines Freie-Elektronen Lasers*. PhD thesis, Universität Hamburg, 2009.

[34] U. Frühling, "Light-field streaking for FELs," *Journal of Physics B: Atomic, Molecular and Optical Physics* **44** no. 24, 243001, Nov, 2011. https://doi.org/10.1088%2F0953-4075%2F44%2F24%2F243001.

[35] F. Quéré, Y. Mairesse, and J. Itatani, "Temporal characterization of attosecond xuv fields," *Journal of Modern Optics* **52** no. 2-3, 339–360, 2005. https://doi.org/10.1080/09500340412331307942.

[36] N. Friesen, *Evaluation molekularer Targets für eine zeitauflösende Elektronenspektroskopie*. PhD thesis, Universität Hamburg, 2019.

[37] R. Brannath, *Zeitliche Verteilung von Auger-Elektronen-Wellenpaketen aus der Photoionisation von Atomen*. PhD thesis, Universität Hamburg, 2016.

[38] R. W. Boyd, "Intuitive explanation of the phase anomaly of focused light beams," *J. Opt. Soc. Am.* **70** no. 7, 877–880, Jul, 1980. http://www.osapublishing.org/abstract.cfm?URI=josa-70-7-877.

[39] S. Feng and H. Winful, "Physical origin of the gouy phase shift," *Optics letters* **26** 485–7, 05, 2001.

[40] B. Schütte, *Laser-based terahertz-field-driven streak camera for the temporal characterization of ultrashort processes*. PhD thesis, Universität Hamburg, 2011.

[41] U. Becker and D. Shirley, *VUV and soft X-ray photoionization*. Springer, 1996.

[42] M. Pfau, *Messaufbau für zeitauflösende Atom- und Molekülspektroskopie im extrem ultravioletten Spektralbereich*. PhD thesis, Universität Hamburg, 2019.

[43] M. Schultze, M. Fieß, N. Karpowicz, J. Gagnon, *et al.*, "Delay in photoemission," *Science* **328** no. 5986, 1658–1662, 2010. https://science.sciencemag.org/content/328/5986/1658.full.pdf.

[44] F. Penent, J. Palaudoux, P. Lablanquie, L. Andric, *et al.*, "Multielectron spectroscopy: the xenon 4d hole double auger decay," *Physical review letters* **95** no. 8, 083002, August, 2005. https://doi.org/10.1103/PhysRevLett.95.083002.

[45] M. Jurvansuu, A. Kivimäki, and S. Aksela, "Inherent lifetime widths of Ar $2p^{-1}$, Kr $3d^{-1}$, Xe $3d^{-1}$, and Xe $4d^{-1}$ states," *Phys. Rev. A* **64** 012502, Jun, 2001. https://link.aps.org/doi/10.1103/PhysRevA.64.012502.

[46] L. Werme, T. Bergmark, and K. Siegbahn, "The high resolution L2,3 MM and M4,5 NN auger spectra from krypton and M4,5 NN and N4,5 OO auger spectra from xenon," *Physica Scripta* **6** 141, 01, 2007.

[47] D. W. Lindle, P. H. Kobrin, C. M. Truesdale, T. A. Ferrett, *et al.*, "Inner-shell photoemission from the iodine atom in CH_3I," *Phys. Rev. A* **30** 239–244, Jul, 1984. https://link.aps.org/doi/10.1103/PhysRevA.30.239.

[48] J. N. Cutler, G. M. Bancroft, and K. H. Tan, "Ligand-field splittings and core-level linewidths in I 4d photoelectron spectra of iodine molecules," *The Journal of Chemical Physics* **97** no. 11, 7932–7943, 1992. https://doi.org/10.1063/1.463468.

[49] T. N. Olney, G. Cooper, and C. Brion, "Quantitative studies of the photoabsorption (4.5–488 eV) and photoionization (9–59.5 eV) of methyl iodide using dipole electron impact techniques," *Chemical Physics* **232** no. 1, 211 – 237, 1998. http://www.sciencedirect.com/science/article/pii/S0301010497003686.